

The Pennsylvania State University

The Graduate School

Department of Chemistry

**INVESTIGATING LIPID HETEROGENEITY IN SINGLE CELLS USING TIME-OF-
FLIGHT SECONDARY ION MASS SPECTROMETRY**

A Dissertation in

Chemistry

by

Paul D. Piehowski

© 2009 Paul D. Piehowski

Submitted in Partial Fulfillment
of the Requirements
for the Degree of

Doctor of Philosophy

December 2009

The dissertation of Paul D. Pichowski was reviewed and approved* by the following:

Andrew G. Ewing
Professor of Chemistry
J. Lloyd Huck Chair in Natural Sciences
Dissertation Advisor
Chair of Committee

Nicholas Winograd
Evan Pugh Professor of Chemistry

Christine D. Keating
Associate Professor of Chemistry

Carlo G. Pantano
Distinguished Professor of Materials Science and Engineering
Director of the Materials Research Institute

Michael L. Heien
Research Assistant
Special Member

Barbara J. Garrison
Shapiro Professor of Chemistry
Head of the Chemistry Department

*Signatures are on file in the Graduate School

ABSTRACT

Imaging time-of-flight secondary ion mass spectrometry (ToF-SIMS) can be utilized to map the spatial distribution of small molecules on a surface with potentially submicron resolution. Due to the inherent characteristics of this technique and its potential to provide higher spatial resolution than light microscopy based techniques without the use of chemical labels, it has been utilized to study the distribution of phospholipid species in the cell membrane. It is now known that many cell membranes contain transient compositional heterogeneities, colloquially referred to as domains, which participate in vital physiological processes such as exocytosis and signal transduction. Because of their size and lifetime, much remains unknown about the nature of these heterogeneities. ToF-SIMS imaging combined with cryogenic sample preparation techniques is a promising analytical platform poised to contribute greatly to this growing field of study.

Sample preparation is crucial to obtaining quality lipid distribution maps, especially when dealing with single biological cells. To achieve this end the Winograd and Ewing groups have developed a freeze-fracture methodology adapted from cryo-SEM studies. Freeze-etching, the practice of removing excess surface water from a sample through sublimation into the vacuum of the analysis environment, has also been extensively used in conjunction with electron microscopy. This technique has been applied to ToF-SIMS imaging of cryogenically preserved single cells. By removing the excess water which condenses onto the sample *in vacuo*, a uniform surface is produced

that is ideal for imaging by static SIMS. I demonstrate that the conditions employed to remove deposited water do not adversely affect cell morphology and do not redistribute molecules in the topmost surface layers. In addition, I found that water can be controllably re-deposited onto the sample at temperatures below $-100\text{ }^{\circ}\text{C}$ in vacuum. The re-deposited water increases the ionization of characteristic fragments of biologically interesting molecules 2-fold without loss of spatial resolution. The utilization of freeze-etch methodology will increase the reliability of cryogenic sample preparations for SIMS analysis by providing greater control of the surface environment. Using these procedures, high quality spectra with both atomic bombardment as well as C_{60}^{+} cluster ion bombardment, have been obtained.

To date, many cell imaging studies have concentrated on phosphatidylcholine distributions, owing to its abundance and high ionization efficiency. However, cholesterol is a particularly interesting molecule due to its involvement in numerous biological processes. For many studies, the effectiveness of chemical mapping is limited by low signal intensity from various bio-molecules. Due to the high energy nature of the SIMS ionization process, many molecules are identified by detection of characteristic fragments. Commonly, fragments of a molecule are identified using standard samples, and those fragments are used to map the location of the molecule. MS/MS data obtained from a prototype C_{60}^{+} / quadrupole time-of-flight mass spectrometer was used in conjunction with indium LMIG imaging to map previously unrecognized cholesterol fragments in single cells. A model system of J774 macrophages doped with cholesterol was used to show that these fragments are derived from cholesterol in cell imaging experiments. Examination of relative quantification experiments reveals that m/z 147 is

the most specific diagnostic fragment and offers a 3-fold signal enhancement. These findings greatly increase the prospects for cholesterol mapping experiments in biological samples, particularly with single cell experiments. In addition, these findings demonstrate the wealth of information that is hidden in the traditional ToF-SIMS spectrum.

In order for this technique to provide insight into biological processes, it is critical to characterize the figures of merit. Because a SIMS instrument counts individual events, the precision of the measurement is controlled by counting statistics. As the analysis area decreases, the number of molecules available for analysis diminishes. This becomes critical when imaging sub-cellular features; it limits the information obtainable, resulting in images with only a few counts of interest per pixel. Many features observed in low intensity images are artifacts of counting statistics, making validation of these features crucial to arriving at accurate conclusions. With ToF-SIMS imaging, the experimentally attainable spatial resolution is a function of the molecule of interest, sample matrix, concentration, primary ion, instrument transmission, and spot size of the primary ion beam. A model, based on Poisson statistics, has been developed to validate SIMS imaging data when signal is limited. This model can be used to estimate the effective spatial resolution and limits of detection prior to analysis, making it a powerful tool for tailoring future investigations. In addition, the model allows for pixel-to-pixel intensity comparisons and can be used to validate the significance of observed image features. The implications and capabilities of the model are demonstrated here by imaging the cell membrane of resting RBL-2H3 mast cells.

Mass spectrometry imaging has been used to demonstrate that changes in membrane structure drive lipid domain formation in mating single-cell organisms. Chemical studies of lipid bilayers in both living and model systems have revealed that chemical composition is coupled to localized membrane structure. However, it is not clear if the lipids that compose the membrane actively modify membrane structure or if structural changes cause heterogeneity in the surface chemistry of the lipid bilayer. ToF-SIMS images of mating *Tetrahymena thermophila*, acquired at various stages during mating, can be used to demonstrate that lipid domain formation follows rather than precedes structural changes in the membrane. Domains are formed in response to structural changes that occur during cell-to-cell conjugation. This observation has wide implications in all membrane processes.

There is considerable interest in the unique properties of cluster ion projectiles and investigations of how they may be utilized to improve biological imaging. A C_{60}^+ cluster ion projectile was employed for sputter cleaning biological surfaces to reveal spatio-chemical information obscured by contamination overlayers. This protocol is used as a supplemental sample preparation method for time of flight secondary ion mass spectrometry (ToF-SIMS) imaging of frozen and freeze dried biological materials. Following the removal of nanometers of material from the surface using sputter cleaning; a frozen-patterned cholesterol film and a freeze-dried tissue sample were analyzed using ToF-SIMS imaging. In both experiments, the chemical information was maintained after the sputter dose, due to the minimal chemical damage caused by C_{60}^+ bombardment. The damage to the surface produced by freeze-drying the tissue sample was found to have a greater effect on the loss of cholesterol signal than the sputter-induced damage. In

addition to maintaining the chemical information, sputtering is not found to alter the spatial distribution of molecules on the surface. This approach removes artifacts that may obscure the surface chemistry of the sample and are common to many biological sample preparation schemes for ToF-SIMS imaging. In general, our results show that by removing these artifacts, the number of analyzable samples for SIMS imaging is greatly expanded.

Although imaging with sub-cellular spatial resolution has been demonstrated, it is clear that the success of future experiments is limited by the ionization efficiency of the lipids, as well as limitations imposed by a coaxial ToF geometry. Considerable work has been done in the lab, to address these limitations. This effort has resulted in the development of a hybrid quadrupole orthogonal ToF instrument equipped with a C_{60}^+ primary ion source. The capabilities and potential of this new platform will greatly increase the contributions of SIMS to the biological sciences.

TABLE OF CONTENTS

LIST OF FIGURES	xii
LIST OF TABLES	xviii
PREFACE	xix
ACKNOWLEDGEMENTS	xxi
Chapter 1 Investigating Lipid Heterogeneity in Single Cells with Time-of-Flight Secondary Ion Mass Spectrometry	1
1.1 Introduction	1
1.2 Time-of-flight secondary ion mass spectrometry	1
1.2.1 Hybrid quadrupole time-of-flight mass spectrometer	7
1.3 Building blocks of the cell membrane	7
1.3.1 Lipids	7
1.3.2 Phospholipids	9
1.3.3 Sterols	11
1.3.4 The hydrophobic effect	13
1.3.5 The bilayer membrane	14
1.3.6 Lipids and cellular communication	14
1.4 Sample Preparation	17
1.4.1 Freeze-drying	20
1.4.2 Trehalose vitrification	24
1.4.3 Freeze-etching	29
1.4.4 C ₆₀ -etching	29
1.4.5 Freeze-fracture of frozen-hydrated cells	30
1.4.6 Summary	34
1.5 References	35
Chapter 2 Freeze-Etching and Vapor Matrix Deposition for ToF-SIMS Imaging of Single Cells	37
2.1 Introduction	37
2.2 Experimental Section	39
2.2.1 Cell culture	39
2.2.2 Cell preparation for imaging	40
2.2.3 Preparation of patterned cholesterol films	41
2.2.4 Preparation of lipid films	41
2.2.5 Mass spectrometry	41
1.3 Results and Discussion	43

2.3.1 Single cell imaging	43
2.3.2 Deposition of water	45
2.3.3 Signal enhancement.....	47
2.3.4 Role of water deposition in signal enhancement.....	51
2.3.5 Surface stability during analysis.....	51
2.3.6 Imaging with cluster projectiles	54
2.4 Conclusion	54
2.5 References.....	56
Chapter 3 MS/MS Methodology to Improve Sub-Cellular Mapping of Cholesterol Using ToF-SIMS	59
3.1 Introduction.....	59
3.2 Experimental Section	61
1.2.1 Hybrid quadrupole time-of-flight mass spectrometer	61
3.2.2 In ⁺ SIMS.....	62
3.2.3 C ₆₀ ⁺ SIMS.....	62
3.2.4 Preparation of cholesterol films	63
3.2.5 Relative quantification	63
3.3 Results and Discussion.....	64
3.3.1 Cholesterol Fragmentation in SIMS Analysis.....	64
3.3.2 Isobaric Interferences and Contamination.....	69
3.3.3 Isobaric interferences in cell imaging	71
3.3.4 Imaging with fragments	75
3.4 Conclusions.....	77
3.5 References.....	78
Chapter 4 ToF-SIMS Imaging of Sub-Cellular Lipid Heterogeneity: Poisson Counting and Spatial Resolution	80
4.1 Introduction.....	80
4.2 Materials and Methods.....	82
4.2.1 Cell preparation for imaging	82
4.2.2 Mass spectrometer.....	83
4.2.3 Data collection and image analysis	84
4.2.4 Model calculations	84
4.3 Results and Discussion.....	86
4.3.1 SIMS imaging of homogenous surfaces.....	86
4.3.2 Probability mass functions and spatial resolution	86
4.3.3 The effect of ionization efficiency and concentration change.....	90
4.3.4 Using histograms to interpret imaging data	93
4.3.5 Single cell imaging of RBL-2H3 mast cells.....	93
4.3.6 Single cell histograms	97
4.3.7 Matrix effects in single cell plasma membrane imaging.....	100
4.3.8 Distribution of cholesterol in RBL-2H3 mast cells.....	102
4.4 Conclusions.....	104
4.5 References.....	105

Chapter 5 Mass spectrometry imaging of mating <i>Tetrahymena</i> : changes in cell morphology regulate lipid domain formation	107
5.1 Introduction.....	107
5.2 Material and Methods	111
5.2.1 Mating Tetrahymena	111
5.2.2 Trituration.....	111
5.2.3 Cell Counting	112
5.2.4 SIMS imaging	112
5.2.5 Region of interest analysis	113
5.2.6 Line scans and intensity calculation.....	113
5.3 Results and Discussion.....	114
5.3.1 Lipid domain formation correlates to pore formation	114
5.3.2 Trituration determines time scale for strong pair formation	117
5.3.3 Mass spectrometry imaging shows that weakly bound cells do not display lipid domains	117
5.3.4 Domains become more prominent over time	119
5.3.5 Domain formation correlates to trituration resistance	122
5.4 Conclusion	122
5.5 References.....	123
Chapter 6 Cluster Bombardment to Recover Spatial Chemistry after Preparation of Biological Samples for SIMS Imaging	125
6.1 Introduction.....	125
6.2 Materials and Methods.....	126
6.2.1 C ₆₀ ⁺ SIMS.....	126
6.2.2 Preparation of cholesterol films	127
6.2.3 Preparation of mouse embryo slices.....	127
6.3 Results and Discussion.....	128
6.3.1 Modeling water deposition in biological analysis	128
6.3.2 Analysis of mouse embryos	131
6.4 Conclusion	137
6.5 References.....	137
Chapter 7 Summary and Future Directions.....	139
7.1 Summary	139
7.2 Future Directions.....	142
7.2.1 Tandem MS experiments in SIMS	143
7.2.2 High mass resolution and mass accuracy	146
7.2.3 Increased imaging area.....	146
7.2.4 Increased duty cycle	149
7.3 Conclusions.....	150
7.4 References.....	150
Appendix A Imaging Instrumentation and Procedure	152
Appendix B Matlab Scripts for Data Processing	156

Script 1, Thresholding.....	156
Script 2, Nearest-neighbor smoothing.....	156
Script 3, Intensity binning.....	157
Script 4, Population selection.....	158

LIST OF FIGURES

Figure 1-1: Schematic of the sputtering process. For most of the imaging experiments the incident particle is In+.....	2
Figure 1-2: Schematic of a linear ToF. All ions are given the same acceleration energy and thus the smaller ions travel faster through the field free region and strike the detector first.	4
Figure 1-3. Schematic of the image acquisition process. The primary ion beam is scanned across the analysis surface generating a series of mass spectra. Features in the spectrum can be highlighted and the pixels pseudo-colored to produce a chemical-specific image.....	5
Figure 1-4. A simple schematic of the Kratos instrument used for the majority of experiments.	6
Figure 1-5. Schematic diagram of the modified QSTAR XL hybrid QqTOF mass spectrometer. ⁴	8
Figure 1-6. Generalized structure of a phospholipid. The molecules in the alcohol column can be substituted in the blue circle in the cartoon of phospholipid structure. The fatty acids column depicts some of the most common “tailgroups” found in mammalian membranes and is substituted in the green rectangles.....	10
Figure 1-7. (A) Structure of cholesterol (B) Structure of tetrahymenol.....	12
Figure 1-8. A cartoon representation of lipid polymorphism and its’ dependence on molecular geometry.....	15
Figure 1-9. Cartoon representation of the fluid mosaic model of the membrane. Peripheral and integral membrane proteins freely diffuse through a randomized solvent of phospholipids. Also note that lipids make up only about 50% of most membranes.	16
Figure 1-10. The “stalk” intermediate which is proposed to form during membrane fusion. Hexagonal II lipids, shown in red, concentrate in high curvature area to stabilize the structure.	18
Figure 1-11. Graphic representation of protein segregation by lipid rafts that is relevant to IgE receptor signal initiation. (A) Distributions of relevant membrane components in unstimulated cells. (B) Distributions of relevant components following signal initiation by antigen-mediated IgE receptor crosslinking. This Figure is taken from Holowka, et. al. ¹¹	19

- Figure 1-12.** Freeze-dried *Tetrahymena* cells directly from culture medium. The images shown are (A) optical brightfield, (B) SEM, (C) total positive ions and (D) m/z 28 (blue) and m/z 184 (green – barely visible). Scale Bars represent 25 μm . All SIMS images were recorded using 15 keV In^+ ion bombardment.22
- Figure 1-13.** *Tetrahymena* cells, rinsed in 18 Mohm water, and then freeze dried. (A) optical brightfield. (B) m/z 28 (blue) and m/z 184 (green). Scale Bars represent 25 μm . The SIMS image was recorded using 15 keV In^+ ion bombardment.....23
- Figure 1-14.** Freeze-dried *Tetrahymena* cells revealing hidden damage (A) SEM. (B) m/z 28 (blue), m/z 184 (green), and m/z 69 (red). Scale Bars represent 25 μm . The SIMS image was recorded using 15 keV In^+ ion bombardment.25
- Figure 1-15.** Total ion SIMS images of rinsed and freeze-dried *Tetrahymena* cells. The primary ion is (A) 15 keV In^+ , (B) 20 keV Au^+ , (C) 20 keV Au_3^+ and (D) 20 keV C_{60}^+ . Scale Bars represent 25 μm26
- Figure 1-16.** Mixed Glia – Oligodendrocytes and Astrocytes lyophilized in trehalose. From the total ion SIMS image acquired using Au^+ bombardment in (A), the morphology of the cell is seen to be preserved. The total ion SIMS image in (B) was acquired using C_{60} bombardment. The molecule-specific images from Au^+ and C_{60}^+ bombardment are shown in (C) and (D), respectively. The scale bars represent 50 μm . Data taken by Shawn Parry.....28
- Figure 1-17.** Application of C_{60}^+ bombardment to remove water layer. (A) Macrophage on Si with water overlayer. PC (m/z 184) is shown in green and (m/z 18) is shown in blue. (B) Smaller crater etched away showing cholesterol localization using a dose of 10^{13} ions/ cm^2 . Red is (m/z 28) to denote the Si substrate that has been uncovered. Scale bars are 25 μm31
- Figure 1-18.** Chemical images of mating *Tetrahymena* cells, taken with differing ice thicknesses. (A,C,D) m/z 69, and (B,D,F) m/z 184. The sample (A,B) was fractured from a sandwich structure that produced a layer of ice thick enough to exhibit charging. The sample (C,D) contained a very thin ice layer that induced topographical artifacts. The sample in (E,F) has an ice thickness that produces results free of artifacts. Scale bars represent 25 μm . Data taken by Michael Kurczyk....33
- Figure 2-1.** (A) Brightfield image of rat oligodendrocyte in culture. (B) Brightfield image of an oligodendrocyte cultured and silicon and cryogenically preserved using the described sample preparation method. (C) SIM image of rat oligodendrocyte. (D) SIMS image of a preserved oligodendrocyte, m/z 184(PC) green, m/z 28(Si) blue, intensity scale 0-4. (E) Brightfield image of oligodendrocyte that has been warmed to allow crystallization. (F) SIMS image of a corresponding area shown in (E), m/z 184(PC) green, m/z 28(Si) blue, intensity scale 0-2. Images were obtained using an In^+ primary ion beam, all scale bars are 20 μm44
- Figure 2-2.** (A) Total ion image of a patterned cholesterol film prior to deposition. (B) SIMS image overlay from (A) m/z 369 (Cholesterol) green, m/z 28 (Si). (C) Total ion image of patterned cholesterol film after water deposition. (D) SIMS image

- overlay from (C) m/z 369 (Cholesterol) green, m/z 28 (Si). Thermal intensity scale from black to white, 0-20 counts. Scale bars represent 25 μm . (E) Line scans displaying intensity of cholesterol ion as a function of distance across image “Before” and “After” water deposition as indicated by the lines in part B and D.46
- Figure 2-3.** (A) 3D-AFM image of patterned cholesterol film before water deposition, FOV 100 μm^2 , to the right is an average cross-section of the film (B) 3D-AFM image of patterned cholesterol film after water deposition and removal, FOV 100 μm^2 , to the right is an average cross-section of the same region as above.48
- Figure 2-4.** Histogram summarizing results of deposition experiments utilizing a cold finger to control the deposition of water. Control intensity represents the signal intensity of m/z 184 (PC Headgroup) on a dry lipid film. “Cooled with Trap” intensity represents signal intensity of m/z 184 when a cold finger was cooled in the sample chamber prior to sample cooling, thus limiting the deposition of water. “Cooled No Trap” intensity represents the signal intensity of m/z 184 (PC Headgroup) after cooling the stage without employment of a cold finger.....52
- Figure 2-5.** Relative intensity of PC headgroup as water is deposited on the surface of a spin coat lipid film. Relative intensity of m/z 18 is plotted to demonstrate increasing H₂O on the surface.53
- Figure 2-6.** (A) SIMS overlay, m/z 184(PC) in green and m/z 18(H₂O) in blue, of 2 macrophages on a silicon substrate prepared by freeze-etching, intensity scale from 0-3. (B) SIMS image of m/z 834 showing DiI intercalated into the macrophage membrane, intensity scale 0-2. Scale bars represent 15 μm55
- Figure 3-1.** Mass spectra of cholesterol films. (A) In⁺ induced spectrum of a PVD cholesterol film. (B) MS/MS spectrum of [M-OH]⁺ ion derived from pure cholesterol film using N₂ as a collision gas. All spectra are standardized to largest peak in the viewing area.....65
- Figure 3-2.** Proposed fragmentation scheme for cholesterol from MS/MS analysis.68
- Figure 3-3.** Discriminating contaminant peaks. (A) Mass spectrum generated from the PDMS coated sample. (B) Mass spectrum generated from the cholesterol coated sample. (C) Orthogonal ToF-SIMS imaging of the junction of two sample plates; one coated with cholesterol (m/z 147.117 = blue), and one coated with PDMS (m/z 147.065 = green). (D) Resulting mass spectrum with m/ Δ m resolution of 8000. Data taken by Anthony Carado.70
- Figure 3-4.** Cholesterol fragment ion intensity versus distance. Line scans of cholesterol fragment ion intensity across two cells demonstrates the uniformity of the internal standard use for quantification. The inset shows the path of the line scan which begins in the bottom left. The cell to the bottom left was treated with cholesterol vs. the cell above which was control. Original data taken by Sara Ostrowski.74
- Figure 3-5.** SIMS imaging of macrophage cells. SIMS overlay images of the Cholesterol fragment ions (Yellow) vs. Na m/z 23(Red), green pixels denote the

- presence of both ions on macrophages. All scale bars are 10 μm . A.) m/z 369 B.) m/z 161 C.) m/z 147 D.) m/z 109 E.) m/z 95.....76
- Figure 4-1.** (A) Mass-specific image of PC from POPC LB film. (B) Histogram of signal intensity for $(m/z)^+$ 184 in a Langmuir Blodgett film composed of POPC. Scale bar represents 100 μm87
- Figure 4-2.** (A) Probability mass function for imaging cholesterol, assuming 100% concentration change between pixels, with 310 nm spatial resolution. (B) Probability mass function of two discrete populations where concentration 1 gives an average intensity of 2.67 counts and concentration 2 gives an average intensity of 5.33 counts. (C) Probability mass function for imaging cholesterol, assuming 100% concentration change between pixels, with 1.2 μm spatial resolution. (D) Probability mass function for imaging cholesterol, assuming 100% concentration change, down-binned to 2.79 μm spatial resolution.89
- Figure 4-3.** (A) z-score as a function of lateral resolution for various lipid ionization efficiencies. The change in concentration was held constant at 100%. (B) z-score as a function of change in lipid species concentration. For this plot, a spatial resolution of 1.2 μm was used, which corresponds to a z-score of 3, or 90% separation, for our cholesterol simulation. The numbers in the legends are ionization efficiencies.91
- Figure 4-4.** (A) Mass-specific image of cholesterol $(m/z)^+$ 147 in the ternary mixture of PC, sphingomyelin, and cholesterol. (B) Histogram for signal intensity of cholesterol $(m/z)^+$ 147 in a ternary mixture of PC, sphingomyelin, and cholesterol. The black line gives the predicted Poisson distribution using the average signal intensity. The red line gives the curve predicted by the Poisson distribution the 2 populations shown in (C) and (D). (C) Map of pixels which have a cholesterol signal intensity of 0-2 counts, population 1. (D) Map of pixels which have a cholesterol signal intensity of 4-10 counts, population 2. Scale bars represent 100 μm94
- Figure 4-5.** Mass-specific ToF-SIMS images of a RBL-2H3 mast cell. (A) PC $(m/z)^+$ 184, (B) cholesterol $(m/z)^+$ 147, (C) PE $(m/z)^+$ 142, and (D) PPC $(m/z)^+$ 224. Scale bars represent 10 μm96
- Figure 4-6.** Histograms of the four lipid masses mapped in Figure 4-5. Histograms are the result of 452 pixels. The theoretical Poisson distribution, generated using the average pixel intensity, is overlaid in black. (A) $(m/z)^+$ 184, PC, (B) $(m/z)^+$ 147, CH, (C) $(m/z)^+$ 142, PE, and (D) $(m/z)^+$ 224, PPC.....99
- Figure 4-7.** Pixels in the top 10% of signal intensity for (A) PC $(m/z)^+$ 184, (B) Cholesterol (CH) $(m/z)^+$ 147, (C) PE $(m/z)^+$ 142, and (D) phospholipid only derived PC $(m/z)^+$ 224. (E) Overlay of a-d. (F) Histogram of the coincidence of high intensity lipid signals. The extended color legend can be seen below the histogram. Scales bars represent 10 μm101
- Figure 4-8.** (A) A plot of correlation coefficient vs. number of weighted distributions used to fit cholesterol intensity distribution histograms. (B) Representative cholesterol histogram with 3 parameter fit shown in solid black, $R^2=0.98$. (C) The 3

curves that compose the 3 parameter fit shown in 6B. (D) Bar plot demonstrating the expected surface coverage for each cholesterol intensity population. (E) Reconstructed cell image displaying the locations of the three populations on the surface. Black outline corresponds to the boundary of the cell defined by the PC signal, which was used to generate the histogram. Color scheme for populations is conserved from (D). For this image, Population 1 is defined as pixels containing intensities 0-3, Population 2 is 4-7, Population 3 is 8-13. Scale bar is 10 μm . For (a) and (d), $n = 5$, and error bars denote standard deviations. 103

Figure 5-1. Schematic of two domain formation scenarios for mated *Tetrahymena thermophila*. Heterogeneously distributed lipids in the plasma membranes of *Tetrahymena thermophila* may form as a result of (red arrow) or in anticipation of pore formation (blue arrows). Black lipids are cylindrical, blue are H II and green are lysolipids. 109

Figure 5-2. Sims analysis of a strongly paired mated *Tetrahymena thermophila*. (A) Differential interference contrast microscopy image of a mating cell pair (scale bar = 25 μm). (B-D) SIMS images of a triturated pair of mating *Tetrahymena thermophila*. C5H9 is mapped in B PC is mapped in C and 2-AEP is mapped in D the intensity in the 2-AEP image has been multiplied by 3. (E) Region of interest analysis of the same cells. The red mass spectrum is from the cell bodies and the green mass spectrum is from the junction. The inset highlights the regions on the SIMS image, red for the cell bodies and green for the junction. Data collected by Mike Kurczy..... 115

Figure 5-3. Temporal evolution of the observed lipid domain formed during cell conjugation. (A) The percent cells paired plotted over time under quiescent conditions and the percent of cells paired following trituration. (B-I) SIMS images and line scans of mated *Tetrahymena thermophilla* at three time points following the initiation of mating. The molecular fragment ion images of PC (m/z 184) for cell pairs imaged at (B) 1 hour, (D and F) 2 hours and (H) at 3 hours. (C, E, G, I) The corresponding line scans for PC and the m/z 69 intensity (ubiquitous hydrocarbon fragment C_5H_9) as control ¹⁴. Each time point taken across the junction is shown below each image. Line scans were treated with 25 % Savitzky-Golay smoothing. Data collected by Mike Kurczy..... 118

Figure 5-4. The percent of paired cells displaying lipid domains over time vs. the percent of paired cells that resisted separation following trituration. Three time points were investigated 60 min ($n = 6$), 120 min ($n = 9$), and 180 min ($n = 4$). Domains were defined as a decrease in phosphocholine at the junction between cells ¹⁴. Line scans of PC intensity were used to measure this decrease. The appearance of a trough was used to determine that a pair had formed a lipid domain. Data collected by Mike Kurczy and Craig Van Bell. 121

Figure 6-1. A cartoon diagram of physical vapor deposited patterned cholesterol film. 129

Figure 6-2. (A) 3D schematic of patterned cholesterol film. (B) 3D schematic of patterned cholesterol film that has been covered by deposited water. (C) 3D schematic of patterned cholesterol film after deposition and subsequent removal of

- water. (D) 3D schematic of patterned cholesterol film illustrating imaging area after deposition and removal of water. 130
- Figure 6-3.** (A) Positive SIMS image of patterned cholesterol film on silicon created using physical vapor deposition, m/z 369 shown in green and m/z 28 in red. (B) The film was then cooled in vacuum (-196°C) and water was allowed to deposit, m/z 18 shown in blue and m/z 369 in green. The cholesterol layer is almost completely covered in water. (C) After etching with a dose of 10^{13} C_{60}^{+} ions/ cm^2 the patterned film beneath is revealed with maintained spatial integrity. (D) Line scans across the film features reveal that the distribution of cholesterol on the surface is maintained when C_{60}^{+} is used to remove the water overlayer versus when the surface is not cleaned with the C_{60}^{+} nanotome. Scale bars are $25\ \mu\text{m}$ 132
- Figure 6-4.** (A) Scanning ion image (SIM) of an axial slice from a 9-day-old mouse embryo. The gut and the genital ridge are identified by white arrows. The images in (B) and (C) are SIMS images of cholesterol (m/z 366-370) from the tissue in the SIM image. The image in (B) was taken prior to a sputter dose of 1×10^{13} $\text{C}_{60}^{+}/\text{cm}^2$ and the image in (C) was taken after nanotome sputtering. Scale bars are $100\ \mu\text{m}$. Data collected by Michael Kurczy. 134
- Figure 7-1.** MS/MS SIMS analysis of the amino acids D-Leucine (Leu) and Isoleucine (Ile) (A) The two structural isomers (Leu) and (Ile). (B) MS/MS SIMS image of the junction of two different thin films on silicon shards. The chemical image of M+H does not reveal the identities of the thin films as m/z^{+} 132.10 maps to both shards. (C) MS/MS of m/z^{+} 132.10 reveals the fragment ion m/z^{+} 69.07 only comes from Ile, and so can be used to show that Ile is on the left, while Leu is on the right. (D,E) The MS/MS spectra of Leu and Ile are shown, respectively. Data collected by Anthony Carado. 144
- Figure 7-2.** (A) Dynamic secondary ion image of a single aplysia cell with phosphate background in red, vitamin E in blue, and cholesterol in green. Cell diameter is approximately $350\ \mu\text{m}$. (B) CID spectrum of vitamin E from a single aplysia cell. (C) SIMS neat thin film reference MS/MS spectrum of vitamin E. (D) Fragmentation points of vitamin E. Data collected by Anthony Carado. 145
- Figure 7-3.** Mass range m/z^{+} 119.5-124.5 for a mouse brain slice. Data Collected by Anthony Carado. 147
- Figure 7-4.** Secondary ion image of a rat brain slice using successively smaller step sizes to demonstrate the versatility of SIMS imaging with this platform. Phosphatidylcholine headgroup ion m/z^{+} 184.07 is shown in green while cholesterol pseudo-molecular ion m/z^{+} 369.35 is shown in blue. The white dashed line indicates the region of greater magnification in the following image. Data Collected by Melissa Passarelli. 148

LIST OF TABLES

Table 2-1. Normalized intensity of characteristic lipid fragments before (Control), and after low temperature water matrix deposition (Cold Film).....	49
Table 3-1. Signal intensity of fragments reported as percentage of pseudomolecular ion intensity.....	67
Table 3.2. Relative cholesterol increase in treated cells utilizing the identified fragments. ..	73
Table 4-1. Reduced χ^2 values for lipids imaged in RBL-2H3 Cells.....	98
Table 5-1. Summary of relative PC intensities across mating <i>Tetrahymena thermophila</i>	120
Table 6-1. Percent of ion signal following a sputter dose of $1 \times 10^{13} \text{ C}_{60}^+/\text{cm}^2$	136

PREFACE

The following material from this thesis has been adapted for publication.

Chapter 1

M. E. Kurczy, **P. D. Piehowski**, S. A. Parry, M. Jiang, G. Chen, A. G. Ewing and N. Winograd, "Which is More Important in Bioimaging SIMS Experiments - The Sample Preparation or the Nature of the Projectile?", *Appl. Surf. Sci.*, **2008**, 255, 1298-1304.

Michael L. Heien, **Paul D. Piehowski**, Nicholas Winograd, Andrew G. Ewing. "Lipid detection, identification, and imaging single cells with SIMS". *Mass Spectrometric Imaging. History, Fundamentals and Protocols*, Humana Press Methods in Molecular Biology Series. In Press.

Chapter 2

P.D. Piehowski, M.E. Kurczy, D. Willingham, S. Parry, M.L. Heien, N. Winograd, A.G. Ewing, "Freeze-Etching and Vapor Matrix Deposition for ToF-SIMS Imaging of Single Cells", *Langmuir*, **2008**, 24, 7906-7911.

Chapter 3

P. D. Piehowski, Anthony J. Carado, Michael E. Kurczy, Sara G. Ostrowski, Michael L. Heien, Nicholas Winograd, Andrew G. Ewing, "MS/MS Methodology to Improve Sub-Cellular Mapping of Cholesterol Using ToF-SIMS", *Anal. Chem.*, **2008**, 80, 8662-8667.

Chapter 4

P.D. Piehowski, Michael L. Heien, Angel M. Davey, Erin D. Sheets, Nicholas Winograd, Andrew G. Ewing, "Mass Spectrometry Imaging of Sub-Cellular Features: Poisson Counting and Spatial Resolution". *Anal. Chem.* **2009**, 81, 5593-5602.

Chapter 5

Michael E. Kurczy, **P. D. Piehowski**, Michael L. Heien, Craig T. Van Bell, Nicholas Winograd and Andrew G. Ewing, “Lipid Domain Formation is Necessary for Irreversible Conjugation in *Tetrahymena thermophila*”. Submitted, *PNAS*.

Chapter 6

Michael E. Kurczy, **P.D. Piehowski**, Michael L. Heien, Kathleen Molyneaux, Nicholas Winograd, Andrew G. Ewing, “Utilizing the Unique Properties of Cluster Ion Projectiles to Increase the Reproducibility of Sample Preparation for Biological SIMS Imaging”. Submitted, *JASMS*.

ACKNOWLEDGEMENTS

I would like to start by thanking my wonderful wife. She has been extremely supportive and patient during the long years of graduate school induced poverty. Thanks for always being there for me in the tough times and reminding me of the things that are most important in life. I dedicate this thesis to you and our future family.

My parents have been a great source of support for me and my education. In our house, education was always priority number one. Whether it was help with a school project or taking an extra job to pay for private school tuition, my parents made sure that I was learning and challenging myself. Thank You, I could not have done it without you.

I would like to acknowledge my research advisor, Andy Ewing for his support and guidance. His passion for science was truly contagious and motivational. He supplied me with everything that I needed to succeed in graduate school and become a member of the scientific community. He gave me the opportunity to attend numerous scientific meetings and brought me to Sweden to participate in exciting new research projects. This not only enhanced my training but also my overall life experience. Thank you for providing an exceptional graduate study experience.

I owe a debt of gratitude to our collaborator Professor Nick Winograd, who treated me like one of his own students. He has been extremely gracious in allowing me to utilize his equipment and resources to complete my research. I was very lucky to have his additional guidance and scientific insight.

Special thanks must go to Dr. Michael Heien. Michael came to Andy's lab at the end of my 3rd year in graduate school, and has been an incredible help. Without his help and guidance

this thesis would look very different. In addition, he had a large role in getting my research on the right path, greatly accelerating my progress. Without him I would still be trying to make sense of my data. Thank you for being a wise mentor and a good friend. I must also make special acknowledgement to Dr. Michael Kurczy. Mike taught me everything I know about ToF-SIMS and Kratos. He is also responsible for much of the data presented in chapters 5, and 6 of this thesis. Mike's sense of humor made it a pleasure to work in Kratos lab, even after long strings of failed freeze-fracture experiments. Thanks.

I would like to thank all the members of the Ewing and Winograd research groups, past and present, for their help and support. Special mention to Dr. Dave Willingham and Anthony Carado whose expertise and collaboration was extremely valuable throughout my time at Penn State. I need to thank Dr. Christine Keating and Dr. Carlo Pantano for taking time out of their busy schedules to be on my doctoral committee. In addition, I would like to thank Sabrina Glasgow and Tammy Sauter for all their behind the scenes efforts to make things run smoothly for me.

For the many people I missed... I would like to acknowledge all the people that have given their time to teach and support me throughout the course of my personal and professional life, without whom, this achievement would not have been possible.

Last but certainly not least, I would like to thank the Saeco® Vienna Superautomatica. Those early morning cups of delicious, liquid concentration played a vital role in the completion of my thesis work.

Chapter 1

Investigating Lipid Heterogeneity in Single Cells with Time-of-Flight Secondary Ion Mass Spectrometry

1.1 Introduction

In this thesis, the study of cellular membranes using time-of-flight secondary ion mass spectrometry, ToF-SIMS, imaging is discussed. This chapter provides an introduction to initiate the reader to ToF-SIMS imaging and the system of interest. It begins with a basic discussion of the technique, followed by lipids and the bilayer membranes that they form. The second half discusses sample preparation and experimental details pertinent to the analysis of lipids using ToF-SIMS.

1.2 Time-of-flight secondary ion mass spectrometry

ToF-SIMS is an analytical technique which creates ions for analysis through the bombardment of a sample surface with a beam of energetic ions, referred to as primary ions. The ions are generated in a source colloquially referred to as an “ion gun”. This beam is generated, in our case, by the field ionization of liquid indium to generate In^+ ions. The ions are accelerated by an electric field and directed at the surface by a series of ion optics.¹ The energy of the primary ion is transferred to the analysis surface through a series of collisions, called a collision cascade, which ejects ions, called secondary ions, and molecules from the surface, Figure 1-1. Because of the low energy nature of the down-stream collisions that eject particles, over 95% of the secondary ions emitted are from the top two atomic layers of the solid.² The bombardment process is inherently destructive. As a result, ToF-SIMS images are generally obtained in the

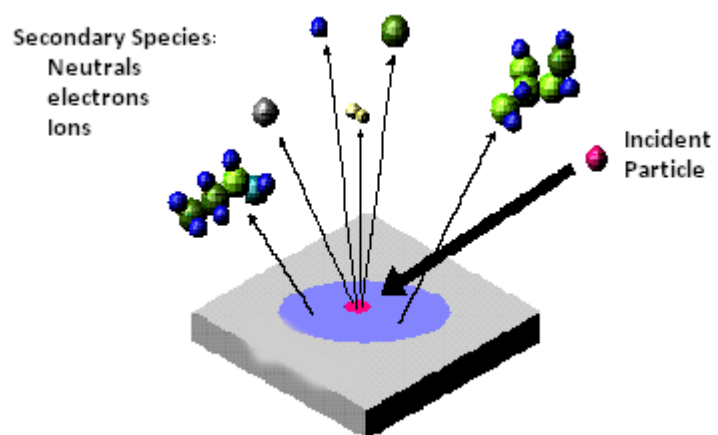


Figure 1-1: Schematic of the sputtering process. For most of the imaging experiments the incident particle is In^+ .

static mode. Static mode is defined as fewer than 10^{13} ion impacts/cm², or 1 impact per 100 surface atoms or ions. This limits the primary ion dosages usable, but ensures that the mass spectrum obtained is a relevant representation of the native sample surface. Unfortunately, the vast majority of the species ejected are neutrals which are not analyzable by mass spectrometry, further limiting the amount of material available for detection.³

These ions generated are collected and analyzed with a time-of-flight (ToF) mass analyzer. For analysis, desorbed ions are accelerated into a field-free region by a uniform extraction voltage. The ion then travels through a field-free region of the analyzer and is detected with a microchannel plate (MCP). The drift time recorded can then be converted to a mass using the kinetic energy equation, because the energy is equal to the extraction voltage. A schematic of a linear ToF is shown in Figure 1-2. The bombardment process produces ions with a spread of kinetic energies, thus a reflectron ToF is utilized in most ToF-SIMS instruments. ToF analyzers are well suited for SIMS imaging experiments for two main reasons. First, they offer a virtually unlimited mass range giving them the flexibility to analyze wide variety of samples. Secondly, ToF analyzers offer parallel detection of all secondary ions giving very high sensitivity. This also means that the analyzer is always ready to detect ions of any mass and does not have to be tuned to a particular mass before analysis.³

The ion beams employed in SIMS can be focused to a small size, in our case as small as 200 nm, and directed at the analysis surface to obtain a mass spectrum. This lends to the possibility of microprobe imaging. To achieve this, the beam is raster-scanned across the surface collecting a mass spectrum at each position. These spectra are put together to form a chemically specific image of the sample. The analyst can then examine the mass spectrum obtained to display the location of ions of interest, Figure 1-3. A schematic of the Kratos instrumental setup is shown in Figure 1-4.

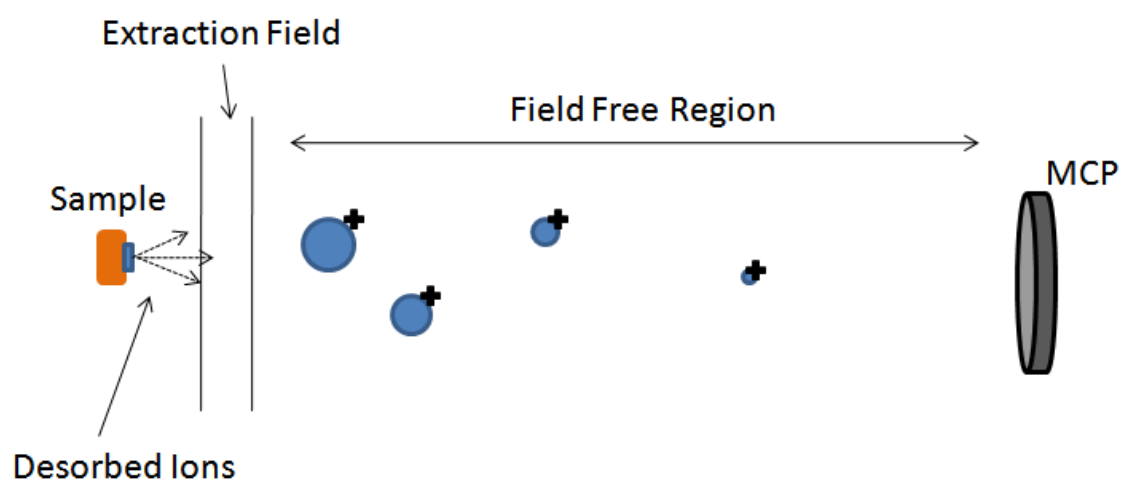


Figure 1-2: Schematic of a linear ToF. All ions are given the same acceleration energy and thus the smaller ions travel faster through the field free region and strike the detector first.

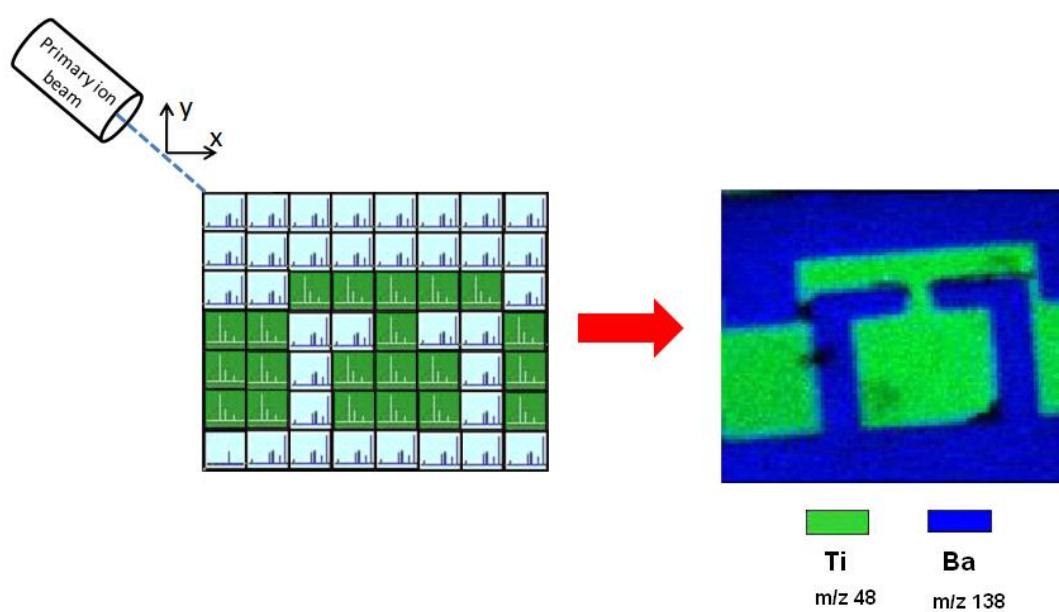


Figure 1-3. Schematic of the image acquisition process. The primary ion beam is scanned across the analysis surface generating a series of mass spectra. Features in the spectrum can be highlighted and the pixels pseudo-colored to produce a chemical-specific image.

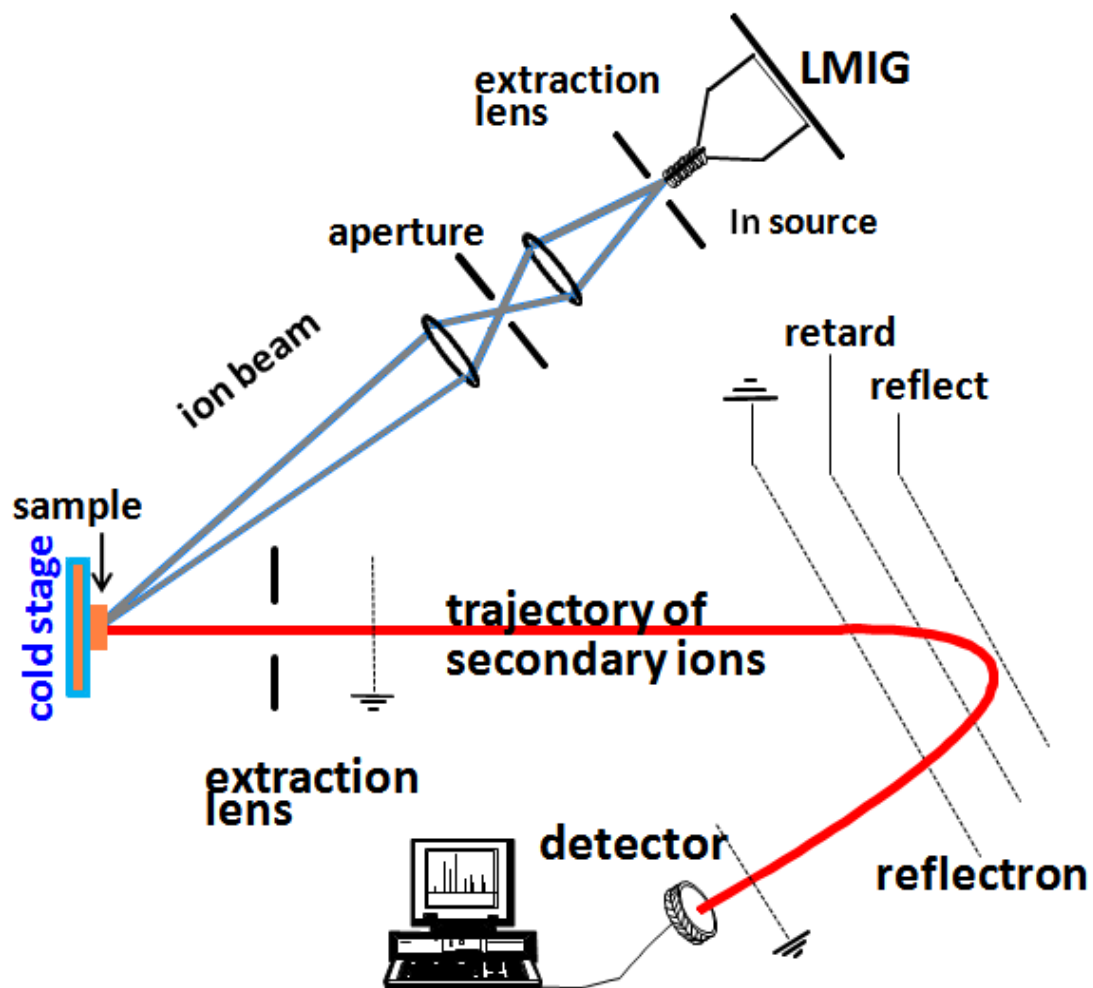


Figure 1-4. A simple schematic of the Kratos instrument used for the majority of experiments.

1.2.1 Hybrid quadrupole time-of-flight mass spectrometer

Recently, a new instrumental geometry has been utilized in the lab as illustrated in Figure 1-5. The triple-quadrupole-orthogonal-ToF design offers many advantages over the traditional ToF-SIMS design. Two important features are the improved mass resolution that results from the orthogonal ToF, and the MS/MS capability afforded by the addition of the quadrupoles.⁴ The instrument is also equipped with a 20 keV C_{60}^+ ion source, which has been shown to enhance high-mass ion yields when compared to In^+ .⁵ The implementation of these advantages to improve imaging experiments is discussed in Chapter 3, with details and future applications discussed in Chapter 7.

1.3 Building blocks of the cell membrane

1.3.1 Lipids

To understand the cell membrane and its complexity, it is important to understand the basic building blocks and the forces that hold them together. For this reason, it is important to begin with a discussion of the molecular structures that make the membrane possible, the amphiphiles. So named because they contain both hydrophobic, “water-fearing”, and hydrophilic, “water-loving”, components in their molecular structure. A complete review of membrane lipid structures is beyond the scope of this introduction, therefore the discussion will focus on two important types of lipid that are the focus of the aforementioned studies.

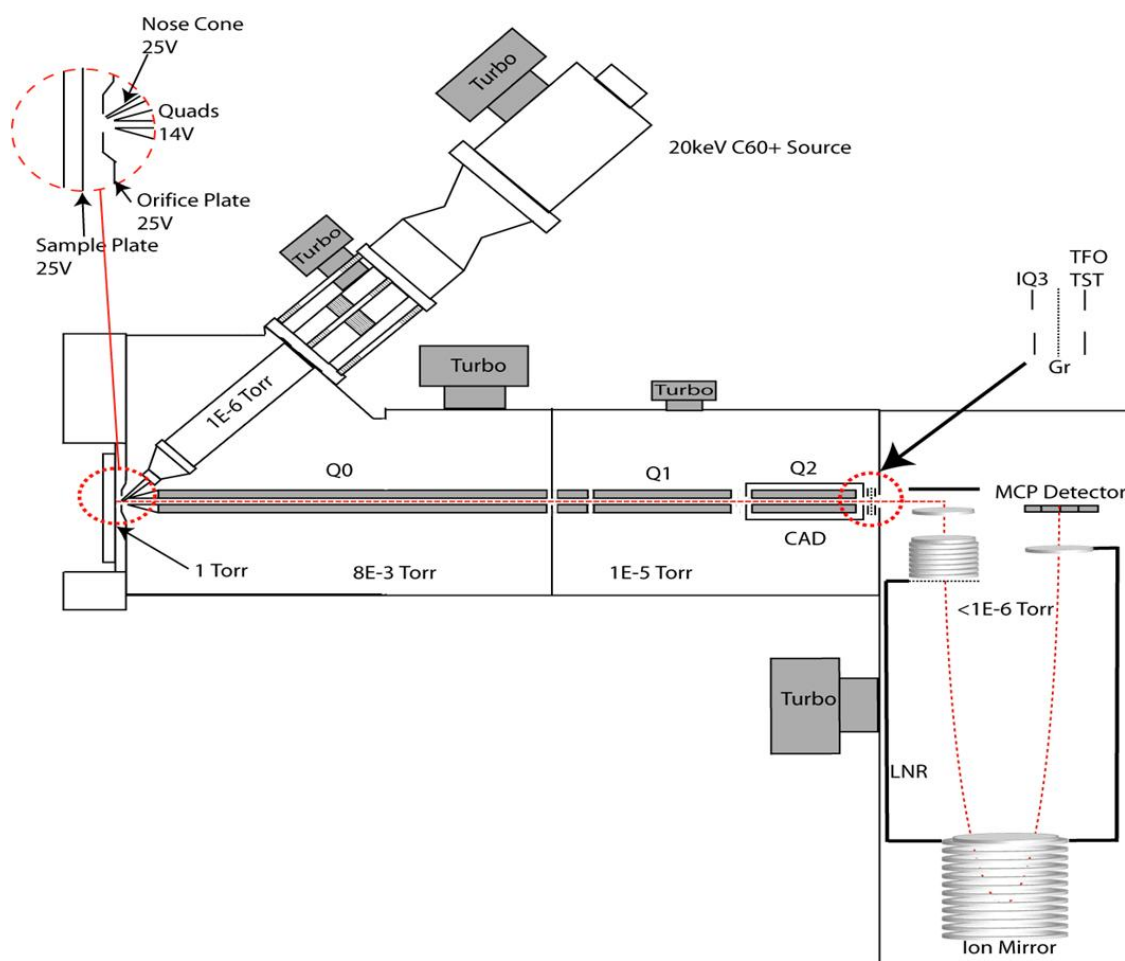


Figure 1-5. Schematic diagram of the modified QSTAR XL hybrid QqTOF mass spectrometer.⁴

1.3.2 Phospholipids

The best known and studied of the membrane lipids are the phospholipids.⁶ The phospholipids get their name from the phosphate group found in the polar region of the molecules. The polar phosphate moiety is esterified to an alcohol on one end and on the opposite end is esterified to a glycerol. The glycerol is then esterified to two nonpolar acyl chains. Commonly, the polar end of the phospholipid is referred to as the headgroup and the nonpolar end as the tailgroup. A generalized structure along with the most common constituents is shown in Figure 1-6.

Phospholipids are commonly identified by the headgroup attached to the phosphate using a simple naming scheme. If the headgroup is choline, the lipid is called phosphatidylcholine. Similarly, if the headgroup is ethanolamine, the lipid is called phosphatidyl ethanolamine. Derived from this simple scheme are the two letter monikers used for these molecules throughout this thesis, i.e. PC for phosphatidylcholine, and PE for phosphatidylethanolamine. The structure of the headgroup determines the charge that the lipid will carry. The phosphate moiety is deprotonated at physiological pH and thus carries a negative charge. In the case of choline and ethanolamine, the headgroup carries a positive charge to balance the phosphate resulting in a zwitterionic, neutral lipid. Glycerol and inositol, while polar, are neutral molecules and result in an overall negatively charged lipid. At physiological pH, serine is a zwitterion and also results in a net negatively charged lipid. These charges are important in determining the surface charge of the membrane as well as how the lipids interact with each other in an ordered structure. As we will discuss later, the size of the headgroup in relation to the rest of the molecule is also an important property when describing phospholipids.

Dividing lipids into classes by the headgroup represents only the first level of complexity in their structure. The second level involves the composition of the fatty acids that make up the

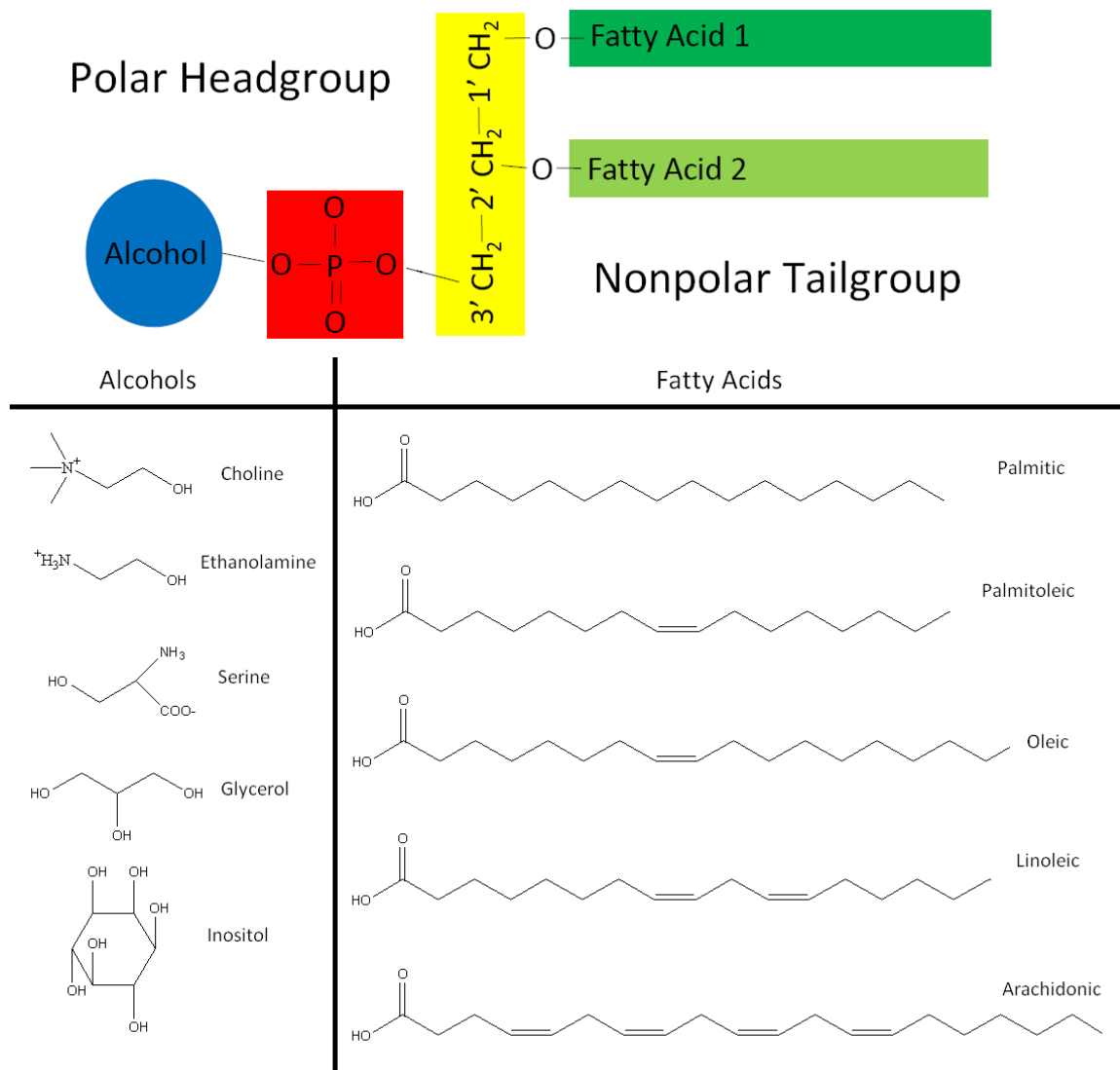


Figure 1-6. Generalized structure of a phospholipid. The molecules in the alcohol column can be substituted in the blue circle in the cartoon of phospholipid structure. The fatty acids column depicts some of the most common “tailgroups” found in mammalian membranes and is substituted in the green rectangles.

nonpolar region of the phospholipids. Figure 1-6 shows five fatty acids commonly found in the mammalian membrane, along with their common names. The full range of possible compositions ranges from as few as 12 to as many as 26 carbon atoms. In addition, the degree of unsaturation can range from 1 to 6. While these numbers represent the norm, many specialized deviations are found in nature.⁶ These common names can be placed in front of the phospholipid class to give a more complete description of the molecule. For example, a phosphatidylcholine with one palmitic acid and one oleic acid would be named palmitoyl-oleyl-phosphatidylcholine. When these structural details are known, a four letter abbreviation is commonly used, i.e. POPC for the molecule mentioned above. The distribution of fatty acids in a membrane is unique to the headgroup class as well as membrane type. It is important to note that this distribution is very important to the maintenance of a suitable membrane environment, though the complexity of this topic is beyond the scope of this introduction. Of importance to this work is the observation that the presence of a cis double bond introduces a kink in the chain structure, which affects the 3-dimensional character of the molecule.

1.3.3 Sterols

The second type of membrane lipid of importance to this work is sterols. In the case of mammalian cells, this specifically refers to cholesterol. *Tetrahymena thermophila* membranes do not contain cholesterol, but they utilize a structurally related molecule, tetrahymenol, which has been shown to play similar roles.⁷ The structures of cholesterol and tetrahymenol are shown in Figure 1-7. Although cholesterol is structurally much different than the phospholipids, it shares their amphiphilic nature. The structure consists of four fused rings which impart a rigid, planar character to the structure. The alcohol functionality attached to this ring system is the polar end

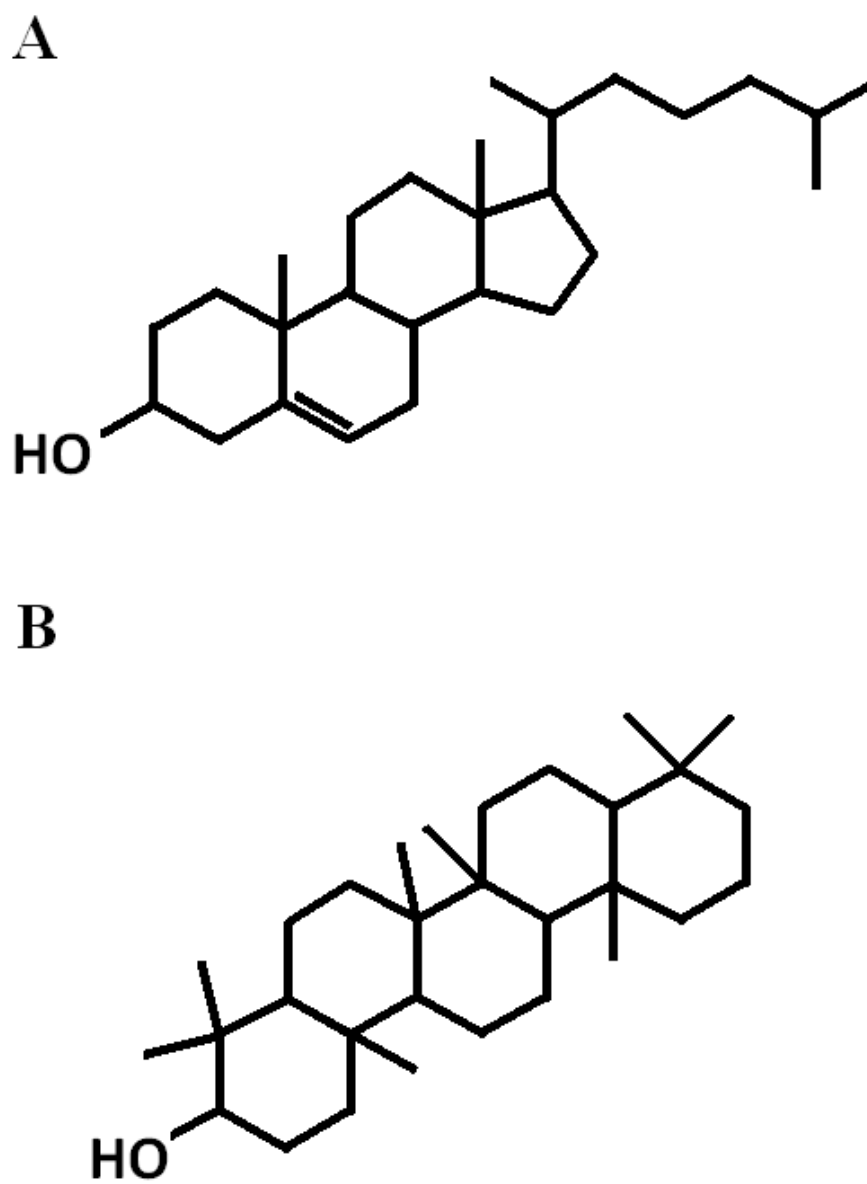


Figure 1-7. (A) Structure of cholesterol (B) Structure of tetrahymenol.

of the molecule. This unique structure leads to the many important roles that cholesterol plays in the mammalian membrane, which will be discussed in more detail later.

1.3.4 The hydrophobic effect

When amphiphiles come in contact with water, they are organized together by a force known as the hydrophobic effect. The assembly of cell membranes is an example of a self-assembly process in which amphiphilic molecules search for their state of lowest chemical potential. This state is achieved by forming intermolecular aggregates that allow for the nonpolar portions of the molecules to be sequestered from the watery environment of life. Thus, the hydrophobic effect is based on repulsion by the solvent molecules as opposed to attractive forces between the lipids themselves.⁸ This fact has very powerful biological consequences. It results in structures that are fluid and deformable, making them uniquely capable of serving as the semi-permeable, protein-rich barrier between the cell and the outside world.

“These essential properties of membranes-deformability and accommodation to appropriate insertions-would be virtually impossible to achieve if the permeability barriers that represent the first stage of compartmentalization were to be based on specific attractive forces, ‘bricks and mortar’, that normally lead to rigid inflexible structures. The fact that nature uses the hydrophobic force as the factor that creates compartments and the connectors between them is not an arbitrary choice. It is difficult to imagine it done in any other way.”

-Charles Tanford⁸

1.3.5 The bilayer membrane

The intermolecular aggregate that best minimizes the chemical potential is dependent on the geometry of the amphiphiles. A cartoon view of this concept is shown in Figure 1-8. Because the membrane lipid composition is predominantly phosphatidylcholine-like lipids the lamellar phase is favored, giving rise to the membrane bilayer. Nevertheless, hexagonal and hexagonal II lipids are present in the membranes of cells. In fact, these lipids are proposed to play an integral role in many cellular functions. Important to this work is their role in membrane fusion, which is a key component of the exocytosis process.

The membrane has been described by Singer and Nicholson as a “two-dimensional oriented solution of integral proteins in the viscous phospholipid bilayer solvent”.⁹ Their theory is known as the fluid mosaic model, and was the dominant theory in membrane biology until the mid 90’s. A cartoon of this model is shown in Figure 1-9. The idea of the lipids as a 2-D solvent has been useful to describe the dynamic state of the membrane; however, it does not explain the large diversity of lipid species present. Over the past 15 years it has become clear that this idea is an oversimplification of the complex role that lipids play in the membrane. It has been demonstrated that lipids are vital to many membrane processes including cell-cell communication, receptor-mediated signaling and membrane trafficking.¹⁰⁻¹⁸

1.3.6 Lipids and cellular communication

One example of cell-cell communication, and a central theme of much of the research described in this thesis, is regulated exocytosis. The process involves a membrane bound vesicle fusing with the cellular membrane in order to release its chemical contents into the extracellular space where it can be received by a neighboring cell. Successful signal transmission occurs only

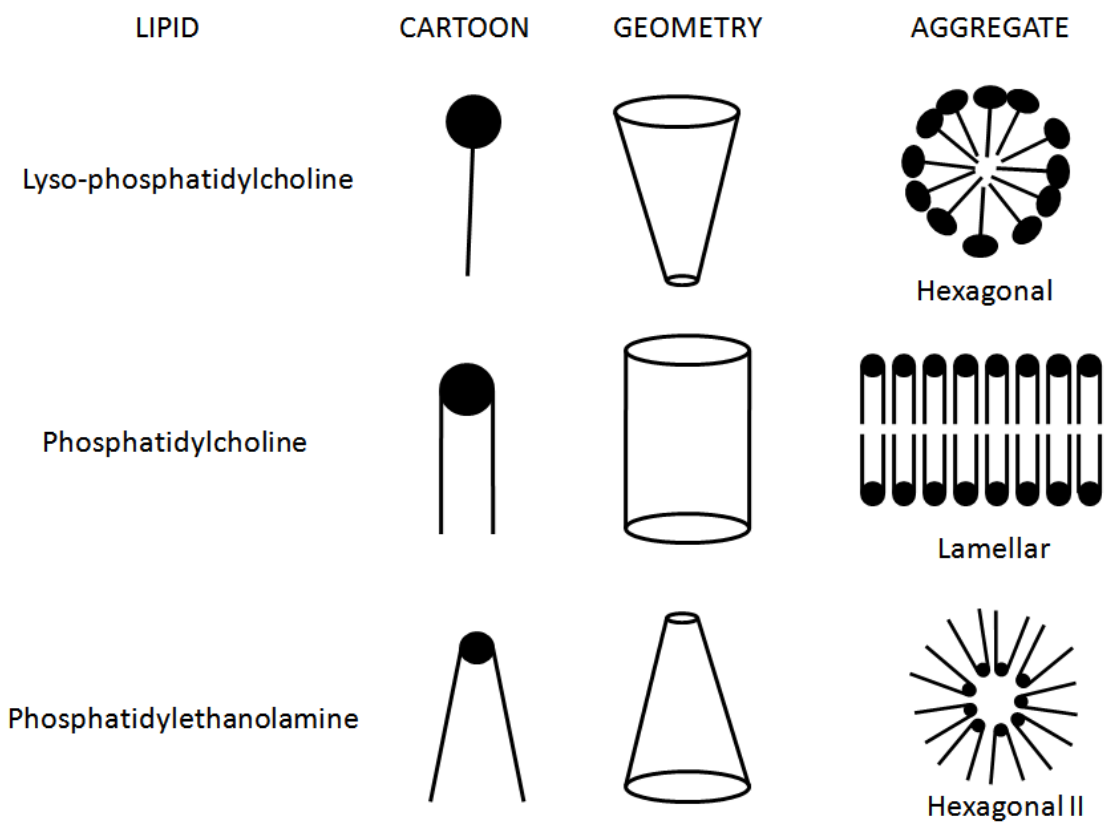


Figure 1-8. A cartoon representation of lipid polymorphism and its' dependence on molecular geometry.

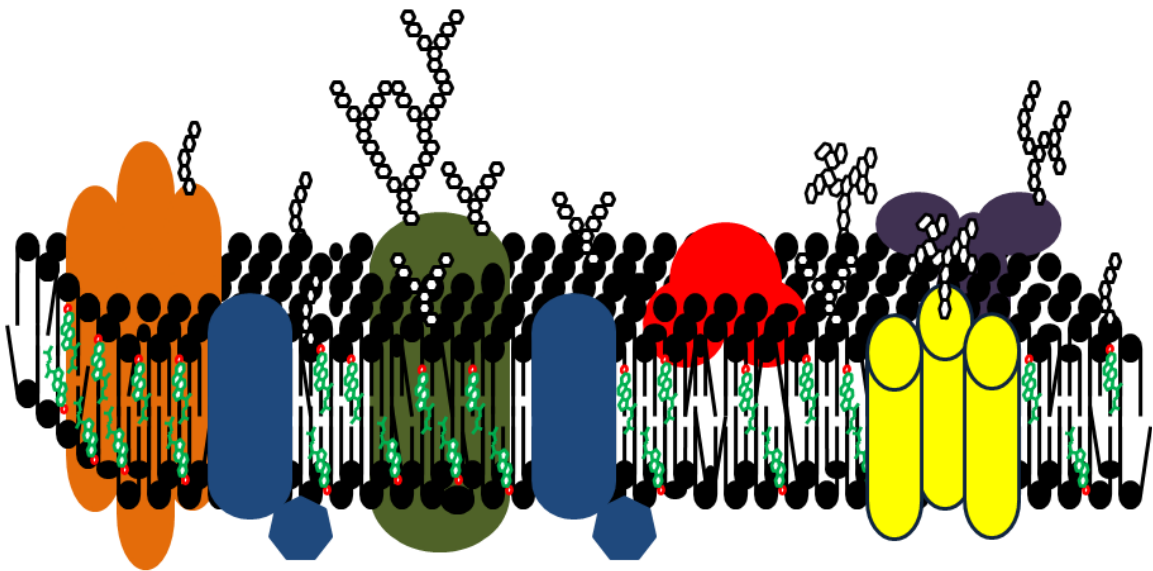


Figure 1-9. Cartoon representation of the fluid mosaic model of the membrane. Peripheral and integral membrane proteins freely diffuse through a randomized solvent of phospholipids. Also note that lipids make up only about 50% of most membranes.

through the collaboration of cytoskeletal elements, membrane bound proteins, and membrane lipids.^{12, 19} Experiments done with liposomes, a cell model devoid of protein and cytoskeleton, suggest that lipid composition plays a role in the fusion process.^{20, 21} Lipids are proposed to facilitate the formation of an intermediate structure necessary to the fusion process.²² This hypothesis is known as the stalk model.²³ A description of the structure of the “stalk” intermediate is shown in Figure 1-10. This model predicts that there will be an abundance of hexagonal II lipids present in the junction region of the two membranes. This conclusion is supported by SIMS imaging work done on the mated *Tetrahymena thermophila* model system, done by Ostrowski, et. al.¹⁴

Lipid composition can also play a role in receptor-mediated signaling. In the case of RBL-2H3 cells, it has been shown that lipid segregation plays a role in IgE receptor signaling.²⁴⁻²⁶ The term ‘lipid segregation’ refers to the separation of liquid-ordered (L_o) and liquid-disordered (L_d) phases in the membrane. L_o phases are caused by cholesterol-dependent lipid packing which increases the acyl chain order thereby slowing lateral diffusion.¹¹ They are characterized by higher concentrations of cholesterol and lipids with saturated acyl chains. In contrast, L_d phases are characterized by lower acyl chain order and increased lateral diffusion. These domains serve to segregate proteins from each other in a manner that facilitates signaling. A schematic of how this process is proposed to occur is shown in Figure 1-11. These experiments are the first of their kind in that they attempt the direct comparison of single pixels. This comparison necessitates the consideration of probability theory’s effect on the image obtained.

1.4 Sample Preparation

The study of lipid membrane heterogeneity in its native state represents a significant analytical challenge. The goal is to make chemically-specific measurements with sub-micrometer

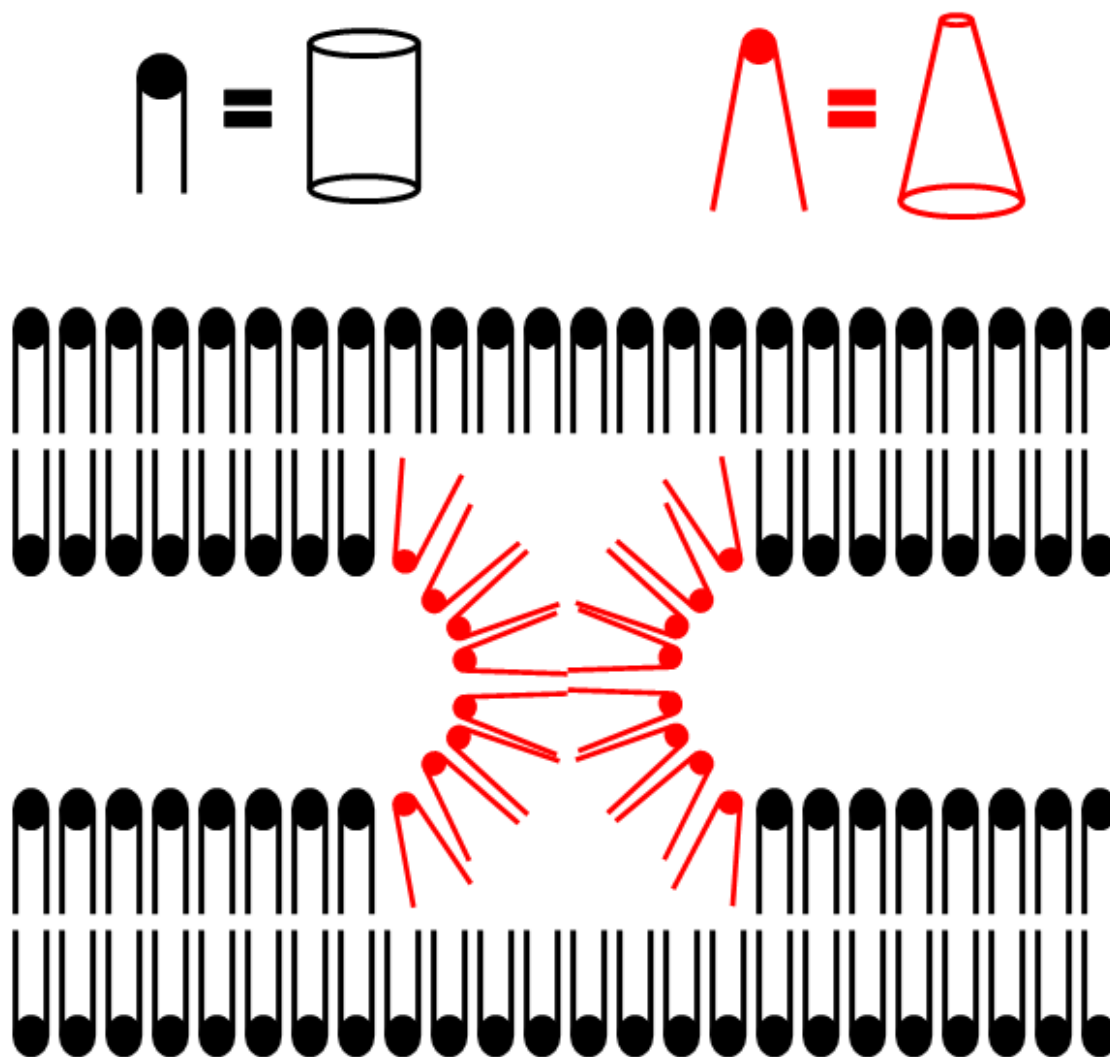


Figure 1-10. The “stalk” intermediate which is proposed to form during membrane fusion. Hexagonal II lipids, shown in red, concentrate in high curvature area to stabilize the structure.

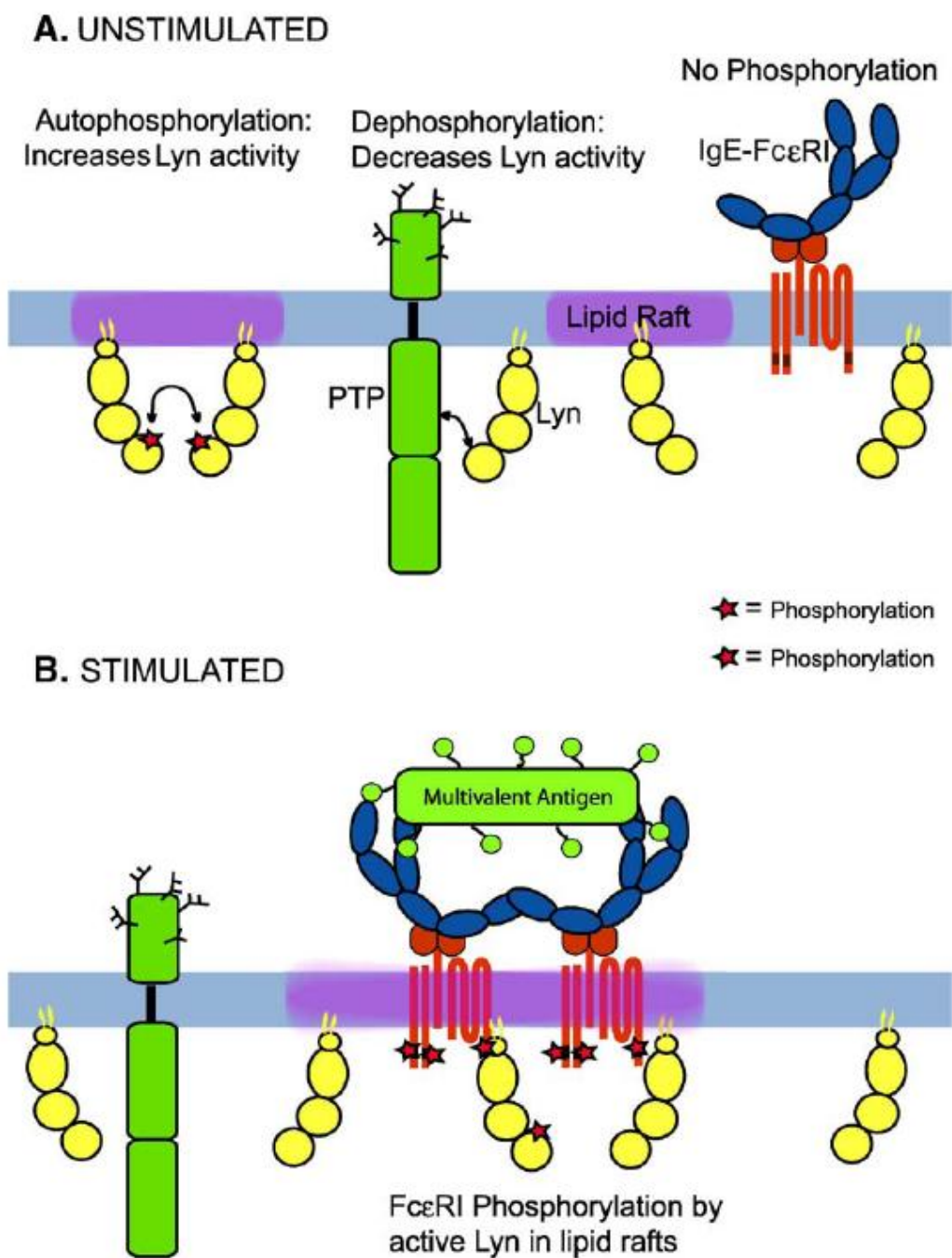


Figure 1-11. Graphic representation of protein segregation by lipid rafts that is relevant to IgE receptor signal initiation. (A) Distributions of relevant membrane components in unstimulated cells. (B) Distributions of relevant components following signal initiation by antigen-mediated IgE receptor crosslinking. This Figure is taken from Holowka, et. al.¹¹

spatial resolution. Due to the experimental constraints of SIMS, measurements must be made in a high vacuum environment. The rapid sublimation of water caused by the vacuum environment results in the destruction of cell membranes, and the redistribution membrane components. Thus, sample preparation is central to acquiring meaningful molecule-specific images with SIMS, especially when sub-micron lateral resolution is involved. The issue is to maintain the distribution of target molecules while attempting to introduce biological cells or tissue into the high vacuum environment of the mass spectrometer. Several groups have been exploring many different ways of dealing with cells and tissue for imaging mass spectrometry. The “gold standard” in the view of many is freeze-fracture of frozen hydrated cells because it preserves the cell membrane in its native hydrated state. With this approach, a thin aqueous layer containing a small number of cells is quenched in liquid ethane to form an amorphous ice structure at temperatures below $-120\text{ }^{\circ}\text{C}$.²⁷ Rapid cooling is essential to avoid crystallization, which can vault molecules many microns away from their original positions. The emergence of 3-dimensional imaging capabilities also suggests that sample preparation should not perturb the 3-dimensional morphology of the cell, a situation not generally possible during freeze-drying.

In some cases, molecular depth profiling and 3-dimensional imaging are feasible with submicron resolution.^{28,29} These properties open new avenues for sample preparation since the surface of some samples need not necessarily be presented to the ion beam in pristine condition.

1.4.1 Freeze-drying

The simplest strategy of preserving cells for analysis in vacuum is freeze-drying of cells cultured on a flat substrate such as a Si wafer. This procedure involves removing the substrate from the culture media, with no rinsing, followed by plunging the chip directly into liquid N_2 coolant. Once frozen, the substrate is transferred to a vacuum chamber for several hours at a

modest pressure of 10^{-6} torr where the water is removed by sublimation. The chamber remains at room temperature during this process, but the water sublimates before any melting occurs.

An example, using the *Tetrahymena* cell line, is illustrated in Figure 1-12. In this situation, the freeze-dried cells generally retain their two dimensional morphology, as seen in the brightfield optical image and the SEM images shown in Figure 1-12A and 1-12B, respectively. However, the total ion SIMS image, and the mass selected images at m/z 184 and m/z 28 are extremely weak in the location of the cells as seen in Figure 1-12C and 1-12D. It is clear from the optical and SEM image that residual material from the culture medium has deposited on and around the cells. Generating a mass spectrum from the pixels in the cell region gives a spectrum that is dominated by Na and PDMS. It is hypothesized that the residual culture media is blocking the emission of the key secondary ions, especially phosphatidylcholine headgroup at m/z 184, which should be of high intensity in the region of the cell. It is also possible that the presence of excess salts negatively impacts the ionization of biomolecules.³⁰

It is certainly possible to quickly water rinse the cells to rid the freeze-dried product of residual culture material. There is significant danger of altering the morphology of the cells, due to swelling induced by osmotic pressure, as illustrated in the example presented in Figure 1-13. In this instance, the optical image of the rinsed *Tetrahymena* cells shown in Figure 1-13A, suggests that they have lysed. The absence of residual material, however, allows membrane-specific ions such as m/z 184 to be present in much higher intensities as seen in Fig 13B. The m/z 184 signal also strongly localizes to the cell. Since the cells have experienced a great deal of trauma during the rinsing process, detailed biological studies would be rather suspect.

Even when the procedure is optimized by quickly plunge-freezing the rinsed *Tetrahymena* cells into liquid C_2H_6 , and slowly freeze-drying to minimize water-vapor wind phenomenon³¹, there are still often experimental artifacts that complicate interpretation. An

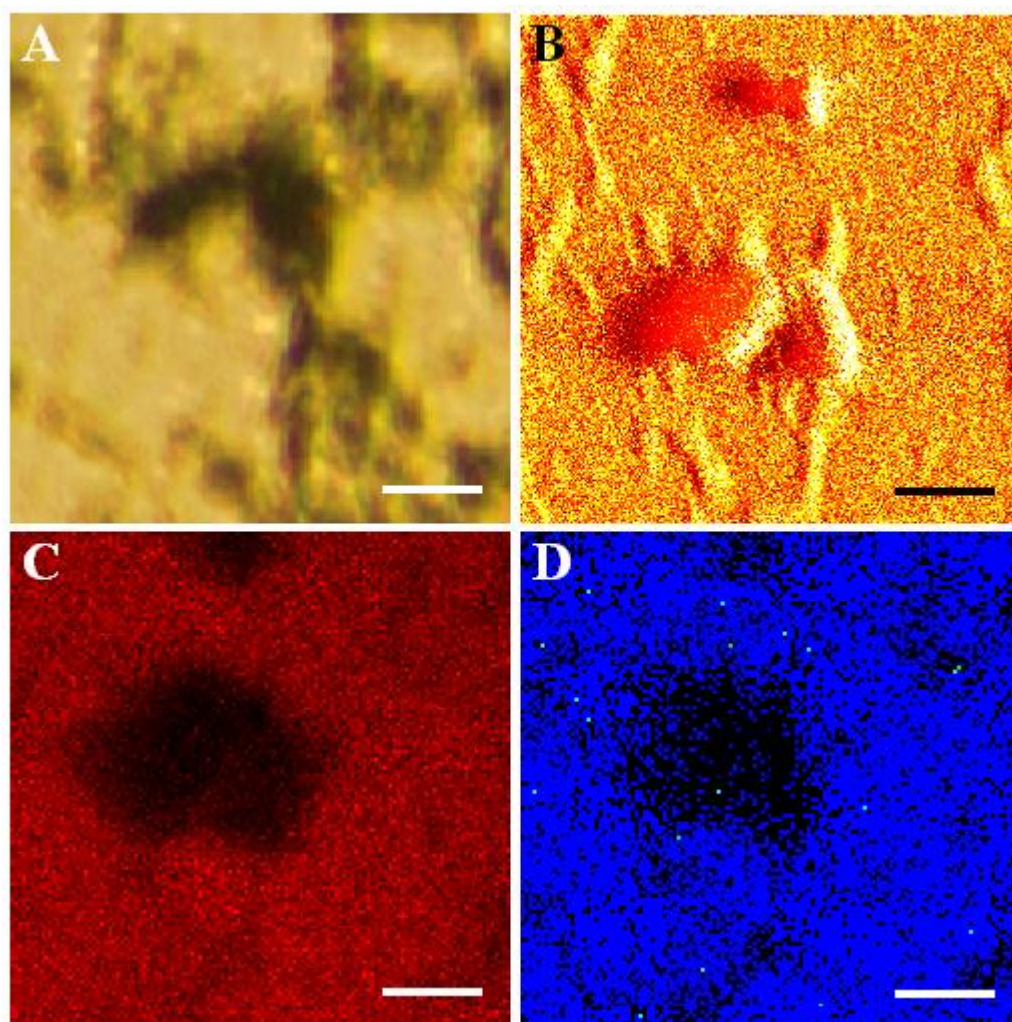


Figure 1-12. Freeze-dried *Tetrahymena* cells directly from culture medium. The images shown are (A) optical brightfield, (B) SEM, (C) total positive ions and (D) m/z 28 (blue) and m/z 184 (green – barely visible). Scale Bars represent 25 μm . All SIMS images were recorded using 15 keV In^+ ion bombardment.

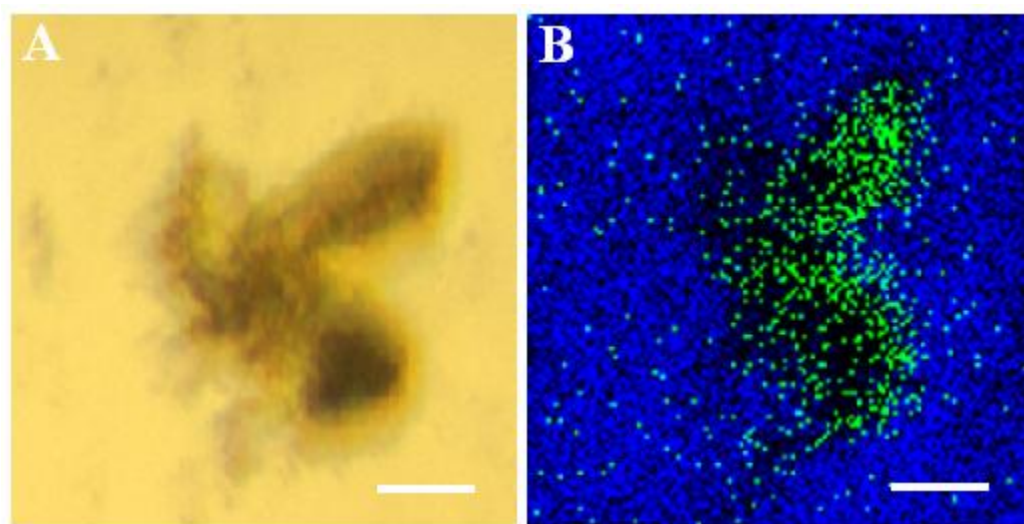


Figure 1-13. *Tetrahymena* cells, rinsed in 18 Mohm water, and then freeze dried. (A) optical brightfield. (B) m/z 28 (blue) and m/z 184 (green). Scale Bars represent 25 μm . The SIMS image was recorded using 15 keV In^+ ion bombardment.

example is shown in Figure 1-14, where the SEM image of the cells suggests that they are well-preserved. The SIMS images, however, clearly show that even though the m/z 184 diagnostic signal is nicely localized, the presence of m/z 69, a ubiquitous hydrocarbon ion which identifies hydrocarbon material that most likely originated in the cell, suggests leakage from cell into the surrounding areas.

Finally, it is interesting to examine the response of freeze-dried cells to cluster bombardment, even though the possibility of cell damage must still be considered. A comparison of the results of total ion imaging with several different projectiles is shown in Figure 1-15. Note that the amount of signal arising from the cell itself goes from nearly zero using the In^+ or Au^+ projectile, to values larger than seen from the Si substrate for Au_3^+ and C_{60}^+ bombardment. This type of effect has been reported previously for polymer beads on Si substrates.³² The effect arises due to the much higher relative sputtering yield enhancement observed for soft materials versus harder materials such as Si.

In summary, freeze-drying in its various forms often yields cells that appear to be well-preserved, but many artifacts both obvious and subtle can occur during the process. The emergence of cluster bombardment has opened new possibilities since greatly improved signal intensities are usually observed from the cell location.

1.4.2 Trehalose vitrification

To minimize cell collapse and cell damage, a stabilizing matrix that helps to keep things in their original location has been sought after. The disaccharide trehalose is known to preserve dehydrated biological tissue and cells.³³ Entire organisms, that produce trehalose, have been found to survive natural desiccation for years.³⁴ Hence, this material is an excellent candidate for use as a stabilizing matrix, and experiments have been performed where this step has been added

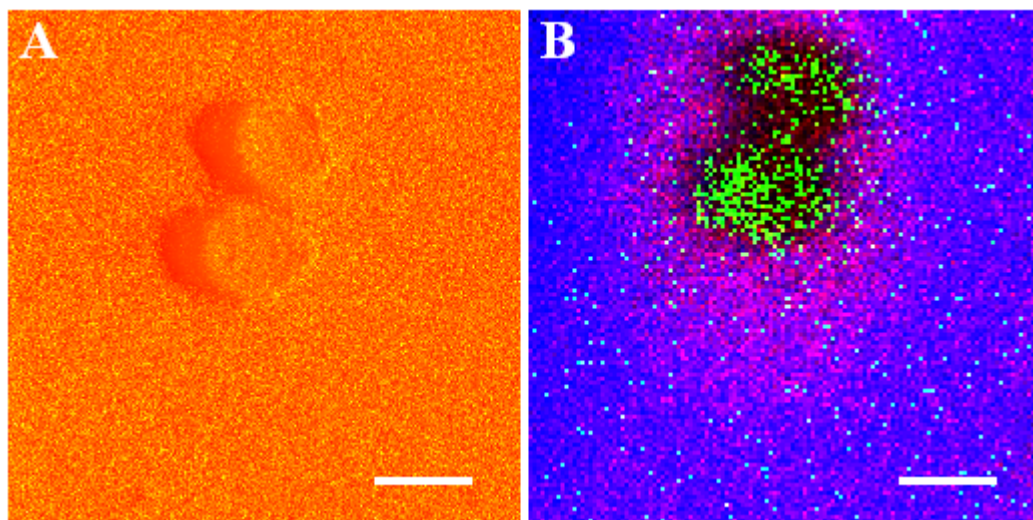


Figure 1-14. Freeze-dried *Tetrahymena* cells revealing hidden damage (A) SEM. (B) m/z 28 (blue), m/z 184 (green), and m/z 69 (red). Scale Bars represent 25 μm . The SIMS image was recorded using 15 keV In^+ ion bombardment.

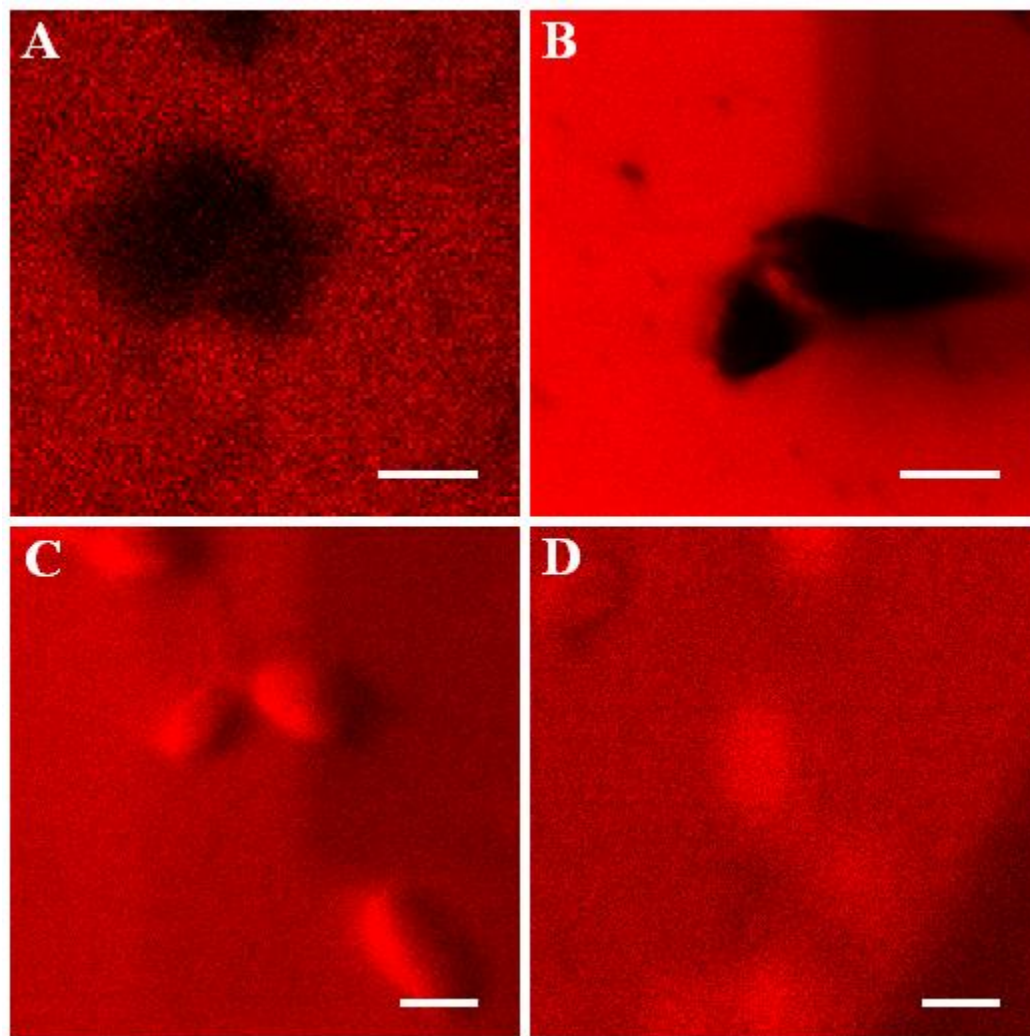


Figure 1-15. Total ion SIMS images of rinsed and freeze-dried *Tetrahymena* cells. The primary ion is (A) 15 keV In^+ , (B) 20 keV Au^+ , (C) 20 keV Au_3^+ and (D) 20 keV C_{60}^+ . Scale Bars represent 25 μm .

to the freeze-drying process.³³ The main advantage is that the 3-dimensional integrity of the cell membrane is preserved while maintaining the possibility of achieving submicron lateral resolution.

An example of glial cells prepared for SIMS imaging via trehalose vitrification is shown in Figure 1-16. The procedure is quite straightforward. Trehalose is added directly to the culture media. After several hours of incubation, the culture media is rinsed away with a PBS buffer solution containing 50-100 mM trehalose. Then, there is a final rinse in a 50-100 mM trehalose, 0.3% glycerol, water solution. Since disaccharides are natural cryo-protectants, fast-freezing is not necessary. The cells are thus frozen in liquid nitrogen, and dried in vacuum at 10^{-6} torr. In Figure 1-16A, the total ion SIMS image from 20 keV Au⁺ ion bombardment shows detailed morphological structure, with the cell nucleus bulge clearly visible. In Figure 1-16B, the m/z 184 ion is shown to be localized with the cell, cell processes and nuclear bulge in the membrane without any apparent artifacts. The preparation is also amenable to C₆₀⁺ ion bombardment. As shown in Figure 1-16C, the total ion image exhibits much less contrast than Au⁺ bombardment since the yields are approximately the same from the cell and the substrate. The chemical image shown in Figure 1-16D exhibits larger counts of m/z 184, albeit with somewhat poorer lateral resolution.

Practically then, trehalose offers a platform where cells can be analyzed at room temperature in their native morphology. The disaccharide matrix offers to minimize the financial and time investments incident to analysis of frozen samples. While amorphous ice provides the most native cellular preservation, frozen samples are particularly susceptible to condensation *in vacuo*, which can hinder ToF-SIMS analysis. A matrix which facilitates long term storage and analysis and 3-dimensional preservation, may be the model platform for time intensive-studies, such as depth profiling of biological cells.

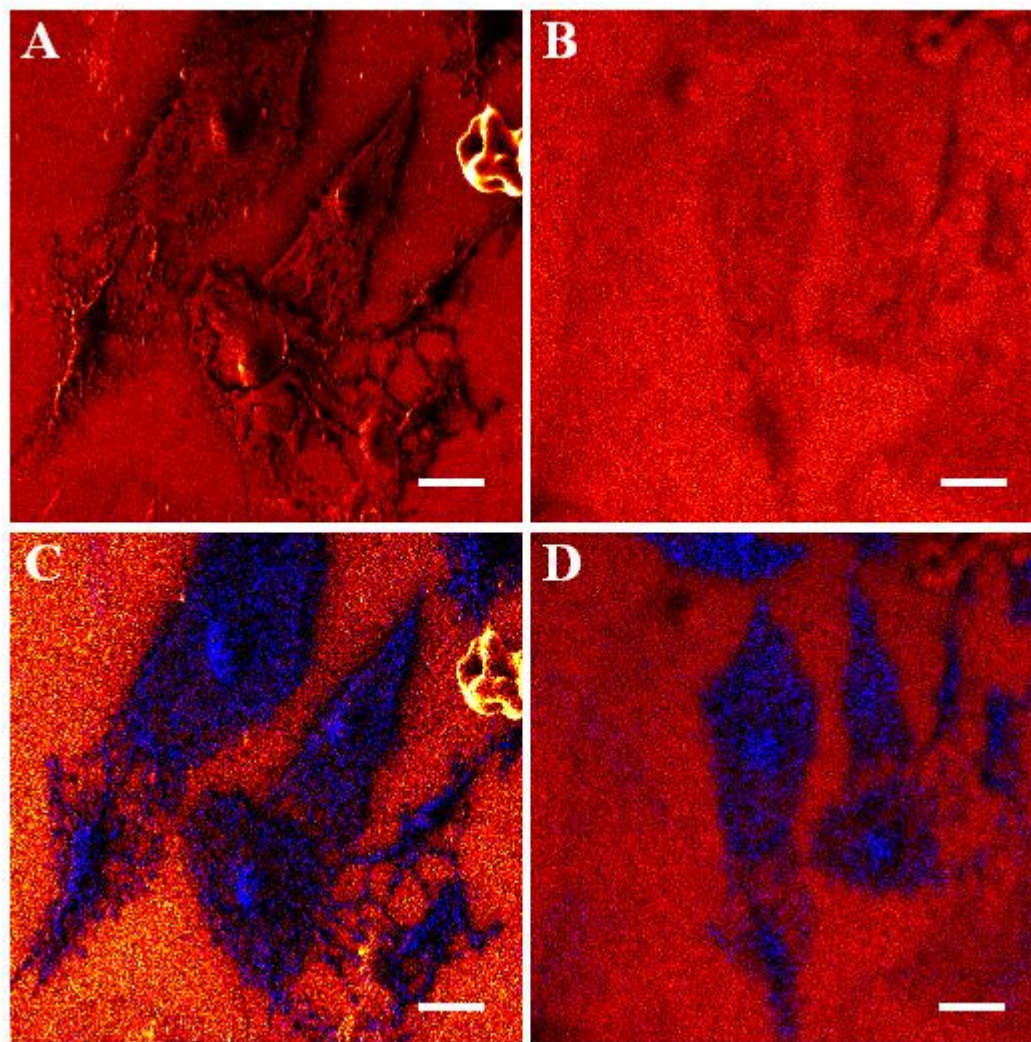


Figure 1-16. Mixed Glia – Oligodendrocytes and Astrocytes lyophilized in trehalose. From the total ion SIMS image acquired using Au^+ bombardment in (A), the morphology of the cell is seen to be preserved. The total ion SIMS image in (B) was acquired using C_{60}^+ bombardment. The molecule-specific images from Au^+ and C_{60}^+ bombardment are shown in (C) and (D), respectively. The scale bars represent 50 μm . Data taken by Shawn Parry.

1.4.3 Freeze-etching

Another strategy for maintaining the 3-dimensional morphology of cells is to prepare them in a frozen-hydrated state. We have explored several approaches to this challenging sample preparation method. The simplest procedure is to culture the cells directly on a Si substrate, wash the cell surface quickly, within a few seconds, with distilled water to remove the culture medium, and then plunge freeze the entire construct into liquid C_2H_6 . The plunge freezing minimizes ice crystallization which can vault molecules many microns away from their original location. This sample may then be stored under liquid nitrogen indefinitely. For SIMS imaging, the cold sample is removed from the liquid nitrogen and inserted directly into the cooled sample stage of the mass spectrometer. During this transfer, ice crystals inevitably deposit on the cell surface, preventing a meaningful analysis. However, in vacuum, we have found it is possible to slowly warm the sample at $5\text{ }^\circ\text{C}/\text{min}$ to a final temperature of $-80\text{ }^\circ\text{C}$. At this point, the water on top of the cell is slowly subliming without allowing crystallization. After about 1 hour, a time determined by monitoring the process with a video camera, the sample is re-cooled to less than $-170\text{ }^\circ\text{C}$ for imaging. Although a small amount of ice condenses on the sample surface during cooling, positive SIMS ion yields are found to be enhanced by about a factor of 2 due to the presence of this layer.³⁵

Overall, this approach is less complicated than *in situ* freeze-fracture, and provides results that are generally as reliable.

1.4.4 C_{60} -etching

The observation that C_{60} bombardment allows molecular depth profiling in many cases suggests that the preparation techniques discussed above may be modified and improved. The

basic idea is to culture cells in the laboratory environment and transfer them directly to the mass spectrometer at cryogenic temperatures. The C_{60} etching is then utilized to remove any residual contamination overlayer without insult to the underlying material.

For Figures 1-17A and 1-17B, respectively, a macrophage cell was cultured directly onto a Si wafer and flash-frozen as described above. After transfer to the mass spectrometer, the image observed is largely covered with water-ice as indicated by the blue color at m/z 18. After etching with a dose of $10^{13} C_{60}^+$ ions/cm², the m/z 184 ion is clearly revealed and is well-localized to the macrophage. These results suggest that it is no longer necessary to worry as much about contamination overlayers during the sample preparation process.

The C_{60} -etching method may also be useful for a number of freeze-dried samples. Using the hypothesis that the redistribution chemistry may be less violent within the tissue, C_{60}^+ etching has been utilized to remove the redistributed layer to uncover a less disturbed portion of the sample. To estimate the sputter depth, values for sputter yield and molecular density from previous experiments involving trehalose, were utilized. Therefore, the fluence corresponds to the removal of roughly 30-40 nm of material. The results suggest that the redistribution of cholesterol is largely a surface phenomenon, and may remain undisturbed in the bulk of the tissue. Thus, the use of cluster bombardment opens new ways to preserve chemical localization.

1.4.5 Freeze-fracture of frozen-hydrated cells

I believe that the safest way to preserve the 3-dimensional cell morphology and chemical arrangement to submicron precision is by freeze-fracture of frozen-hydrated cells directly within the confines of the mass spectrometer. There is considerable evidence that the presence of water as well as preserving the native bilayer structure, provides an optimal environment for ionization.^{36, 37} This strategy has already led to a number of successful applications including the

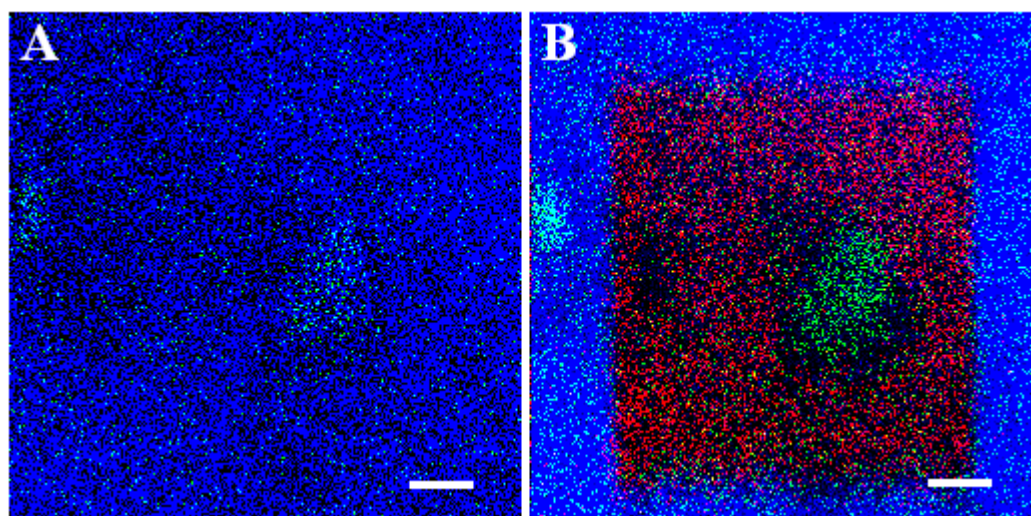


Figure 1-17. Application of C_{60}^+ bombardment to remove water layer. (A) Macrophage on Si with water overlayer. PC (m/z 184) is shown in green and (m/z 18) is shown in blue. (B) Smaller crater etched away showing cholesterol localization using a dose of 10^{13} ions/cm². Red is (m/z 28) to denote the Si substrate that has been uncovered. Scale bars are 25 μ m.

quantitative assay of cholesterol in macrophage cells³⁸ and the observation of lipid rearrangement in the highly curved membranes of mating *Tetrahymena* cells.¹⁴

However, there are still artifacts with this technique that need to be considered. An example is shown in Figure 1-18 where different freeze-fracture situations result either in undesirable topography or an unacceptable levels of sample charging. Three situations are compared using the m/z 69 species to represent ubiquitous hydrocarbon, and the m/z 184 peak to indicate membrane composition. If the ice layer is too thick, as seen in Figure 1-18A and 1-18B, the samples charge very badly under atomic ion bombardment as indicated by very weak signals. Current efforts to neutralize this sample charging, using an electron flood gun, have been unsuccessful. If the ice layer is too thin, as seen in Figure 1-18C and 1-18D, the morphology of the cell creates shadowing effects which make quantitative interpretation very difficult. Moreover, these samples are subject to rapid warming during transfer which often is accompanied by chemical smearing as noted in Figure 1-18C. Only when the ice thickness is on the order of the same thickness of the cell, in this case about 10 μm , is a uniform distribution of m/z 69 observed across the cell, indicating the non-uniform distribution of m/z 184 has biological significance. This last situation provides the cleanest representation of the chemistry of cells that we have seen using any of the other sample preparation protocols.

Until now, this cell line has only been examined with 15 keV In^+ ion bombardment, due to instrumental constraints in the laboratory. Many investigators are anxious to utilize C_{60}^+ ion bombardment to image cells for comparison purposes. If what has been learned from the earlier discussions holds true for the freeze-fracture methodology, the use of C_{60}^+ should greatly reduce the charging problems associated with thicker ice films and should obviate the need for very thin ice layers.

In all, the best sample preparation method will be dependent on the information that is desired and the sample that is being analyzed. Each sample preparation approach has its

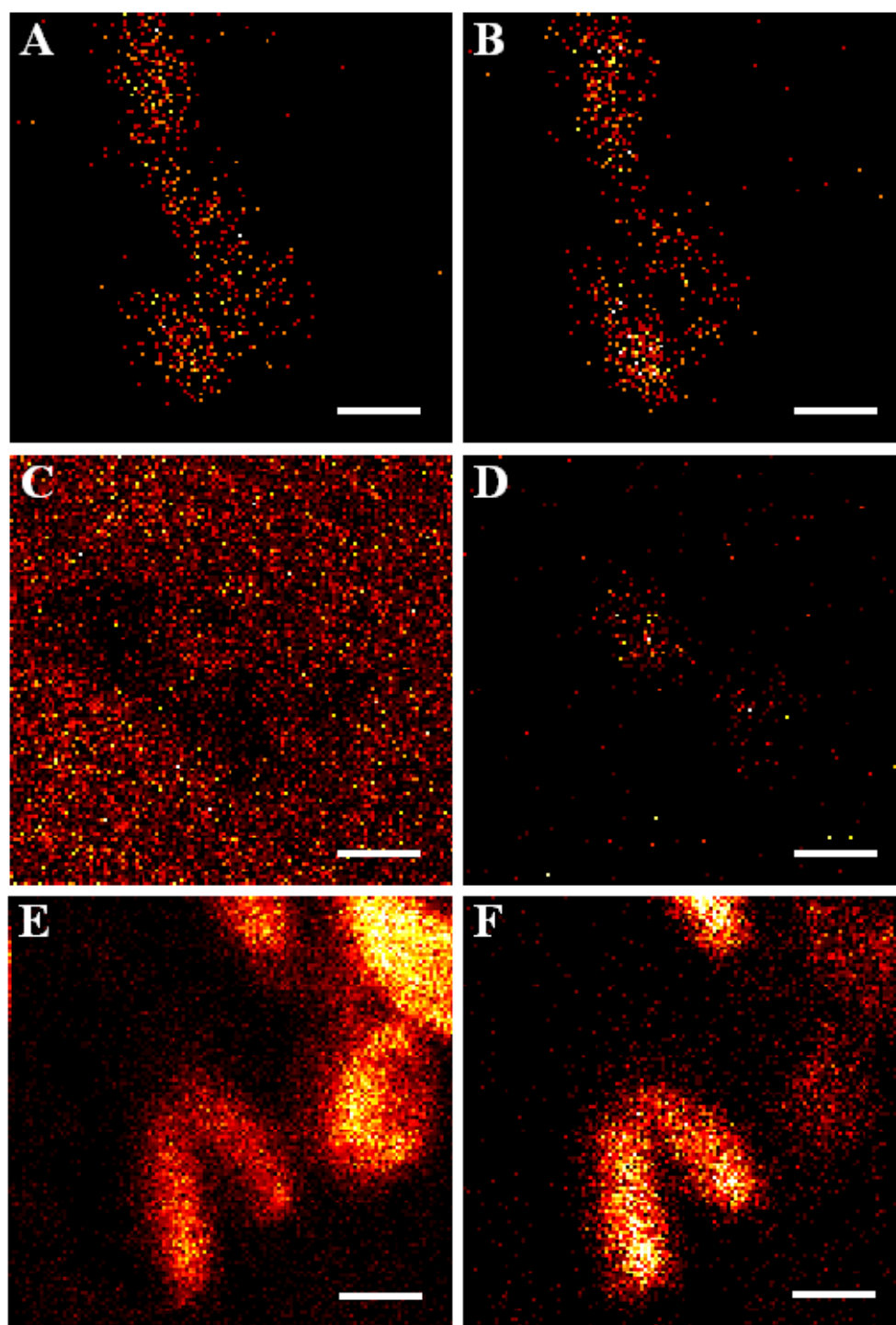


Figure 1-18. Chemical images of mating *Tetrahymena* cells, taken with differing ice thicknesses. (A,C,D) m/z 69, and (B,D,F) m/z 184. The sample (A,B) was fractured from a sandwich structure that produced a layer of ice thick enough to exhibit charging. The sample (C,D) contained a very thin ice layer that induced topographical artifacts. The sample in (E,F) has an ice thickness that produces results free of artifacts. Scale bars represent 25 μm . Data taken by Michael Kurczyk.

advantages and disadvantages. Freeze-drying and trehalose vitrification have the advantage of being simple, quick, and economical. In addition, they do not necessitate the modification of the instrument for handling cold samples. The disadvantage is that the quality of sample preservation is lower than with cryogenic methods. These methods are particularly useful with larger samples, and when sub-micrometer lateral resolution is not required. The cryogenic methods have the advantage of offering the best possible sample preservation and the ice matrix has been shown to enhance ionization. These two factors are crucial to measuring sub-cellular lipid distributions. However, these methods require expensive instrumentation and can be difficult to execute.

1.4.6 Summary

When studying biological samples, the implementation of ToF-SIMS presents unique challenges. Addressing these challenges to improve the quality of information obtained in SIMS analyses is the central theme of this work. The overarching goal is to apply this technique to study the spatial distribution of membrane lipids, and use this information to elucidate the role of these molecules in dynamic cellular events. Chapter 2 discusses the development of a freeze-etching protocol that aims to improve the reproducibility and decrease the difficulty of freeze fracture experiments, while maintaining the superior sample preservation of freeze-fracture.

Another challenge to imaging biological cells is the convoluted mass spectrum that is obtained when bombarding a complex sample with a primary ion beam. Spectral interpretation is further complicated by the low signal intensity of many biologically relevant ions. Recent improvements in mass spectrometry (MS) instrumentation have allowed a more detailed study of secondary ions. This technological advance and its application to traditional cholesterol imaging experiments, is discussed in Chapter 3.

Chapter 4 develops a statistical model that allows a more robust interpretation of the data obtained in imaging experiments. Further, it demonstrates the successful implementation of the concepts discussed in Chapters 2 and 3, to provide some valuable insights into the lipid distribution of the RBL-2H3 cell membrane.

In Chapter 5, a previous model system of the lab is revisited, mating *Tetrahymena thermophila*. In 2003, Ostrowski et. al. demonstrated the existence of a lipid domain, hypothesized to be curvature induced, in mating *Tetrahymena* cell pairs.¹⁴ To probe the underlying causes of these domains, a temporally resolved experiment was designed.

The development of C_{60}^+ cluster ion sources has greatly increased the potential scope of ToF-SIMS imaging experiments.⁵ Chapter 6 discusses the application of C_{60}^+ primary ions to improve sample quality. In addition, the potential for 3D biological analysis is demonstrated.

The thesis is concluded with a brief summary of the work and a discussion of initial experiments done with the hybrid quadrupole time-of-flight instrument.

1.5 References

- (1) Vickerman, J. C. *Surface analysis : the principal techniques*; John Wiley: Chichester [England] ; New York, 1997.
- (2) Vickerman, J. C.; Briggs, D. *ToF-SIMS: Surface Analysis by Mass Spectrometry*; IM Publications and SurfaceSpectra Ltd: Chichester, West Sussex, 2001.
- (3) Vickerman, J. C.; Briggs, D., Eds. *ToF-SIMS: Surface Analysis by Mass Spectrometry*; IM Publications and Surface Spectra Limited: West Sussex, 2001.
- (4) Carado, A.; Passarelli, M. K.; Kozole, J.; Wingate, J. E.; Winograd, N.; Loboda, A. V. *Anal. Chem.* **2008**, *80*, 7921-7929.
- (5) Winograd, N. *Anal. Chem.* **2005**, 143A-149A.
- (6) Yeagle, P. L. *The Membranes of Cells*, Second ed.; Academic Press, Inc.: New York, 1993.
- (7) Erwin, J. A. *Lipids and Biomembranes of Eukaryotic Microorganisms*; Academic Press: New York, 1973.
- (8) Tanford, C. *Science* **1978**, *200*, 1012-1018.
- (9) Singer, S. J.; Nicolson, G. L. *Science* **1972**, *175*, 720-731.
- (10) Edidin, M. *Annu. Rev. Biophys. Biomol. Struct.* **2003**, *32*, 257-283.

- (11) Holowka, D.; Gosse, J. A.; Hammond, A. T.; Han, X. M.; Sengupta, P.; Smith, N. L.; Wagenknecht-Wiesner, A.; Wu, M.; Young, R. M.; Baird, B. *Biochim. Biophys. Acta, Mol. Cell Res.* **2005**, *1746*, 252-259.
- (12) McMahon, H. T.; Gallop, J. L. *Nature* **2005**, *438*, 590-596.
- (13) Mukherjee, S.; Maxfield, F. R. *Annu. Rev. Cell Dev. Biol.* **2004**, *20*, 839-866.
- (14) Ostrowski, S. G.; Bell, C. T. V.; Winograd, N.; Ewing, A. G. *Science* **2004**, *305*, 71-73.
- (15) Simons, K.; Ehehalt, R. *J. Clin. Invest.* **2002**, *110*, 597-603.
- (16) Simons, K.; Ikonen, E. *Nature* **1997**, *387*, 569-572.
- (17) Simons, K.; Toomre, D. *Nat. Rev.* **2000**, *1*, 31-41.
- (18) Zimmerberg, J.; Chernomordik, L. V. *Adv. Drug Delivery Rev.* **1999**, *38*, 197-205.
- (19) Jahn, R. *Nat. Struct. Mol. Biol.* **2008**, *15*, 655-657.
- (20) Cans, A. S.; Wittenberg, N.; Karlsson, R.; Sombers, L.; Karlsson, M.; Orwar, O.; Ewing, A. *Proc. Natl. Acad. Sci. U. S. A.* **2003**, *100*, 400-404.
- (21) Baumgart, T.; Hess, S. T.; Webb, W. W. *Nature* **2003**, *425*, 821-824.
- (22) Basanez, G. *Cell. Mol. Life Sci.* **2002**, *59*, 1478-1490.
- (23) Kozlov, M. M.; Markin, V. S. *Biofizika* **1983**, *28*, 242-247.
- (24) Davey, A. M.; Heikal, A. A.; Sheets, E. D. 2007; Biophysical Society; 575A-575A.
- (25) Davey, A. M.; Krise, K. M.; Sheets, E. D.; Heikal, A. A. *J. Biol. Chem.* **2008**, *283*, 7117-7127.
- (26) Davey, A. M.; Walvick, R. P.; Liu, Y. X.; Heikal, A. A.; Sheets, E. D. *Biophys. J.* **2007**, *92*, 343-355.
- (27) Severs, N. J.; Shotton, D. *Rapid Freezing, Freeze Fracture, and Deep Etching*; Wiley-Liss: New York, 1995.
- (28) Wucher, A.; Cheng, J.; Winograd, N. *Analytical Chemistry* **2007**, *In Press*.
- (29) Fletcher, J. S.; Lockyer, N. P.; Vaidyanathan, S.; Vickerman, J. C. *Anal. Chem.* **2007**, *79*, 2199-2206.
- (30) Jones, E. A.; Lockyer, N. P.; Vickerman, J. C. *Anal. Chem.* **2008**, *80*, 2125-2132.
- (31) Cannon, D. M. J.; Pacholski, M. L.; Winograd, N.; Ewing, A. G. *J. Am. Chem. Soc.* **2000**, *122*, 603-610.
- (32) Xu, J.; Ostrowski, S.; Szakal, C.; Ewing, A. G.; Winograd, N. *Appl. Surf. Sci.* **2004**, *231-2*, 159-163.
- (33) Parry, S.; Winograd, N. *Anal. Chem.* **2005**, *77*, 7950-7957.
- (34) Crowe, J. H.; Crowe, L. M. *Nature Biotechnology* **2000**, *18*, 145-146.
- (35) Piehowski, P. D.; Kurczy, M. E.; Willingham, D.; Parry, S.; Heien, M. L.; Winograd, N.; Ewing, A. G. *Langmuir* **2008**, *24*, 7906-7911.
- (36) Roddy, T. P.; Jr., D. M. C.; Ostrowski, S. G.; Ewing, A. G.; Winograd, N. *Anal. Chem.* **2003**, *75*, 4087-4094.
- (37) Prinz, C.; Malm, J.; Hook, F.; Sjoval, P. *Langmuir* **2007**, *23*, 8035-8041.
- (38) Ostrowski, S. G.; Kurczy, M. E.; Roddy, T. P.; Winograd, N.; Ewing, A. G. *Anal. Chem.* **2007**, *79*, 3554-3560.

Chapter 2

Freeze-Etching and Vapor Matrix Deposition for ToF-SIMS Imaging of Single Cells

2.1 Introduction

The role of individual lipid components in membrane processes is a topic of considerable interest in cellular and molecular biology.¹⁻³ A variety of methods including atomic force microscopy (AFM),⁴ NMR,⁵ near-field scanning optical microscopy (NSOM),⁶ electron spin resonance (ESR),⁷ single particle tracking (SPT)⁸ and fluorescence microscopy, have been applied to the study of membrane lipid heterogeneity.⁹ Indeed, much of what is known about role of individual lipid components in membrane processes has been obtained with fluorescence techniques. Typically, synthetic fluorescent probes containing fatty acid-like chains are inserted into the membrane. By manipulating the structure of these chains, a preference for various membrane environments is imparted, although the chemical specificity is often restricted. In addition, these bulky fluorophores might perturb the environment and alter intrinsic domain formation events.⁴

Recently, imaging with time-of-flight secondary ion mass spectrometry (ToF-SIMS) has been shown to be a powerful analytical tool for mapping the distribution of biologically relevant small molecules (<1000 Da) on a surface.¹⁰ This method combines submicron spatial resolution, high chemical specificity and surface sensitivity making it a promising tool for the study of lipids in cellular membranes. Briefly, a pulsed beam of primary ions is directed at the analysis surface, causing the sputtering of ions and molecules. The ions are extracted into a ToF mass analyzer generating a mass spectrum. To obtain an image, the primary beam is raster-scanned across the surface, recording a mass spectrum for each pixel. Masses of interest are then selected from the

spectrum and their intensities mapped across the imaging area. When combined with cryogenic sample preparation techniques, ToF-SIMS allows the detailed study of membrane lipids during dynamic processes such as membrane fusion.¹¹⁻¹³

The quality of the information obtained with SIMS is dependent upon conservation of morphological and chemical integrity of samples.¹⁴ However, utilization of ToF-SIMS requires that the biological samples be analyzed in a high vacuum environment. Towards this end many approaches have been used, including freeze-fracture,¹³ freeze-drying,¹⁵⁻¹⁸ vitrification in trehalose,¹⁹ and imprinting on metal foil.²⁰ A freeze-fracture protocol based on methods used in electron microscopy has been developed for ToF-SIMS.¹³ In this method, freezing of the sample is performed in liquid ethane to quench the sample, capture dynamic membrane processes and protect the sample from water crystallization damage. While this technique has the advantage of preserving membranes in their hydrated state it also has disadvantages. When a fracture is performed, very precise control over the vacuum environment is necessary to maintain a reproducible surface amenable to SIMS analysis. Fracture-induced damage of cells can also occur which may complicate interpretation and degrade the quality of information obtained from SIMS. Lastly, the fracture plane is difficult to reproduce, making many samples unusable and making comparison of cells in different populations difficult.

Another challenge facing SIMS imaging is low signal intensity from many biologically interesting molecules. Ionization efficiency measurements of membrane lipids demonstrate that less than 0.01% of molecules desorbed by the primary ion beam impact are ionized.²¹ Improving the ionization efficiency of the target molecules could greatly improve the SIMS signal. Significant increases in sputter yield have been achieved using cluster ion sources for sample bombardment and have attracted the attention of many in the SIMS community.²²⁻²⁴ Many groups have been pursuing ways of improving signal through creative sample preparations,

coating samples with thin metal films (metA-SIMS),²⁵ deposition of MALDI-type matrices (ME-SIMS),^{15, 26-28} and the addition of metal nanoparticles.^{29, 30}

The overall goal of this research is to measure nanometer-scale distributions of lipids in the cell membrane. Thus, it is crucial that the spatial distribution of these molecules is maintained during sample preparation. To obtain this level of preservation I have utilized cryogenic sample preparation methodology. In this chapter, a sample preparation technique is described for SIMS that not only improves the reproducibility of bio-vacuum interfaces, but also increases ionization efficiency. Implementation of this protocol produces cells with similar surface environments which greatly reduces the variation between cell images. The approach is illustrated using oligodendrocytes and macrophages, and the key attributes of the sample treatment are examined using various lipid model systems. With this method, adventitious sources of surface water-ice, which tend to block the emission of biomolecules, are removed by low-temperature sublimation. Next, a controlled amount of amorphous ice is re-deposited back onto the sample surface. This step yields significant signal enhancement when compared to freeze-dried sample preparations and also produces a uniform surface which does not have spatial resolution limited by matrix crystallization.³¹

2.2 Experimental Section

2.2.1 Cell culture

Oligodendrocytes were harvested from 1-day-old Sprague-Dawley rat pups and separated from cerebral tissue as previously described.³² The cells were cultured on 5 mm x 5 mm silicon shards (Ted Pella, Redding, CA) that were coated with 0.2 mg/mL poly(L-lysine) (VWR, West

Chester, PA) and 0.1 mg/mL collagen (Sigma-Aldrich, St. Louis, MO). Cells were incubated until maturation was visible under a microscope.

J774 macrophage cells were cultured in sterile, polystyrene cell culture flasks. When confluent, cells were treated with 25 $\mu\text{g}/\text{mL}$ of DiI (Molecular Probes, Eugene OR) in serum-free media (Invitrogen, Carlsbad, CA) for one hour. Following this treatment, cells were rinsed with media before being dislodged from the culture dish by gentle tapping. The suspension of cells was added to a new flask containing sterile 5 mm x 5 mm silicon shards.

2.2.2 Cell preparation for imaging

Shards containing maturing oligodendrocytes or macrophages were rinsed for 5 s in 18 M Ω water to remove contamination from excess media. To prevent cell rupture, they were quickly frozen in liquid ethane and stored under liquid nitrogen (LN₂). The samples were introduced to the UHV environment at LN₂ temperatures. Details of this process have been described elsewhere.¹³ Once under vacuum, the sample was warmed 5 °C/ min to -80 °C to remove the water while minimizing crystallization and redistribution of molecules by efflux of water from the surface. This process was monitored using a video camera mounted on a brightfield microscope, to ensure that microscale signs of crystallization did not occur. When the water was removed, the sample was quickly returned to liquid nitrogen temperatures. During the cooling process, some residual water in the vacuum environment was re-deposited on the sample producing a uniform layer of water on top of the cells.

2.2.3 Preparation of patterned cholesterol films

Physical vapor deposition (PVD) films were prepared by subliming cholesterol contained in a crucible by resistive heating of a tungsten filament followed by deposition onto a LN₂-cooled sample stage. The film thickness was monitored using a quartz crystal microbalance (QCM), and subsequently characterized using AFM. AFM images were collected using a Nanopics 2100 (KLA Tencor, San Jose, CA) by scanning a 200 μm FOV in contact mode.

2.2.4 Preparation of lipid films

Lipids were dissolved in 9:1 CHCl₃/MeOH solution at concentration of 1 mg/mL. Films were prepared by spin-coating 50 μL aliquots of lipid solution onto 5mm² silicon shards at a spin rate of 3000 rpm for 60 s. Dipalmitoylphosphatidylcholine and dilauroylphosphatidylethanolamine were obtained from Avanti Polar Lipids (Alabaster, AL) and cholesterol was obtained from Sigma Aldrich (St. Louis, MO). All lipids were used without further purification. Each lipid spectrum was taken from a sampling area of 132 x 102 μm using 5 x 10⁵ primary ion pulses. For enhancement measurements, the integrated peak area for the mass of interest was divided by the integrated peak area for the internal standard fragment (m/z 69), yielding a relative intensity.

2.2.5 Mass spectrometry

Imaging data using In⁺ primary ions was acquired using a Kratos Prism ToF-SIMS spectrometer (Manchester, U.K.) equipped with an In⁺ liquid metal ion source (FEI, Beaverton, OR). The pulsed primary ion source was operated at an anode voltage of 15kV angled at 45° to the sample. The beam was focused to approximately 200 nm in diameter, and delivered 1 nA of

DC current in 50 ns pulses. The sample was mounted onto a LN₂-cooled analysis stage (Kore Tech. Ltd, Cambridge, U.K.) biased at +2.5 kV, 2.5 inches from a cold trap also cooled with LN₂. An extraction lens, biased at -4.7 kV, collected the secondary ions which then traveled along a 4.5-m flight path and were detected at a microchannel plate (MCP) detector (Galileo Co., Sturbridge, MA).

Imaging data using C₆₀⁺ primary ions was acquired using a BioToF ToF-SIMS spectrometer, described in detail elsewhere.³³ The spectrometer was equipped with a 40 KeV C₆₀⁺ primary ion source³⁴⁻³⁶ (Ionoptika Ltd., Southampton, U.K.). The source was operated with a 300 μm diameter beam defining aperture, yielding approximately 20 pA of DC current.

Mass spectrometry images were acquired by raster-scanning the primary ion beam across the sample region and collecting a mass spectrum for each pixel. Using in-house imaging software, visual C++, molecule-specific images were created by selecting a mass peak of interest from the total ion mass spectrum and plotting the intensity of this mass at each pixel in the image. The intensity of each peak could then be displayed in false color and multiple images were overlaid. Signal intensities can be relatively compared in mass specific images using the line scan function built into the software. A line scan is a plot of the summed pixel intensities for a given chemical map as a function of the lateral distance of the line.

The instrument was also equipped with a channeltron detector (Burle, Lancaster, PA) positioned approximately 0.5 cm from the sample which was used to generate scanning ion micrographs (SIM). Scanning ion images were obtained by using the channeltron to measure the current of charged species and electrons emitted from the sample during direct current ion bombardment.

1.3 Results and Discussion

2.3.1 Single cell imaging

Analyzing the native morphology and molecular distributions is crucial to determining the biological role of individual molecules. Several cryogenic methods have been developed to achieve this difficult end.^{14,37} In the method presented here, the samples are plunge-frozen in ethane to eliminate sample damage due to water crystallization, then stored under LN₂ until analysis. A sample preparation and transfer chamber designed in-house¹³ is utilized to fracture the sample sandwich and move the sample to the analysis stage without significant warming. With careful control of the temperature and pressure during this process, a clean fracture surface can be generated. The limitations of this approach are that control over the conditions can be difficult to maintain through the transfer process, and that the plane of fracture is unpredictable. This can result in fractures through the center of a cell or through pure ice leaving the cell damaged or completely buried.

Previous attempts to remove excess surface water through sublimation have been unsuccessful. Warming of freeze-fractured liposomes results in images with lipid spread homogeneously across the surface.¹³ It appears that large water sublimation fluxes can redistribute molecules across surfaces. I have found here that significant amounts of water can be removed from the surface without redistribution of lipids, by ensuring that the sample temperature does not exceed -80 °C before being returned to LN₂ temperature. Images of cells that have been prepared in this fashion are shown in Figure 2-1.

A mature oligodendrocyte in culture, exhibiting the characteristic, delicate cellular processes, is shown in Figure 2-1A. A brightfield image of a similar oligodendrocyte in

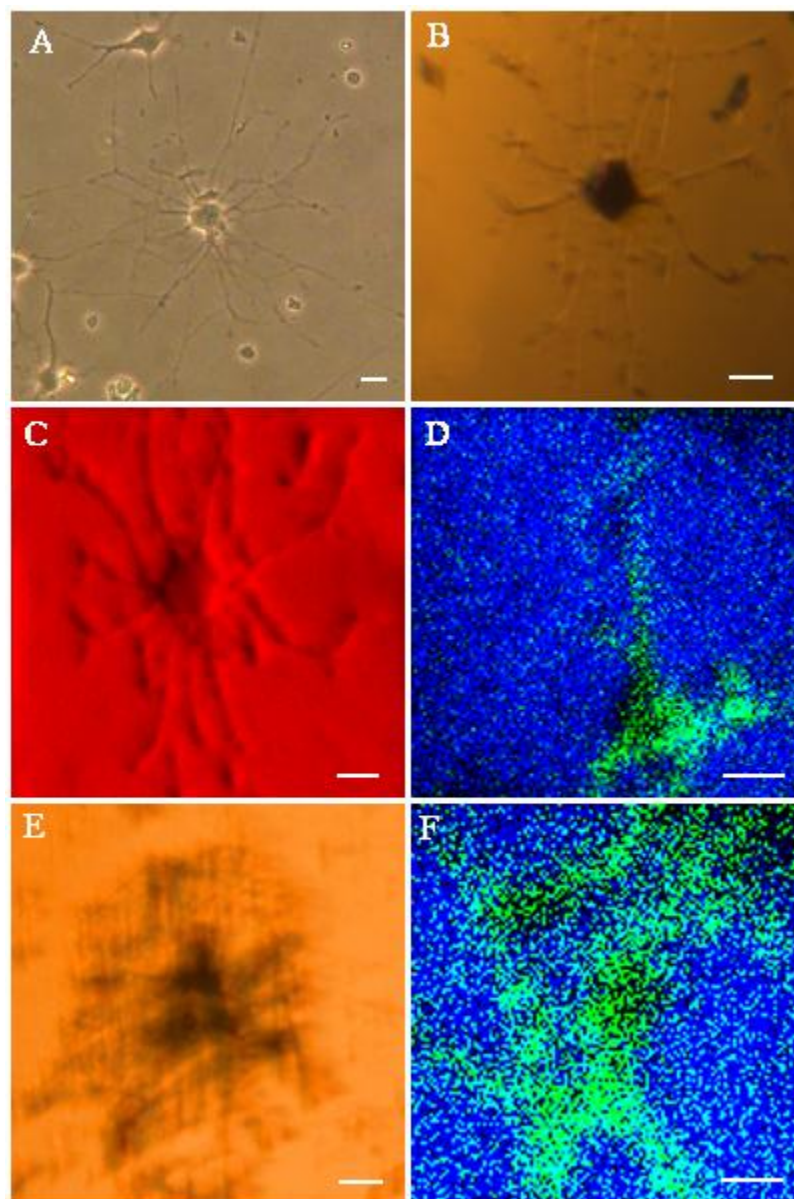


Figure 2-1. (A) Brightfield image of rat oligodendrocyte in culture. (B) Brightfield image of an oligodendrocyte cultured and silicon and cryogenically preserved using the described sample preparation method. (C) SIM image of rat oligodendrocyte. (D) SIMS image of a preserved oligodendrocyte, m/z 184(PC) green, m/z 28(Si) blue, intensity scale 0-4. (E) Brightfield image of oligodendrocyte that has been warmed to allow crystallization. (F) SIMS image of a corresponding area shown in (E), m/z 184(PC) green, m/z 28(Si) blue, intensity scale 0-2. Images were obtained using an In^+ primary ion beam, all scale bars are 20 μm .

vacuum after undergoing the freeze etching process is shown in Figure 2-1B. The SIM image shown in Figure 2-1C of the same cell shown in 2-1B, demonstrates that the cell maintains its morphology. A SIMS image overlay, where the green pixels represent m/z 184 PC and blue represents m/z 28 from the Si substrate, is shown in Figure 2-1D. From this image it is clear that there is not a measurable redistribution of lipid molecules from the cell to the adjacent surface, as previously seen when warming samples^{13, 38}.

To demonstrate the damage that occurs when warming is not controlled, Figure 2-1E and 1F show a cell that has been damaged by the warming process. The brightfield image in 2.1E shows that the delicate processes of the cell have been destroyed. In addition, the SIMS overlay shown in 1F demonstrates that there is significant smearing of the PC signal that occurs. In fact, the resulting image in these cases rarely resembles what is observed in the microscope.

2.3.2 Deposition of water

To test the effect of water re-deposition on the sample, a simple model system consisting of a patterned thin film of cholesterol was used, and this was characterized by SIMS and AFM. The film was created using physical vapor deposition of cholesterol onto a Si substrate with a finder grid in the center. After the deposition, the finder grid was removed leaving a relief pattern on the Si. SIMS images of the resulting film, before (A and B) and after (C and D) the deposition process, are shown in Figure 2-2.

Images 2-2A and 2-2C show all of the ions collected from the surface on the same thermal intensity scale. Deposition of water was confirmed by monitoring the increase of m/z 18, representing $[\text{H}_2\text{O}]^+$, using SIMS (data not shown). When qualitatively comparing images 2-2A and 2-2C, it is evident that more ions are collected from the cholesterol islands after deposition. The inverse is true for the signal from the Si substrate. Images 2-2B and 2-2D are

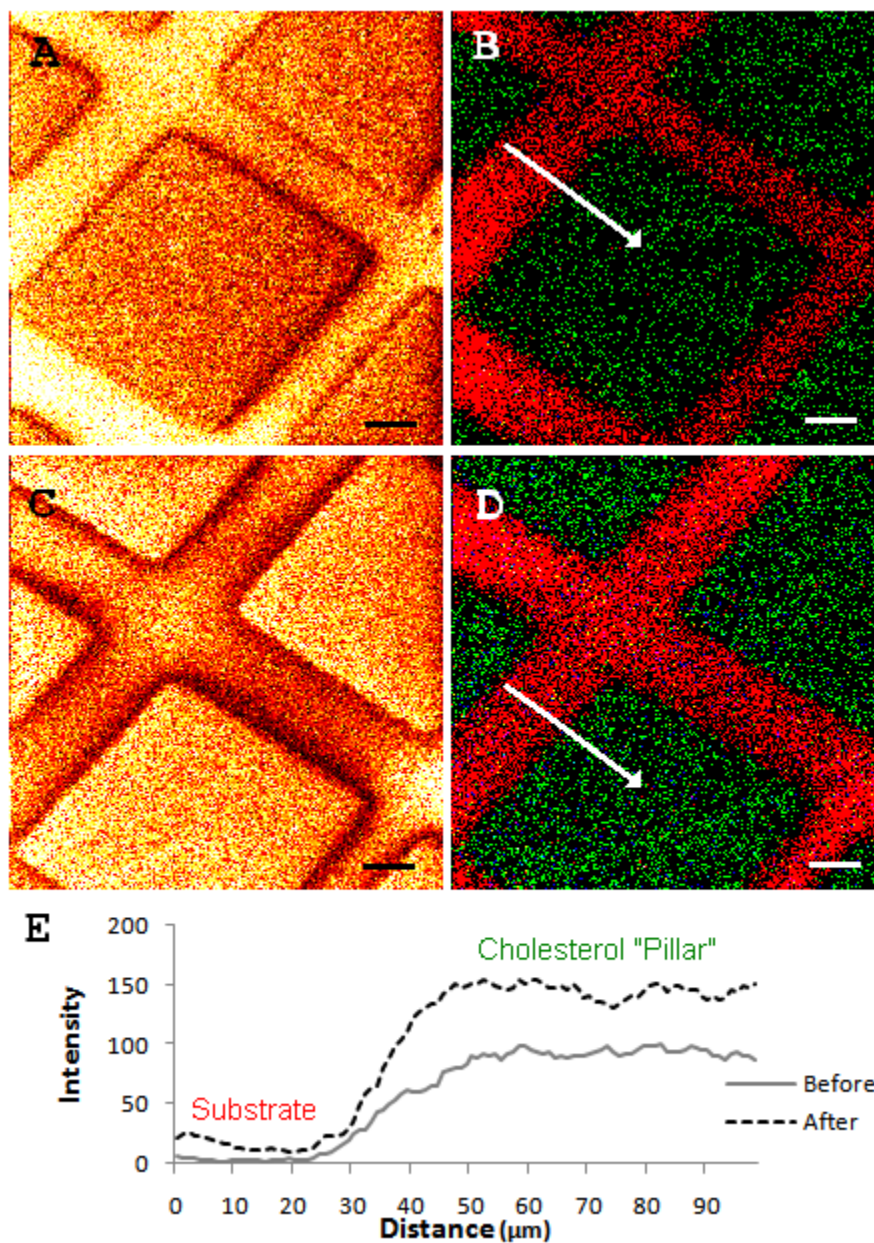


Figure 2-2. (A) Total ion image of a patterned cholesterol film prior to deposition. (B) SIMS image overlay from (A) m/z 369 (Cholesterol) green, m/z 28 (Si). (C) Total ion image of patterned cholesterol film after water deposition. (D) SIMS image overlay from (C) m/z 369 (Cholesterol) green, m/z 28 (Si). Thermal intensity scale from black to white, 0-20 counts. Scale bars represent 25 μm. (E) Line scans displaying intensity of cholesterol ion as a function of distance across image “Before” and “After” water deposition as indicated by the lines in part B and D.

SIMS overlay images that represent cholesterol (Green) and Si (Red). The ionization effect on cholesterol is demonstrated through the use of a line scan shown in Figure 2-2E. A more thorough investigation of these ionization effects can be found later. The data in image 2-2D shows that there is no measurable change in the distribution of cholesterol as a result of water deposition. Due to the limitations of spot size of the In^+ source, measurements of lateral resolution from this analysis have been limited to approximately 1 μm , and no change in resolution was measured after deposition. To more fully demonstrate the preservation of film features, the samples were also analyzed using AFM.

Representative AFM images are shown in Figure 2-3. Images 2-3A and 2-3B show the same feature on the film before and after being placed in vacuum and having water deposited and then removed, respectively. Image 2-3B shows that there are no changes resulting from the deposition and removal process. The representative line scans shown correspond to the same feature on the film, and measurements of feature size confirm that there is no change.

There is no evidence of damage from deposition or removal, which implies that a matrix can be vapor-deposited without imposing a limit on spatial resolution. This result has important implications for imaging of single cells with SIMS, as it increases signal without compromising sample preservation. Various compounds, other than water, might be deposited in vacuum to yield greater ionization increases.

2.3.3 Signal enhancement

Water sublimed from the sample is not completely removed from the vacuum environment. Thus the subsequent return of the sample to liquid nitrogen temperature results in the deposition of some water on the sample. Re-deposition can be monitored from the intensity

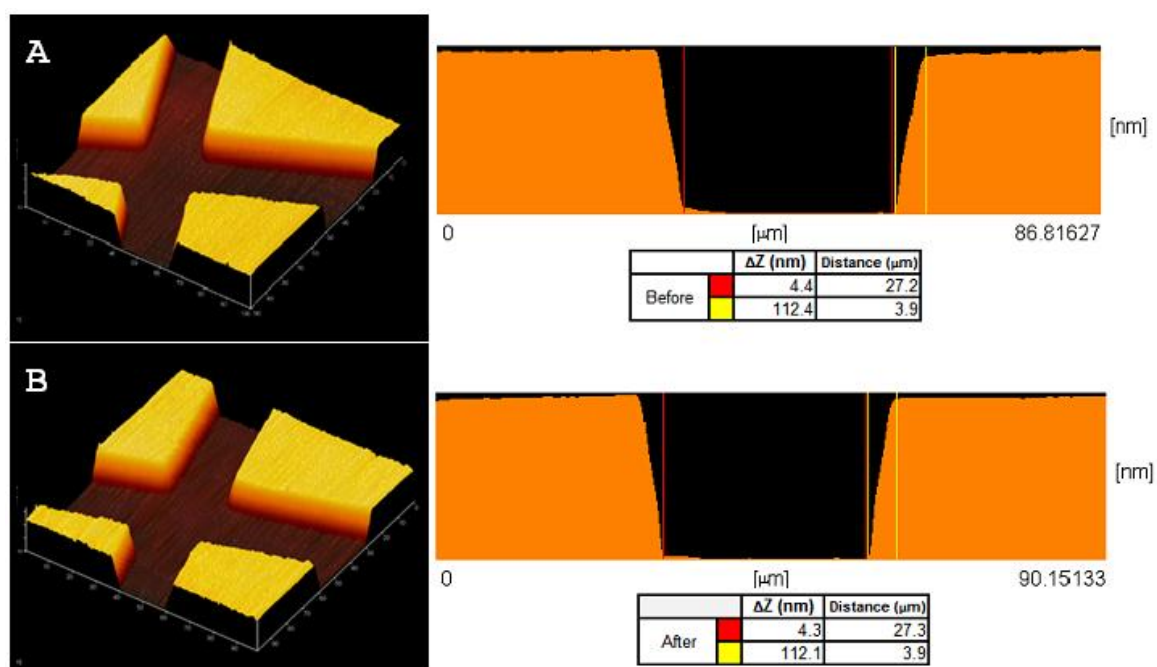


Figure 2-3. (A) 3D-AFM image of patterned cholesterol film before water deposition, FOV $100 \mu\text{m}^2$, to the right is an average cross-section of the film (B) 3D-AFM image of patterned cholesterol film after water deposition and removal, FOV $100 \mu\text{m}^2$, to the right is an average cross-section of the same region as above.

Table 2-1. Normalized intensity of characteristic lipid fragments before (Control), and after low temperature water matrix deposition (Cold Film).

Fragment (m/z)⁺	Control Intensity (± SD)	Cold Film Intensity (± SD)	% Enhancement (± SD)
PC fragments			
184	0.67 ± 0.045	1.0 ± 0.11	51 ± 6
86	0.99 ± 0.039	1.9 ± 0.039	94 ± 4
224	0.047 ± 0.0043	0.11 ± 0.021	141 ± 28
166	0.13 ± 0.0068	0.24 ± 0.034	84 ± 13
CH Fragments			
369	0.18 ± 0.043	0.28 ± 0.031	56 ± 15
385	0.11 ± 0.012	0.21 ± 0.025	95 ± 15
PE Fragments			
124	0.072 ± 0.003	0.114 ± 0.006	59 ± 4
142	0.087 ± 0.0041	0.121 ± 0.0085	40 ± 3
Tail Fragment			
575	0.044 ± 0.0031	0.08 ± 0.0054	82 ± 8
(M+H)⁺			
735	0 ± 0	0.00179 ± 0.00077	

of the mass peak at m/z 18, in the mass spectrum of freeze-etched samples. Of great potential interest, water deposition was found to enhance the signal from several lipid molecules.

To quantify the enhancement observed, films of the lipids phosphatidylcholine (PC), phosphatidylethanolamine (PE), and cholesterol (CH) were analyzed with SIMS using an In^+ primary ion beam. The intensity of characteristic fragments^{39, 40} was measured by integrating the peak areas and normalizing them to the intensity of m/z 69 (C_5H_9^+). The (C_5H_9^+) fragment has been used as an internal standard to account for small variations in secondary ion signal that can occur during SIMS analysis as a result of primary beam current fluctuation, sample topography, and secondary ion collection efficiency.^{16, 41} With this analysis, variability of less than 10% is achieved using many different samples, Table 2-1.

Signal enhancement is observed for all characteristic fragments measured in the analysis, however, as is seen in previous studies^{25, 30, 42, 43}, the amount of enhancement varied for each fragment analyzed. Some signals, such as the m/z 184, resulting from the PC headgroup, have already been extensively mapped in previous SIMS imaging experiments.^{15, 16, 20, 37} Other ions have not produced sufficient signal intensity for the production of detailed images. Of particular interest to lipid mapping experiments, are the signal enhancements observed for characteristic lipid tail fragments, lipid molecular ion, and the m/z 224 fragment (PC headgroup plus glycerol). Significant increases in tailgroup signal make it possible to image unique distributions of acyl chains in lipid models such as liposomes or supported bilayers. Also significant, is the appearance of the molecular ion peak for Dipalmitoylphosphatidylcholine (DPPC). Ion bombardment using In^+ is known to induce a large amount of fragmentation upon impact, and the DPPC molecular ion is not observed in dry lipid preparations. The cold samples of DPPC exhibit considerable signal corresponding to $[\text{M}+\text{H}]^+$. Enhancement of the 224 fragment is also of significance to biological imaging experiments because reference spectra⁴⁴

demonstrate that this fragment can be used to differentiate between PC derived from phospholipid species and PC derived from sphingomyelin, not possible in previous imaging studies.

2.3.4 Role of water deposition in signal enhancement

It has been previously established that PC ionization can proceed by intermolecular proton abstraction and that the presence of water in frozen hydrated samples increases ionization efficiency.⁴⁵ In an attempt to differentiate the effect of the presence of water from the effect of cooling the sample, a cold trap was placed in the analysis chamber, to remove water from the chamber before the film was cooled on the stage. When the trap is employed, the signal enhancement observed from cooling is significantly decreased by 20 ± 8 percent; and the change in ionization efficiency was not significant (Student's t-test, $p = 0.145$). When the trap is not used, the enhancement observed is significant, 51 ± 6 percent, Student's t-test, $p = 0.002$). This is strong evidence that small amounts of water deposition cause the increase in ionization efficiency. Results are summarized in Figure 2-4.

2.3.5 Surface stability during analysis

To demonstrate the stability of the surface that results from the low temperature deposition of a water matrix, multiple regions were analyzed across the surface of a DPPC film over the course of 3 hours. The intensity of m/z 18, standardized to total secondary ion intensity, was used to monitor the deposition of water (data not shown). After an initial 20 min of cooling, the enhancement effect is saturated, Figure 2-5. Assuming a sticking coefficient of unity, 20 min corresponds to 1.6×10^{13} water molecules/cm². Following the initial increase, the signal intensity of characteristic DPPC fragments varied by no more than 10%.

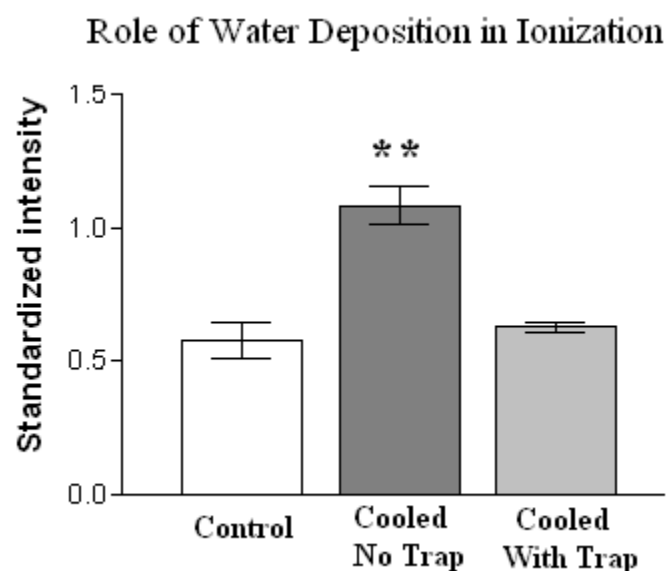


Figure 2-4. Histogram summarizing results of deposition experiments utilizing a cold finger to control the deposition of water. Control intensity represents the signal intensity of m/z 184 (PC Headgroup) on a dry lipid film. “Cooled with Trap” intensity represents signal intensity of m/z 184 when a cold finger was cooled in the sample chamber prior to sample cooling, thus limiting the deposition of water. “Cooled No Trap” intensity represents the signal intensity of m/z 184 (PC Headgroup) after cooling the stage without employment of a cold finger.

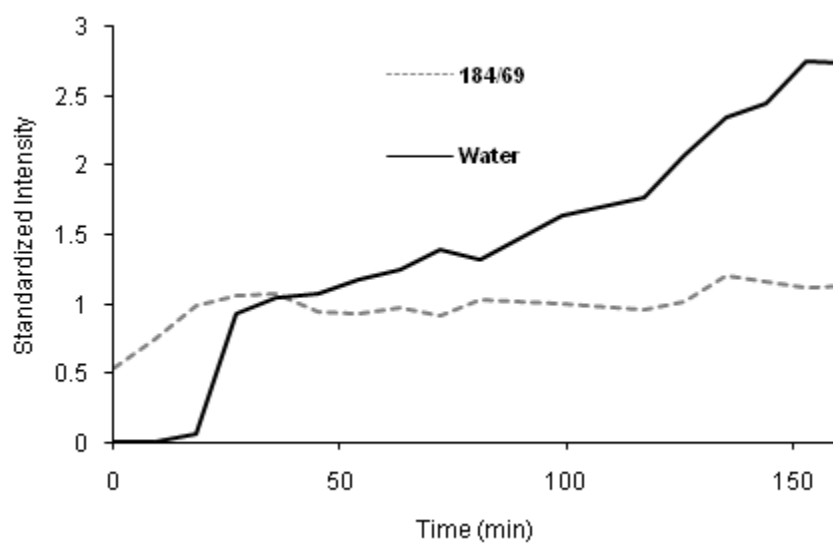


Figure 2-5. Relative intensity of PC headgroup as water is deposited on the surface of a spin coat lipid film. Relative intensity of m/z 18 is plotted to demonstrate increasing H₂O on the surface.

2.3.6 Imaging with cluster projectiles

The freeze-etching methodology is also compatible with analysis using cluster ion beams. Images of macrophages obtained using a 40 keV C_{60}^+ projectile as the primary ion, are shown in Figure 2-6. A high resolution image is shown in Figure 2-6A. To illustrate the ability of C_{60}^+ to image organic molecules of higher mass, the macrophages were labeled using DiI, a fluorophore that preferentially intercalates into the outer membrane of the cells. An image of a DiI-labeled cell is shown in Figure 2-6B. Analysis of water deposition on a cholesterol film using C_{60}^+ as the projectile demonstrates similar ionization increases, between 50 and 100%, to those observed with the In^+ beam, but are less stable with time (data not shown). Recent evidence from the literature,^{46, 47} and In^+ data from this study, support the supposition that water deposition enhances ionization efficiency when using cluster ions. It is possible that sampling depth will affect samples with vapor-deposited overlayers and this remains to be studied.

2.4 Conclusion

A novel alternative approach is presented to prepare reproducible bio-vacuum interfaces amenable to ToF-SIMS imaging analysis. This process exposes cells with the similar surface environments, making cell-to-cell comparisons feasible. During the preparation process the cell remains frozen, thus preserving the native state of the membrane as well as the spatial distribution of the lipid molecules. Matrix deposition occurs at low temperatures resulting in a matrix which does not impose a limit on lateral resolution.

Deposition of water from the vacuum environment serves to enhance the ionization efficiency of characteristic lipid fragments as well as high mass ions. Current evidence suggests that water interacting directly with the biological surface may donate protons resulting in the

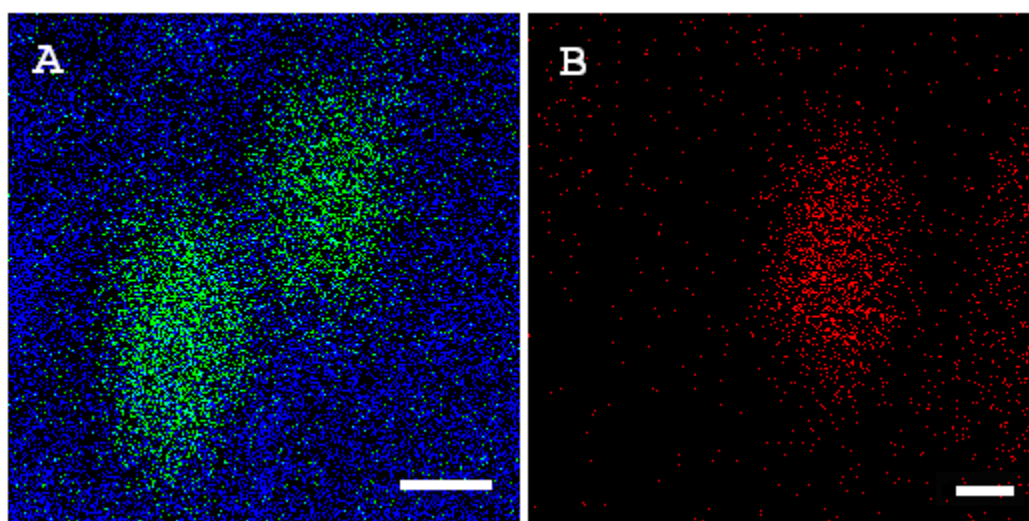


Figure 2-6. (A) SIMS overlay, m/z 184(PC) in green and m/z 18(H₂O) in blue, of 2 macrophages on a silicon substrate prepared by freeze-etching, intensity scale from 0-3. (B) SIMS image of m/z 834 showing DiI intercalated into the macrophage membrane, intensity scale 0-2. Scale bars represent 15 μm.

observed enhancement effect. If so, it should be feasible to deposit other compounds that may be better proton donors to further increase the enhancement observed with water ice. The deposition of water also serves to enhance the ionization of cholesterol though the role of water in the mechanism is currently not known.

The enhancement effect is stable over a period of hours, resulting in an “analysis window” in which the results of different images can be directly compared. The ability to produce a consistent and uniform surface environment will greatly improve the reproducibility of SIMS imaging and is essential to obtaining quantitative information from SIMS analyses.

These procedures yield high quality spectra both for atomic bombardment in the low dose mode, and with cluster bombardment. This strategy adds to the options available for producing cryogenically preserved single cells with high spatial integrity for SIMS analysis.

2.5 References

- (1) Simons, K.; Ikonen, E. *Nature* **1997**, *387*, 569-572.
- (2) Simons, K.; Toomre, D. *Nat. Rev.* **2000**, *1*, 31-41.
- (3) Huttner, W. B.; Zimmerberg, J. *Curr. Opin. Cell Biol.* **2001**, *13*, 478-484.
- (4) Burns, A. R. *Langmuir* **2003**, *19*, 8358-8363.
- (5) Veatch, S. L.; Polozov, I. V.; Gawrisch, K.; Keller, S. L. *Biophys. J.* **2004**, *86*, 2910-2922.
- (6) Burgos, P.; Yuan, C. B.; Viriot, M. L.; Johnston, L. J. *Langmuir* **2003**, *19*, 8002-8009.
- (7) Ge, M. T.; Gidwani, A.; Brown, H. A.; Holowka, D.; Baird, B.; Freed, J. H. *Biophys. J.* **2003**, *85*, 1278-1288.
- (8) Ritchie, K.; Iino, R.; Fujiwara, T.; Murase, K.; Kusumi, A. *Mol. Membr. Biol.* **2003**, *20*, 13-18.
- (9) Mukherjee, S.; Maxfield, F. R. *Annu. Rev. Cell Dev. Biol.* **2004**, *20*, 839-866.
- (10) Johansson, B. *Surf. Interface Anal.* **2006**, *38*, 1401-1412.
- (11) Roddy, T. P.; Donald M. Cannon, J.; Meserole, C. A.; Winograd, N.; Ewing, A. G. *Anal. Chem.* **2002**, *74*, 4011-4019.
- (12) Roddy, T. P.; Donald M. Cannon, J.; Ostrowski, S. G.; Winograd, N.; Ewing, A. G. *Anal. Chem.* **2002**, *74*, 4020-4026.
- (13) Cannon, D. M. J.; Pacholski, M. L.; Winograd, N.; Ewing, A. G. *J. Am. Chem. Soc.* **2000**, *122*, 603-610.
- (14) Chandra, S.; Bernius, M. T.; Morrison, G. H. *Anal. Chem.* **1986**, *58*, 493-496.

- (15) McDonnell, L. A.; Piersma, S. R.; Altelaar, A. F. M.; Mize, T. H.; Luxembourg, S. L.; Verhaert, P. D. E. M.; Minnen, J. v.; Heeren, R. M. A. *J. Mass Spectrom.* **2005**, *40*, 160-168.
- (16) Monroe, E. B.; Jurchen, J. C.; Lee, J.; Rubahkin, S. S.; Sweedler, J. V. *J. Am. Chem. Soc.* **2005**.
- (17) Peteranderl, R.; Lechene, C. *J. Am. Soc. Mass Spectrom.* **2004**, *15*, 478-485.
- (18) Marxer, C. G.; Kraft, M. L.; Weber, P. K.; Hutcheon, I. D.; Boxer, S. G. *Biophys. J.* **2005**, *88*, 2965-2975.
- (19) Parry, S.; Winograd, N. *Anal. Chem.* **2005**, *77*, 7950-7957.
- (20) Nygren, H.; Eriksson, C.; Malmberg, P.; Sahlin, H.; Carlsson, L.; Lausmaa, J.; Sjoval, P. *Colloid Surface B* **2003**, *30*, 87-92.
- (21) Ostrowski, S. G.; Szakal, C.; Kozole, J.; Roddy, T. P.; Xu, J. Y.; Ewing, A. G.; Winograd, N. *Anal. Chem.* **2005**, *77*, 6190-6196.
- (22) Winograd, N. *Anal. Chem.* **2005**, 143A-149A.
- (23) Xu, J.; Ostrowski, S.; Szakal, C.; Ewing, A. G.; Winograd, N. *Appl. Surf. Sci.* **2004**, *231-2*, 159-163.
- (24) Toubol, D.; Kollmer, F.; Niehus, E.; Brunelle, A.; Laprevote, O. *J. Am. Soc. Mass Spectrom.* **2005**, *16*, 1608-1618.
- (25) Altelaar, A. F. M.; Klinkert, I.; Jalink, K.; Lange, R. P. J.; Adan, R. A. H.; Heeren, R. M. A.; Piersma, S. R. *Anal. Chem. A* **2005**.
- (26) Wu, K. J.; Odom, R. W. *Anal. Chem.* **1996**, *68*, 873-882.
- (27) Adriaensen, L.; Vangaever, F.; Lenaerts, J.; Gijbels, R. *Rapid Commun. Mass Spectrom.* **2005**, *19*, 1017-1024.
- (28) Altelaar, A. F. M.; van Minnen, J.; Jimenez, C. R.; Heeren, R. M. A.; Piersma, S. R. *Anal. Chem.* **2005**, *77*, 735-741.
- (29) Marcus, A.; Winograd, N. *Anal. Chem.* **2006**, *78*, 141-148.
- (30) Kim, Y.-P.; Oh, E.; Hong, M.-Y.; Lee, D.; Han, M.-k.; Shon, H. K.; Moon, D. W.; Kim, H.-S.; Lee, T. G. *Anal. Chem.* **2006**, *78*, 1913-1920.
- (31) Luxembourg, S. L.; McDonnell, L. A.; Duursma, M. C.; Guo, X. H.; Heeren, R. M. A. *Anal. Chem.* **2003**, *75*, 2333-2341.
- (32) McCarthy, K. D.; DE Vellis, J. *J. Cycl. Nucleotide Res.* **1978**, *4*, 15-26.
- (33) Braun, R. M.; Blenkinsopp, P.; Mullock, S. J.; Corlett, C.; Willey, K. F.; Vickerman, J. C.; Winograd, N. *Rapid Commun. Mass Spectrom.* **1998**, *12*, 1246-+.
- (34) Wong, S. C. C.; Hill, R.; Blenkinsopp, P.; Lockyer, N. P.; Weibel, D. E.; Vickerman, J. C. *App. Surf. Sci.* **2003**, *203*, 219-222.
- (35) Weibel, D.; Wong, S.; Lockyer, N.; Blenkinsopp, P.; Hill, R.; Vickerman, J. C. *Anal. Chem.* **2003**, *75*, 1754-1764.
- (36) Fletcher, J. S.; Conlan, X. A.; Jones, E. A.; Biddulph, G.; Lockyer, N. P.; Vickerman, J. C. *Anal. Chem.* **2006**, *78*, 1827-1831.
- (37) Colliver, T. L.; Brummel, C. L.; Pacholski, M. L.; Swanek, F. D.; Ewing, A. G.; Winograd, N. *Anal. Chem.* **1997**, *69*, 2225-2231.
- (38) Severs, N.; Shotton, D., Eds. *Rapid Freezing, Freeze-Fracture, and Deep Etching*; Wiley-Liss: New York, 1995.
- (39) Murphy, R. C., Ed. *Mass Spectrometry of Lipids*; Plenum Press: New York, 1993.
- (40) Murphy, R. C., Ed. *Mass Spectrometry of Phospholipids: Tables of Molecular and Product Ions*; Illuminati Press: Denver, 2002.
- (41) Ostrowski, S. G.; Bell, C. T. V.; Winograd, N.; Ewing, A. G. *Science* **2004**, *305*, 71-73.
- (42) Delcorte, A. *App. Surf. Sci.* **2006**, *252*, 6582-6587.

- (43) Luxembourg, S. L.; McDonnell, L. A.; Duursma, M. C.; Guo, X. H.; Heeren, R. M. A. *Analytical Chemistry* **2003**, *75*, 2333-2341.
- (44) McQuaw, C. M.; Zheng, L. L.; Ewing, A. G.; Winograd, N. *Langmuir* **2007**, *23*, 5645-5650.
- (45) Roddy, T. P.; Jr., D. M. C.; Ostrowski, S. G.; Ewing, A. G.; Winograd, N. *Anal. Chem.* **2003**, *75*, 4087-4094.
- (46) Conlan, X. A.; Lockyer, N. P.; Vickerman, J. C. *Rapid Commun. Mass Spectrom.* **2006**, *20*, 1327-1334.
- (47) McDonnell, L. A.; Heeren, R. M. A.; de Lange, R. P. J.; Fletcher, I. W. *J. Am. Soc. Mass Spectrom.* **2006**, *17*, 1195-1202.

Chapter 3

MS/MS Methodology to Improve Sub-Cellular Mapping of Cholesterol Using ToF-SIMS

3.1 Introduction

There has been considerable interest in imaging mass spectrometry because of its potential to offer insight into countless biological processes.¹ Time-of-flight secondary ion mass spectrometry imaging is a powerful analytical tool for mapping the distribution of biologically relevant small molecules (<1000 Da) on a surface.²⁻⁷ Briefly, a pulsed beam of primary ions is directed at the analysis surface. The impact of the ions causes the sputtering of ions and molecules, which are then extracted into a TOF mass analyzer and a mass spectrum is generated. To obtain an image, the primary beam is raster scanned across the surface recording a mass spectrum for each pixel. Molecules of interest can be selected from the spectrum and their unique distributions mapped simultaneously across the imaging area.

Due to the surface sensitivity of the technique, much of its biological application has been in the study of the cell membrane lipids, such as phospholipids and cholesterol.^{2, 6, 8, 9} Cholesterol is a major constituent of nearly all mammalian cell membranes where its concentration is tightly controlled. In the membrane, cholesterol modifies the physical properties of the membrane as well as interacting differentially with various lipids and proteins in the formation of specialized microdomains.¹⁰⁻¹² ToF-SIMS combines submicron spatial resolution, chemical specificity and surface sensitivity, making it an excellent tool for the study of lipid domains within cellular membranes. The capability of ToF-SIMS to image sub-cellular features has been demonstrated in the literature.^{2, 6}

In the brain, cholesterol is involved in many important processes, namely synaptogenesis and myelin formation. Improper regulation of cholesterol in the brain has been implicated in multiple human brain diseases including Alzheimer's disease¹³. Improper cholesterol homeostasis is also implicated in atherosclerosis which can lead to myocardial infarction and stroke, as well as other disorders.¹⁴ Therefore, being able to detect and identify the distribution of cholesterol in biological samples has important implications in medical science.

Due to the high-energy nature of the SIMS ionization process, several larger molecules are identified by the detection of characteristic fragments. Commonly, fragments of the molecule of interest are identified using standard samples, and those fragments are used to map the location of the molecule. However, even single constituent samples can produce complex spectra. Many factors can affect the fragmentation pattern in a SIMS experiment including primary ion, matrix effects, molecular orientation, and surface contamination.^{4, 15-17} These factors complicate analysis and can make identification of characteristic fragments challenging.

In this chapter, I present the novel application of MS/MS methodology to identify characteristic fragment ions for use in imaging SIMS. A commercially available MALDI instrument, the QSTAR[®] XL manufactured by Applied Biosystems MDS Sciex, has been modified to incorporate a C₆₀⁺ primary ion source. This combination produced several advantages that can be utilized for improving biological SIMS.^{18, 19} Most notable for these experiments, was greatly increased mass resolution, mass accuracy, and MS/MS capability. Currently, the spatial resolution of this prototype instrument is limited to approximately 10 μm, limiting its use for many single-cell imaging experiments. However, it can provide valuable information to be used in conjunction with sub-micron resolution SIMS instrumentation. In SIMS experiments, cholesterol is seen as [M-OH]⁺ at m/z 369.35 and [M-H]⁺ at m/z 385.4.²⁰ Collision-induced dissociation of this ion revealed several candidate fragments whose intensities might make them more suitable for mapping experiments than the pseudomolecular ion. While

the relationship between CID fragments and primary ion impact fragments is only just now being explored, initial experiments in this lab show that they are often similar. The main advantage of using fragments generated by CID is that they have unambiguous origins. In addition, the MS/MS spectrum generated is often less complex.

The presence of the fragments in a single component spectrum using In^+ as the primary ion, was verified using pure cholesterol films. To validate the usefulness of the CID fragments for single cell imaging experiments, J774 macrophage cells were imaged before and after doping with cholesterol. The relative increases obtained were then compared with results using the pseudomolecular ion. I then demonstrate the improvement obtained in cell imaging experiments by displaying the fragments in mass specific images of macrophages.

3.2 Experimental Section

1.2.1 Hybrid quadrupole time-of-flight mass spectrometer

The front end of a QSTAR® XL system, a hybrid LC/MS/MS instrument originally designed for MALDI and electrospray ionization mass spectrometry (Applied Biosystems / MDS Sciex) was modified to fit a 20 keV C_{60}^+ source by Ionoptika Ltd. Details of the QSTAR® XL system and the 20 keV C_{60}^+ source can be found elsewhere.^{21, 22} Briefly, the QSTAR® XL system is a tandem quadrupole orthogonal time-of-flight mass spectrometer. In this instrument, nitrogen gas is used for collisional cooling and collisional focusing. The pressure of N_2 , on the order of 5 mTorr near the sample and collisional focusing quadrupole region (Q_0), is critical for efficient operation.²³⁻²⁵ With this configuration, $m/\Delta m$ resolution exceeding 12,000 has been obtained.

The C_{60}^+ ion source for these experiments was operated with 10-15 pA current on the sample in DC mode. MS/MS experiments were carried out using N_2 collision gas with a residual gas pressure of 4×10^{-5} .

Imaging is accomplished through movement of the sample stage up to 50 mm in either direction either in a stepped motion down to 10 μm or in a continuous motion. During stepped stage motion, the ion source beam is pulsed off with each stage movement. Data analysis is handled by Analyst® QS 2.0 software and sample stage motion is controlled by oMALDI™ Server 5.0 software, both by Applied Biosystems / MDS Sciex. Further image processing was completed with BIOMAP version 3.7.5.4 software.

3.2.2 In^+ SIMS

Spectra using In^+ primary ions was acquired using a Kratos Prism ToF-SIMS spectrometer (Manchester, U.K.) equipped with an In^+ liquid metal ion source (FEI, Beaverton, OR). The pulsed primary ion source was operated at an anode voltage of 15kV angled at 45° to the sample. The beam was focused to approximately 200 nm in diameter, and delivered 1 nA of DC current in 50 ns pulses. An extraction lens, biased at -4.7 kV, collected the secondary ions which then traveled along a 4.5-m flight path and were detected at a microchannel plate (MCP) detector (Galileo Co., Sturbridge, MA). Mass resolution for these experiments was $m/\Delta m$ 500.

3.2.3 C_{60}^+ SIMS

Data using C_{60}^+ primary ions was acquired using a BioToF ToF-SIMS spectrometer, described in detail elsewhere.²⁶ The spectrometer was equipped with a 40 KeV C_{60}^+ primary ion

source^{21, 27, 28} (Ionoptika Ltd., Southampton, U.K.). The source was operated with a 300 μm diameter beam defining aperture, yielding approximately 20 pA of DC current.

3.2.4 Preparation of cholesterol films

Physical vapor deposition (PVD) films were prepared by subliming cholesterol (Sigma-Aldrich, St. Louis, MO) contained in a crucible by resistive heating of a tungsten filament followed by deposition onto a LN₂-cooled sample stage. The film thickness was monitored using a quartz crystal microbalance (QCM), and subsequently characterized using AFM. Films used for this study had a thickness of 100 nm \pm 10 nm.

Polydimethylsiloxane (PDMS) films were prepared by soaking a 1 cm x 1 cm Sil-Tec silicone sheet (Technical Products, Inc.) in 5 mL Hexane. The solution was then drop dried onto a stainless steel substrate.

3.2.5 Relative quantification

J774 macrophage cells were cultured to confluence and subsequently separated into two populations. To label the two different cell populations as well as identify the outer leaflet of J774 cells after fracture, two fluorescent dyes 1,1'-dioctadecyl-3,3,3',3'-tetramethylindodicarbocyanine (DiD) and 1,1'-dioctadecyl-3,3,3',3'-tetramethylindocarbocyanine (DiI), (Molecular Probes, Eugene, OR) were used. Cholesterol loading was achieved by adding cholesterol- β -cyclodextrin (chol-BCD) (CDT, Inc., High Springs, FL) to the DiD labeled flask. The populations were incubated for 1 hr, then rinsed in serum-free media to remove excess dye, and plunge frozen for freeze fracture.²⁹ Fluorescence was monitored using a vertical illuminator microscope (Olympus, Melville, NY) that was

previously incorporated into the SIMS instrumental design.³⁰ A detailed description of methods used for relative quantification experiments can be found elsewhere.³¹

3.3 Results and Discussion

3.3.1 Cholesterol Fragmentation in SIMS Analysis

For biological mapping experiments, SIMS spectra are first obtained from single component standards, generally in the form of thin films. These analyses identify characteristic ions that can be used to map the location of these molecules in complex systems, such as biological cells. When using highly energetic primary ions to generate secondary ions from biological samples for analysis, complex spectra are obtained. A spectrum obtained from a pure film of cholesterol induced by 15 keV In⁺ bombardment is shown in Figure 3-1A. The lack of PDMS contamination is evidenced by the absence of other common contamination fragments at m/z 133, 207 and 221.

The QSTAR® XL instrumentation allows the utilization of MS/MS methodology to probe the fragmentation of cholesterol ions created by primary ion bombardment. The resultant MS/MS spectrum from the [M-OH]⁺, generated by C₆₀⁺ bombardment, is shown in Figure 3-1B. Collision-induced fragmentation produces two species in high quantity at m/z 147.12 and m/z 161.13. These species are nearly absent in the cholesterol spectrum obtained using C₆₀⁺, but are found in the In⁺ spectrum with higher intensity than the m/z 369 pseudomolecular ion traditionally used for cholesterol imaging using SIMS. The molecular ion is seen at m/z 385.4 in standard samples, but the pseudomolecular ion (m/z 369) is most commonly used due to its higher intensity. This suggests that these species may be useful for mapping cholesterol,

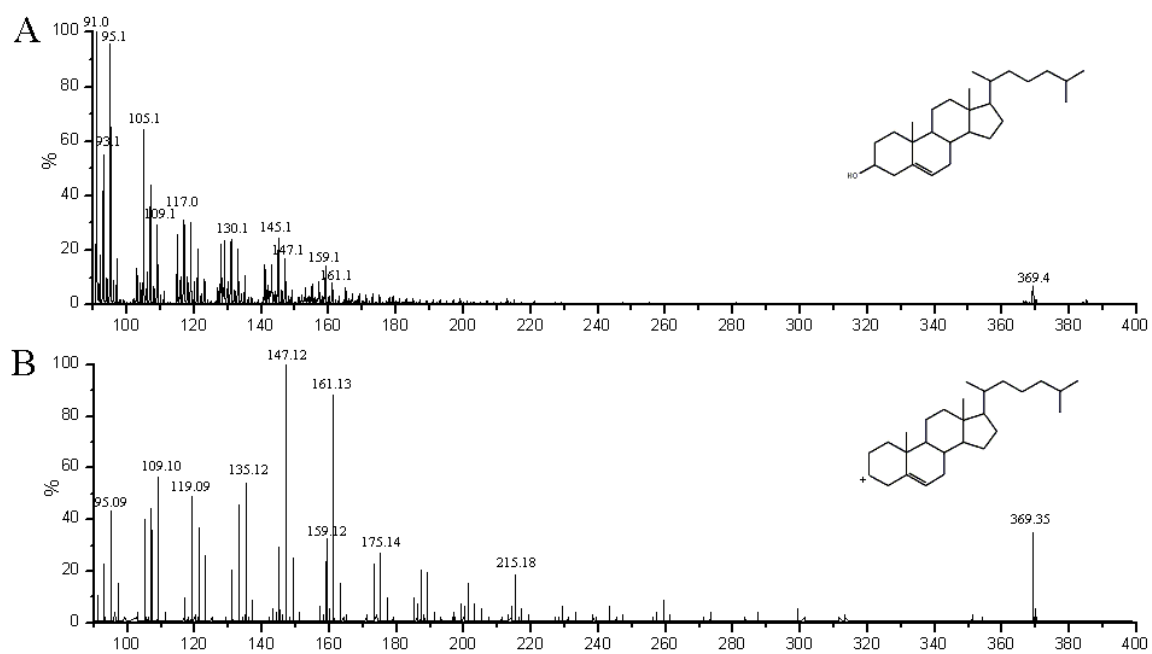


Figure 3-1. Mass spectra of cholesterol films. (A) In⁺ induced spectrum of a PVD cholesterol film. (B) MS/MS spectrum of [M-OH]⁺ ion derived from pure cholesterol film using N₂ as a collision gas. All spectra are standardized to largest peak in the viewing area.

particularly when limited ions are available for collection, as is the case in high resolution cell imaging experiments.

To quantify the signal intensity obtained for the various fragments, PVD cholesterol films were analyzed using In^+ and C_{60}^+ . The intensity was calculated by dividing the peak area for the fragment by the peak area for m/z 369. Results are shown in Table 3-1. This analysis suggests that the mapping of fragments should be most beneficial in the case of atomic projectiles. These analyses also demonstrate the decrease in fragmentation that occurs when utilizing cluster ion sources. This indicates the value of identifying characteristic fragments, even when employing cluster primary ions. It should also be noted that the absolute intensities (ions/primary ion) of fragments obtained using C_{60}^+ as the primary ion were 50 - 110 fold higher than those obtained employing In^+ . However, when imaging with a high-spatial resolution C_{60}^+ beam, primary ion currents are typically 100 fold lower than In^+ resulting in prohibitive data collections times to reach the static limit.

The $[\text{M-OH}]^+$ ion has been used extensively in biological imaging experiments,^{5, 9, 20, 31, 32} as it can be unambiguously attributed to cholesterol. For this reason and its high intensity, it was analyzed by MS/MS. It has been suggested in the literature³³ that the first step in the fragmentation is the disconnection of the aliphatic side chain. Direct evidence for this was not observed, as the side chain fragment or the intact sterol ring system was not observed in the mass spectrum. However, the fragments detected are derived from the sterol ring system, as was reported. The mass resolution of the QSTAR® XL allowed us to very accurately identify the elemental formulas of the fragment ions.

The major fragments can be explained by identifying two key fragmentation sites, shown in Figure 3-2. The complexity of the spectrum obtained suggests that fragmentation occurs at many sites, but to a much lesser extent. The stability of these fragments indicates that they would be good ions to measure in SIMS.

Table 3-1. Signal intensity of fragments reported as percentage of pseudomolecular ion intensity.

Material	Projectile	(m/z) ⁺			
		161	147	109	95
PVD Film	C ₆₀ ⁺	21 ± 7%	30 ± 9%	51 ± 9%	149 ± 5%
	In ⁺	155 ± 11%	310 ± 10%	538 ± 9%	1645 ± 9%
J774 Cells	In ⁺	177 ± 16%	260 ± 16%	443 ± 16%	1352 ± 9%

The reported numbers are the mean of 5 independent measurements of different areas of the surface from the same film. The reported cell numbers are the mean of 6 independent macrophage images. Errors reported are standard deviation.

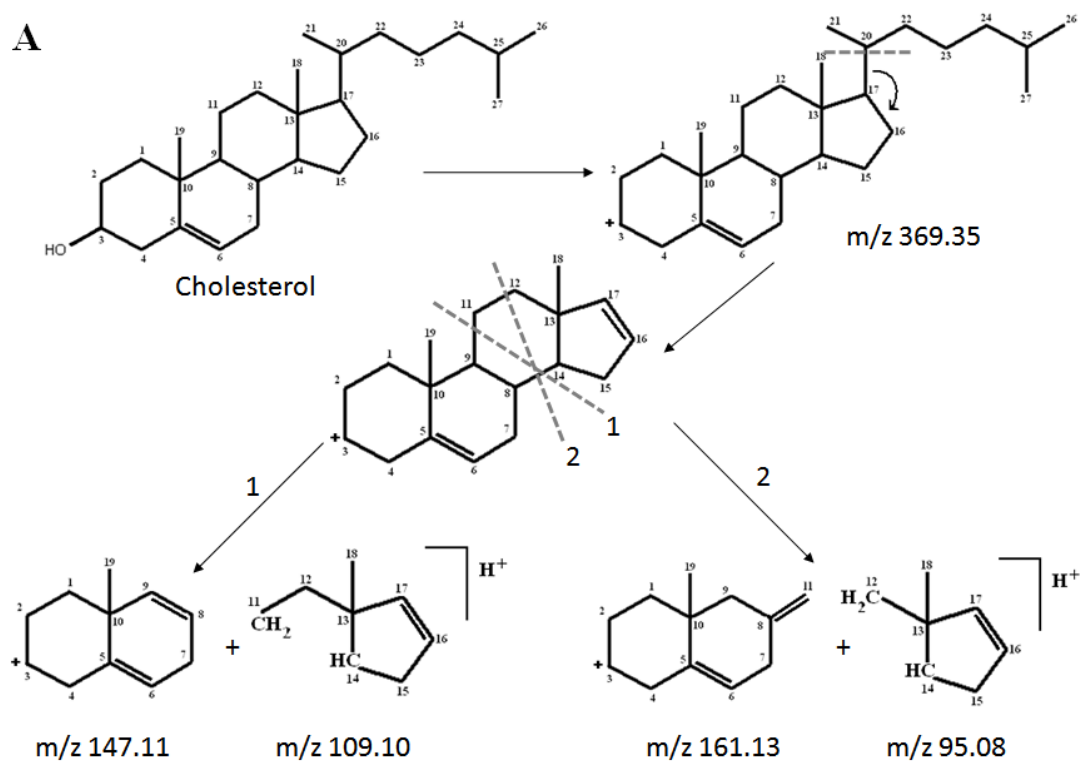


Figure 3-2. Proposed fragmentation scheme for cholesterol from MS/MS analysis.

3.3.2 Isobaric Interferences and Contamination

The nominal mass 147 has long been known to be indicative of PDMS, a prevalent contaminant in SIMS analysis³⁴. It is believed that the existence of this contaminant has prevented the identification of this major fragment.

To demonstrate that the m/z 147 fragment in the MS/MS spectrum is not the result of contamination, a thin film of pure cholesterol was placed next to a thin film of PDMS. Figure 3-3A shows a mass spectrum obtained from the PDMS film. The m/z 147.065 peak is easily identified along with other characteristic fragments seen with PDMS: m/z 73.05, m/z 149.04, and m/z 209.02. When a mass spectrum is obtained from the cholesterol film, these fragments are nearly absent, indicating little or no contamination. A spectrum of a cholesterol film induced by 20 keV C_{60}^+ cluster ion bombardment can be seen in Figure 3-3B. This analysis yields a simpler spectrum than In^+ with a larger contribution coming from the $[M-OH]^+$. However, significant fragmentation is observed resulting in a different pattern when compared to that obtained with In^+ . This suggests that when employing other primary ion sources, fragments other than those observed with In^+ may be more valuable.

To further demonstrate the difference between the two species obtained around m/z 147, an image of the junction of these two plates was obtained. Figure 3-3C shows a blow-up of the 147 mass region; the peaks at m/z 147.065 and m/z 147.117 are fully resolved. In Figure 3-3D, a mass specific SIMS image of the two masses shows that 147.065 localizes to the PDMS covered sample and the 147.117 localizes to the cholesterol-coated sample. In combination with MS/MS data, this decisively shows that m/z 147.117 is derived from cholesterol. These experiments also demonstrate the value of improved mass resolution for ToF-SIMS imaging experiments.

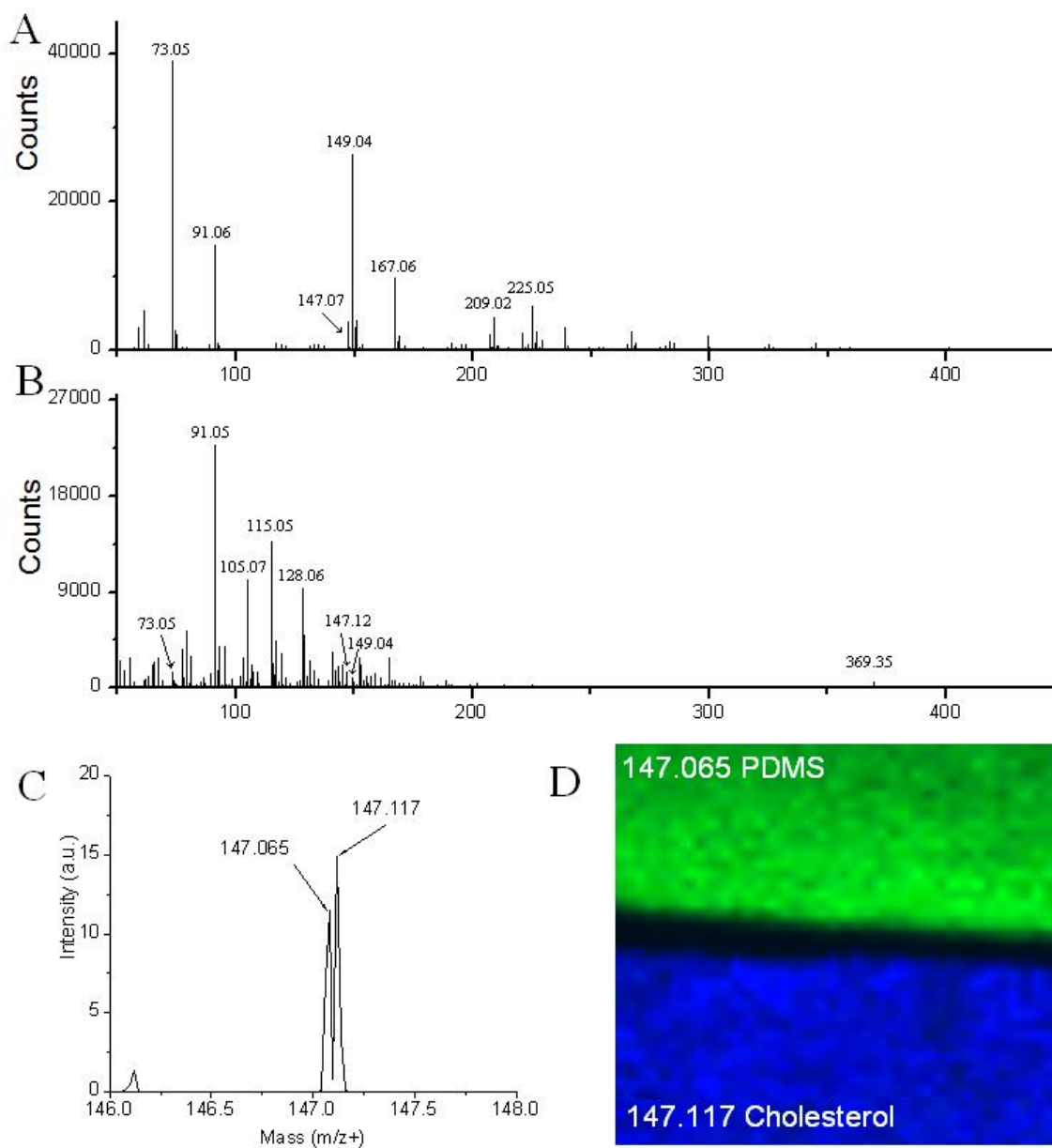


Figure 3-3. Discriminating contaminant peaks. (A) Mass spectrum generated from the PDMS coated sample. (B) Mass spectrum generated from the cholesterol coated sample. (C) Orthogonal ToF-SIMS imaging of the junction of two sample plates; one coated with cholesterol (m/z 147.117 = blue), and one coated with PDMS (m/z 147.065 = green). (D) Resulting mass spectrum with $m/\Delta m$ resolution of 8000. Data taken by Anthony Carado.

3.3.3 Isobaric interferences in cell imaging

In a standard ToF- SIMS experiment, the ToF region is coupled to the secondary ion ejection process. The energy spread inherent to the sputtering process limits the attainable mass resolution for these imaging experiments. Hence, the mass resolution shown above is not currently available to single cell imaging experiments. To determine if the m/z 147 observed in these experiments was derived from cholesterol, relative quantification experiments measuring cholesterol were examined.

A J774 cell population was split, half were incubated with DiD and chol-BCD, and the other with DiI, as previously reported.³¹ The chol-BCD complex is water soluble and facilitates cholesterol loading. Therefore, the treated cell population is expected to have a higher concentration of cholesterol in the outer membrane. The DiI and DiD are fluorophores that preferentially intercalate into the outer leaflet of the cell membrane, creating a marker to differentiate the two cell populations. After incubation, the cells were rinsed, mixed together and allowed to settle on Si substrates.

The samples were prepared for imaging using freeze-fracture methodology.³ Treated and non-treated populations were differentiated using *in situ* fluorescence microscopy. By imaging the two different cell populations in the same field of view, the cholesterol content could be compared. Quantification was performed by analyzing line scans across the images; a plot of the signal intensity for a given ion as a function of its lateral position on the line shown on the image (inset). By drawing the line across 2 cells from different populations, as demonstrated in Figure 3-4A inset, the signal intensities are displayed on a single plot. For the image shown, the line scan begins in the lower left.

Figure 3-4A shows the line scans for each individual fragment from the image. It is clear from these scans that signal intensity is greater in the first cell, and the fluorescence measurement

indicates this cell was from the chol-BCD treated population. A rise in fragment signal was observed for all of the fragments after incubation with chol-BCD. It can be seen in the Figure 3-4A inset that the size of the two cells appears to be different. This disparity is accounted for in relative quantification experiments through the use of m/z 69 as an internal standard.^{2, 6, 31} Additionally, the ratio of the peak areas from treated cell to control cell are appreciably different for some of the fragments analyzed, m/z 109 and m/z 95. This suggests that these fragments are less discriminatory indicators of cholesterol concentration.

To better understand why some fragment ions are better indicators of cholesterol, the relative quantification data was analyzed using the fragments characterized in this work. The results are summarized in Table 3-2. Cholesterol molecular ion is shown in the last column as a comparison. Since m/z 369 appears in a region of the spectrum with few other peaks, it is hypothesized that isobaric interference is least for this ion. For this reason, results obtained for the fragment ions were statistically compared to the measurement from the pseudomolecular ion (Student's t-test). The p-values obtained for each fragment are shown in the bottom row of the table. It can be seen from this analysis that m/z 109 is significantly different than the molecular ion, and that difference for m/z 95 tends toward significance. It is hypothesized that this discrepancy is due to other species present in these complex samples that are difficult to differentiate due to a lack of mass resolution. This implies that these masses are not very selective diagnostic peaks for cholesterol. Despite the interference, cholesterol undoubtedly contributes to the signal intensity observed at these two masses, indicating that these fragments can still be useful for imaging cholesterol distribution.

Table 3.2. Relative cholesterol increase in treated cells utilizing the identified fragments.

	(m/z)⁺				
	161	147	109	95	369
% Increase	146 ± 44	178 ± 34	134 ± 17	149 ± 8	187 ± 45
p-value	0.14	0.69	0.02	0.07	

The relative cholesterol increase in treated cells calculated for various cholesterol fragments. Errors reported are standard deviations, n=6 for all measurements. The p-values are reported from a t-test comparing the calculated increase using the fragment, to the increase found using the pseudomolecular ion.

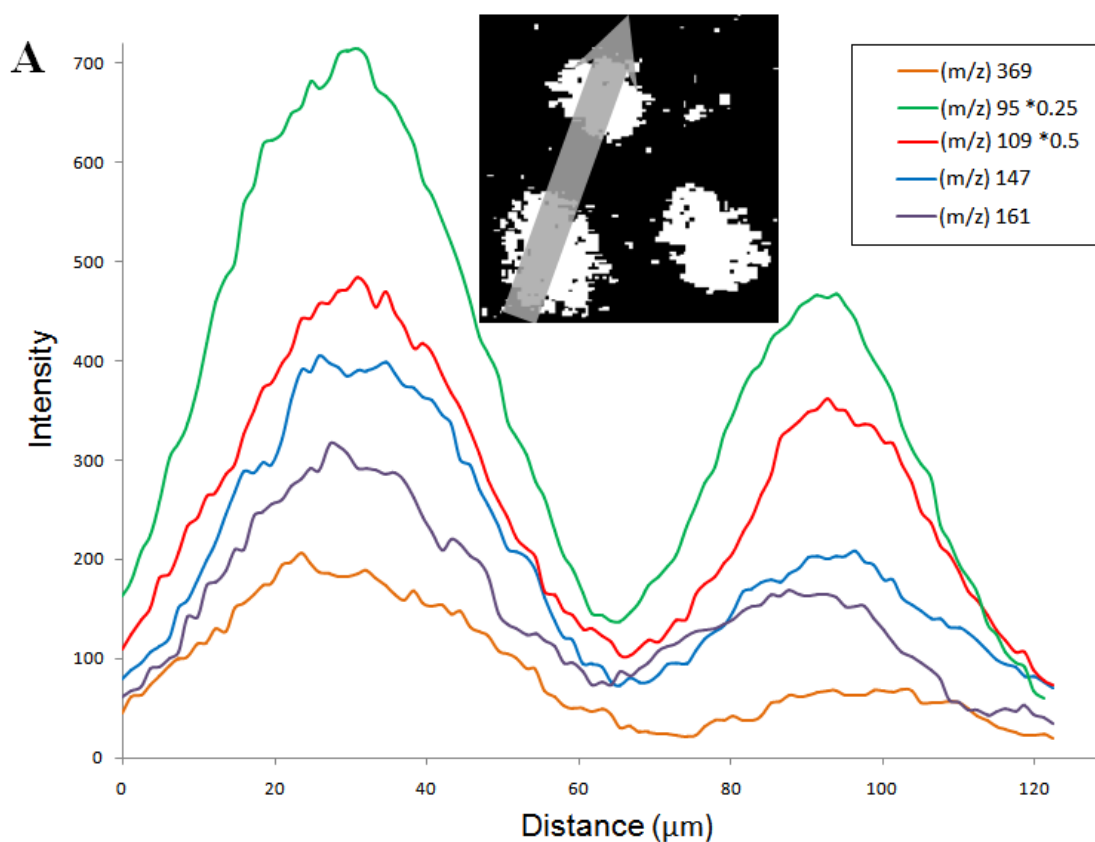


Figure 3-4. Cholesterol fragment ion intensity versus distance. Line scans of cholesterol fragment ion intensity across two cells demonstrates the uniformity of the internal standard use for quantification. The inset shows the path of the line scan which begins in the bottom left. The cell to the bottom left was treated with cholesterol vs. the cell above which was control. Original data taken by Sara Ostrowski.

The best correlation for these measurements is obtained from the m/z 147 fragment. This fragment also shows a much smaller standard deviation than m/z 369, likely due to the gain in signal to noise ratio. This analysis suggests this fragment would give the most accurate measure of cholesterol concentration. Moreover, this fragment appears with the largest intensity in the MS/MS spectrum, which is indicative of its stability.

3.3.4 Imaging with fragments

These fragments are useful to single cell imaging experiments. An example of this is shown in Figure 3-5. The Indium ion source was employed as it provides higher spatial resolution required for imaging single cells. These images illustrate the increase in signal that is obtained when fragment peaks are used to map cholesterol on the surface. Although employing m/z 369 provides enough signal to compare concentrations, little or no information is obtained about the sub-cellular distribution of cholesterol on the cells surface. However, when higher intensity fragments are mapped a much more detailed description of the surface is obtained, allowing us to probe cholesterol concentration at discrete locations on the cell surface.

Table 3-1 shows the intensity increase when compared to the m/z 369 ion, as shown above for the different projectiles. These images were obtained using In^+ primary ion. When compared to Figure 3-2B, these numbers resemble those obtained from the cholesterol standard. The decrease in relative intensity is likely due to the lower concentration of cholesterol at the surface of the membrane when compared to the surface of a PVD film. This indicates that under these well controlled sample conditions, matrix effects play a limited role in the ionization process and further supports the proposition that these fragments are derived from cholesterol.

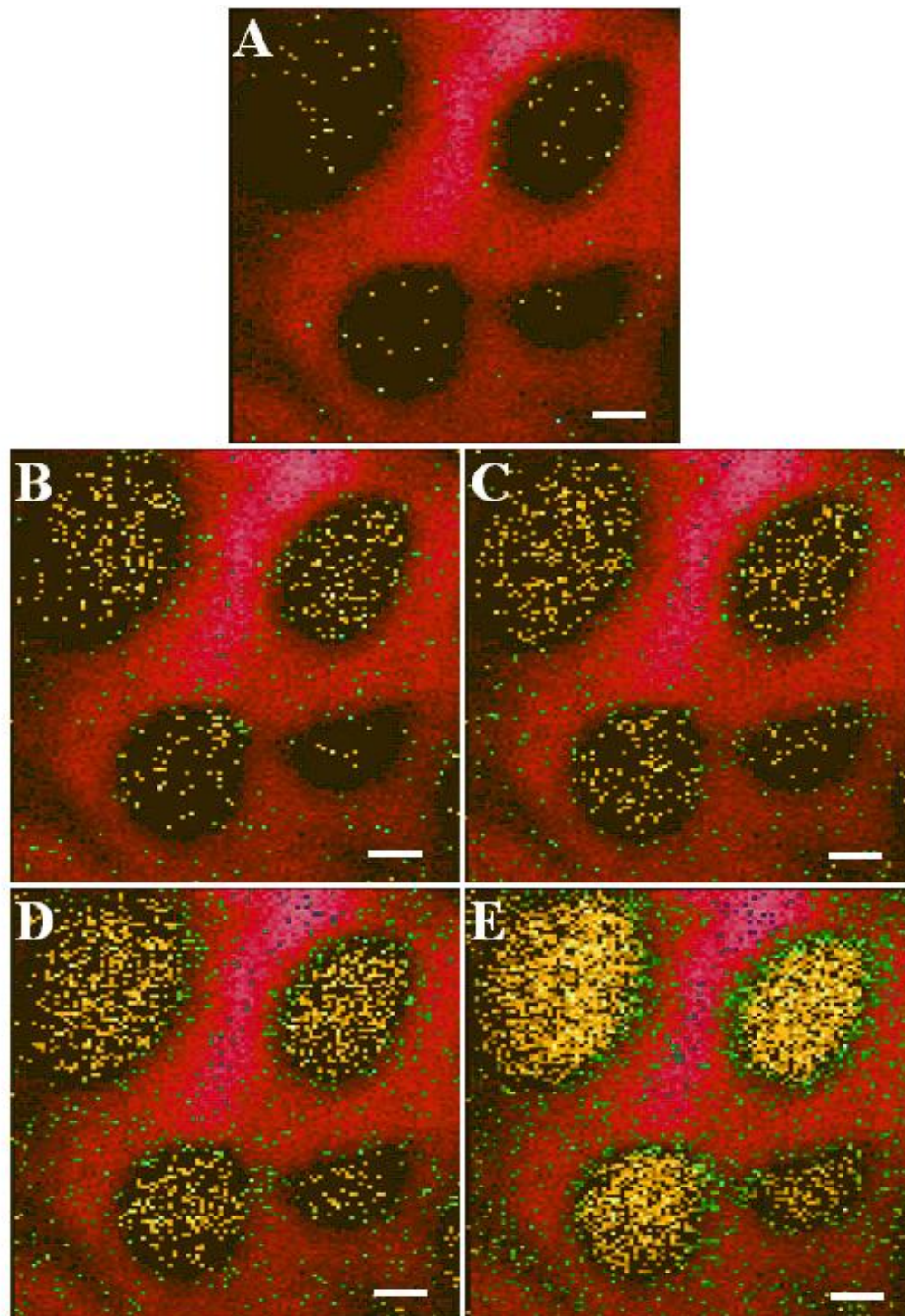


Figure 3-5. SIMS imaging of macrophage cells. SIMS overlay images of the Cholesterol fragment ions (Yellow) vs. Na m/z 23 (Red), green pixels denote the presence of both ions on macrophages. All scale bars are 10 μm . A.) m/z 369 B.) m/z 161 C.) m/z 147 D.) m/z 109 E.) m/z 95.

The strong localization of the m/z 147 ion to the surface of the cell shows that there is little PDMS contamination with this sample. With a contaminated sample, a more dispersed signal would be expected. The low values for standard deviation demonstrate the utility of m/z 69 as an internal standard for single cell imaging experiments; and further validates the rigorous protocols developed in this lab for making relative quantification measurements.³¹ Moreover, this demonstrates that relative intensity measurements are sensitive to surface concentrations.

3.4 Conclusions

New diagnostic fragments have been uncovered for the analysis of cholesterol using ToF-SIMS imaging using MS/MS methodology. The m/z 147 fragment of cholesterol has been resolved from that for PDMS using the higher resolution QSTAR® XL instrument. The use of these fragments improves the capability of SIMS to quantify and image cholesterol, particularly in single cells.

Relative quantification experiments reveal that increasing the content of cholesterol in cells results in a corresponding increase in cholesterol fragments. When analyzing a complex biological sample with low mass resolution, isobaric interferences are unavoidable. For the lower mass fragments, these interferences were shown to be problematic for relative quantification experiments and could be misleading in imaging experiments with low signal to noise ratios. Comparison of fragments with $[M-OH]^+$ reveal that m/z 147 most closely resembles the molecular ion, indicating the least isobaric interference. Moreover, this fragment appears with the largest intensity in the MS/MS spectrum, which is indicative of its stability.

These findings demonstrate the potential for the application of MS/MS methodology to ToF-SIMS bioimaging. The identification of novel and useful diagnostic fragments of biomolecules is central to the advancement of the technique. In this particular case, characteristic

fragments of an extensively analyzed molecule have been overlooked. This new knowledge, along with TOF data sets, allows for past analyses to be re-evaluated. This illustrates the value of retrospective imaging capabilities permitted when employing ToF-MS. Furthermore, these findings reveal the need for improved mass resolution in SIMS imaging experiments. When analyzing an incredibly complex system such as the cellular membrane, improved mass resolution is crucial to the identification of unknown peaks and elimination of isobaric interference. It is probable that substantial biological complexity is being lost in the noise, due to a lack of mass resolution.

3.5 References

- (1) McDonnell, L. A.; Heeren, R. M. A. *Mass Spectrom. Rev.* **2007**, *26*, 606-643.
- (2) Monroe, E. B.; Jurchen, J. C.; Lee, J.; Rubakhin, S. S.; Sweedler, J. V. *J. Am. Chem. Soc.* **2005**, *127*, 12152-12153.
- (3) Colliver, T. L.; Brummel, C. L.; Pacholski, M. L.; Swanek, F. D.; Ewing, A. G.; Winograd, N. *Anal. Chem.* **1997**, *69*, 2225-2231.
- (4) Pacholski, M. L.; Donald M. Cannon, J.; Ewing, A. G.; Winograd, N. *J. Am. Chem. Soc.* **1999**, *121*, 4716-4717.
- (5) McDonnell, L. A.; Piersma, S. R.; Altelaar, A. F. M.; Mize, T. H.; Luxembourg, S. L.; Verhaert, P. D. E. M.; Minnen, J. v.; Heeren, R. M. A. *J. Mass Spectrom.* **2005**, *40*, 160-168.
- (6) Ostrowski, S. G.; Bell, C. T. V.; Winograd, N.; Ewing, A. G. *Science* **2004**, *305*, 71-73.
- (7) Rubakhin, S. S.; Jurchen, J. C.; Monroe, E. B.; Sweedler, J. V. *Drug Discov. Today* **2005**, *10*, 823-837.
- (8) Nygren, H.; Malmberg, P. *Trends Biotechnol.* **2007**, *25*, 499-504.
- (9) Altelaar, A. F. M.; Klinkert, I.; Jalink, K.; Lange, R. P. J.; Adan, R. A. H.; Heeren, R. M. A.; Piersma, S. R. *Anal. Chem. A* **2005**.
- (10) Mukherjee, S.; Maxfield, F. R. *Annu. Rev. Cell Dev. Biol.* **2004**, *20*, 839-866.
- (11) Mukherjee, S.; Zha, X. H.; Tabas, I.; Maxfield, F. R. *Biophys. J.* **1998**, *75*, 1915-1925.
- (12) Davey, A. M.; Walvick, R. P.; Liu, Y. X.; Heikal, A. A.; Sheets, E. D. *Biophys. J.* **2007**, *92*, 343-355.
- (13) Valenza, M.; Cattaneo, E. *Prog. Neurobiol.* **2006**, *80*, 165-176.
- (14) Hansson, G. K.; Robertson, A. K. L.; Soderberg-Naucler, C. *Annu. Rev. Pathol. Mech. Dis.* **2006**, *1*, 297-329.
- (15) Piehowski, P. D.; Kurczy, M. E.; Willingham, D.; Parry, S.; Heien, M. L.; Winograd, N.; Ewing, A. G. *Langmuir* **2008**, *24*, 7906-7911.
- (16) Prinz, C.; Hook, F.; Malm, J.; Sjoval, P. *Langmuir* **2007**, *23*, 8035-8041.

- (17) Luxembourg, S. L.; McDonnell, L. A.; Duursma, M. C.; Guo, X. H.; Heeren, R. M. A. *Anal. Chem.* **2003**, *75*, 2333-2341.
- (18) Carado, A.; Kozole, J.; Passarelli, M.; Winograd, N.; Loboda, A.; Bunch, J.; Wingate, J.; Hankin, J.; Murphy, R. *Appl. Surf. Anal.* **2008**.
- (19) Carado, A.; Kozole, J.; Passarelli, M.; Winograd, N.; Loboda, A.; Wingate, J. *Appl. Surf. Anal.* **2008**.
- (20) Sostarecz, A. G.; McQuaw, C. M.; Ewing, A. G.; Winograd, N. *J. Am. Chem. Soc.* **2004**, *126*, 13882-13883.
- (21) Weibel, D.; Wong, S.; Lockyer, N.; Blenkinsopp, P.; Hill, R.; Vickerman, J. C. *Anal. Chem.* **2003**, *75*, 1754-1764.
- (22) Cotter, R. J.; Gardner, B. D.; Iltchenko, S.; English, R. D. *Anal. Chem.* **2004**, *76*, 1976-1981.
- (23) Douglas, D. J.; French, J. B. *J. Am. Soc. Mass Spectrom.* **1992**, *3*, 398-408.
- (24) Krutchinsky, A. N.; Chernushevich, I. V.; Spicer, V. L.; Ens, W.; Standing, K. G. *J. Am. Soc. Mass Spectrom.* **1998**, *9*, 569-579.
- (25) Loboda, A. V.; Krutchinsky, A. N.; Bromirski, M.; Ens, W.; Standing, K. G. *Rapid Commun. Mass Spectrom.* **2000**, *14*, 1047-1057.
- (26) Braun, R. M.; Blenkinsopp, P.; Mullock, S. J.; Corlett, C.; Willey, K. F.; Vickerman, J. C.; Winograd, N. *Rapid Commun. Mass Spectrom.* **1998**, *12*, 1246-+.
- (27) Wong, S. C. C.; Hill, R.; Blenkinsopp, P.; Lockyer, N. P.; Weibel, D. E.; Vickerman, J. C. *App. Surf. Sci.* **2003**, *203*, 219-222.
- (28) Fletcher, J. S.; Conlan, X. A.; Jones, E. A.; Biddulph, G.; Lockyer, N. P.; Vickerman, J. C. *Anal. Chem.* **2006**, *78*, 1827-1831.
- (29) Cannon, D. M. J.; Pacholski, M. L.; Winograd, N.; Ewing, A. G. *J. Am. Chem. Soc.* **2000**, *122*, 603-610.
- (30) Roddy, T. P.; Donald M. Cannon, J.; Meserole, C. A.; Winograd, N.; Ewing, A. G. *Anal. Chem.* **2002**, *74*, 4011-4019.
- (31) Ostrowski, S. G.; Kurczy, M. E.; Roddy, T. P.; Winograd, N.; Ewing, A. G. *Anal. Chem.* **2007**, *79*, 3554-3560.
- (32) Nygren, H.; Eriksson, C.; Malmberg, P.; Sahlin, H.; Carlsson, L.; Lausmaa, J.; Sjoval, P. *Colloid Surface B* **2003**, *30*, 87-92.
- (33) Rossmann, B.; Thurner, K.; Luf, W. *Monatsh. Chem.* **2007**, *138*, 436-444.
- (34) Vickerman, J. C.; Briggs, D., Eds. *ToF-SIMS: Surface Analysis by Mass Spectrometry*; IM Publications and Surface Spectra Limited: West Sussex, 2001.

Chapter 4

ToF-SIMS Imaging of Sub-Cellular Lipid Heterogeneity: Poisson Counting and Spatial Resolution

4.1 Introduction

Imaging with time-of-flight secondary ion mass spectrometry (ToF-SIMS) is a powerful analytical tool for mapping the spatial distribution of biologically relevant small molecules (<1000 Da) on a surface.¹ Due to the inherent surface sensitivity of the technique, ToF-SIMS has been used for the study of cell membrane lipids, such as phospholipids and cholesterol.²⁻⁵ Primary ion sources employed for ToF-SIMS experiments are not diffraction-limited, and thus provide nanometer-scale spatial resolution.⁶⁻⁹ The desorbed ions are analyzed using ToF, which provides high chemical specificity. Recent advances in MS instrumentation used to analyze secondary ions promise to greatly increase the chemical specificity available for imaging experiments.^{10,11} When combined with cryogenic sample preparation techniques, ToF-SIMS permits the detailed study of membrane lipids during dynamic processes such as membrane fusion.¹²⁻¹⁴

The capability of ToF-SIMS to image sub-cellular features of the plasma membrane has been previously demonstrated; however, these features were significantly larger than the minimum pixel size available for the analysis.^{2,3} Further, these features appeared in distinct cellular locations on the cell that allowed for features to be easily identified via a line scan (a plot of the signal intensity for a given ion as a function of its lateral position on the line). Analyzing small features becomes difficult as feature size approaches the minimum pixel size, an experimental limit imposed by the focus of the primary ion beam. Indeed, when characterizing these small features, signal averaging cannot be used, making it necessary to compare fewer

pixels to one another. The concept of useful lateral resolution, ΔL , has long existed in the SIMS community.¹⁵ ΔL is defined as the side of the minimum square area in which N secondary ions of a given mass can be desorbed and detected.^{16, 17} Traditionally, an N of 4 was considered to be useful.¹⁶ This concept accounts for the finite amount of ions generated for detection from small sample volumes. This definition is, however, inadequate when imaging a small number of pixels.

Keenan and Kotula have shown that consideration of counting statistics improves the quality of multivariate analyses applied to ToF- SIMS data.¹⁸ Because SIMS images are compiled by counting relatively rare events, ions of interest striking a detector, the resulting distribution of the intensities measured must be considered. Thus, an image of a uniform surface will not appear uniform because the pixel intensities follow a binomial distribution. This distribution precludes the direct comparison of two individual pixels and complicates the interpretation of imaging data. Thus, when analyzing small volumes, one must also consider factors which influence the intensity for a molecule of interest, i.e. the surface concentration, the change in concentration expected, the effective ionization efficiency, and the spot size of the primary ion source.

In this work, we demonstrate that SIMS imaging data can be accurately modeled using the Poisson distribution. By analyzing the data in this manner, a better understanding and more robust interpretation of the surface composition are obtained. This approach allows the identification and validation of pixel-to-pixel heterogeneity not possible with line scans. This capability allows the interrogation of lipid domains, which can appear anywhere on the cell surface and with sizes smaller than a single pixel.

To test this approach, phospholipid and cholesterol distributions on the surfaces of RBL-2H3 mast cells were imaged. Cholesterol-rich microdomains within the plasma membrane of these cells have been hypothesized to play functionally important roles in immunoreceptor signaling in the allergic response.^{19, 20} However, directly observing the spatial arrangement of

these domains, and the lipids that comprise them, *in situ* with good spatial resolution and relevant chemical information has remained elusive due to their size and lifetime.^{21,22} In this chapter, I describe a model using simulated data that allows signal and spatial resolution limitations to be predicted. The model is then applied to the analysis of RBL-2H3 cell images. The analysis reveals multiple intensity populations existing on the surface of the cell. The presence of multiple populations provides compelling evidence for a heterogeneous distribution of lipid species in the resting RBL-2H3 cell membrane.

4.2 Materials and Methods

4.2.1 Cell preparation for imaging

RBL-2H3 mast cells were suspended in BSA-containing buffered saline solution (20 mM HEPES, pH 7.4, 135 mM NaCl, 5 mM KCl, 1.8 mM CaCl₂, 1 mM MgCl₂, 5.6 mM glucose, 1 mg/mL BSA) and sensitized with a 10-fold molar excess of mouse-anti-2,4-dinitrophenyl IgE. Cells were incubated for 2 h at 4 °C. Cells were then diluted (1×10^6 cells/mL), applied to 5 mm \times 5 mm Si substrates and allowed to adhere (10 min, 37.4 °C).²² Shards containing RBL-2H3 cells were rinsed for 5 s in 18 M Ω water to remove contamination from excess media. To prevent cell rupture, the shards were quickly frozen in liquid ethane and stored under liquid nitrogen (LN₂). The samples were introduced to the ultra high vacuum environment of the mass spectrometer at LN₂ temperatures, as described elsewhere.¹⁴ Once under vacuum, the samples were warmed 5 °C/ min to -80 °C to remove the water with negligible crystallization. This process was monitored using a video camera mounted on a brightfield microscope. When the water was removed, the sample was quickly returned to liquid nitrogen temperatures. During the

cooling process, some residual water in the vacuum environment was re-deposited on the sample producing a uniform layer of water on top of the cells.²³

Langmuir-Blodgett and physical vapor deposition film preparation. The phospholipids used include *N*-stearoyl sphingomyelin (SSM), 1-palmitoyl-2-oleoyl-*sn*-glycero-3-phosphocholine (POPC), and cholesterol (CH). The LB films used for the investigation were either pure POPC or 23% CH/47% SM/30% PC. The lipids were applied to the air-water interface, compressed to 7 mN/m, and then transferred onto hydrophilic substrates. This relatively low pressure is used to ensure the appearance of immiscible liquid phases and to ensure that the size of the domains is large enough for SIMS observation.

Physical vapor deposition (PVD) films were prepared by subliming cholesterol (Sigma-Aldrich, St. Louis, MO) contained in a crucible by resistive heating of a tungsten filament followed by deposition onto a LN₂-cooled sample stage. The film thickness was monitored using a quartz crystal microbalance (QCM), and subsequently characterized using AFM.

4.2.2 Mass spectrometer

Imaging data was acquired using a Kratos Prism ToF-SIMS spectrometer (Manchester, U.K.) equipped with an In⁺ liquid metal primary ion source (FEI, Beaverton, OR). The pulsed primary ion source was operated at an anode voltage of 15kV angled at 45° to the sample. The beam was focused to approximately 300 nm in diameter, and delivered 1 nA of DC current in 50 ns pulses. The sample was mounted onto a LN₂-cooled analysis stage (Kore Tech. Ltd, Cambridge, U.K.) biased at +2.5 kV, 2.5 inches from a cold trap that was also cooled with LN₂. An extraction lens, biased at -4.7 kV, collected the secondary ions which then traveled along a 4.5-m flight path and were detected with a microchannel plate (MCP) detector (Galileo Co., Sturbridge, MA).

4.2.3 Data collection and image analysis

Mass spectrometry images were acquired by raster-scanning the primary ion beam across the sample region and collecting a mass spectrum for each pixel. The data were collected using in-house imaging software (visual C++, Microsoft, Redmond, WA). Imaging data was imported into MATLAB (Mathworks, Natick, MA) for analysis. Individual masses were plotted with their intensities displayed on a false color scale to better portray image details. Image binning was achieved by mathematically combining adjacent pixels. Histograms were created by first using an ROI tool created in LabView to select the cell or film area. The data was then exported to Microsoft Excel and histograms were plotted and fitted using the built-in function from the Analysis ToolPak. Multiple Poisson distributions were applied to the histogram and the means and partial contributions were allowed to vary. The solver function varied these parameters to minimize variance and thus provide the best fit.

4.2.4 Model calculations

The basic equation that describes the ion yield in a static SIMS experiment was used to obtain expected yields for imaging experiments.²⁴

$$I_m = I_p Y_m \alpha^+ \theta_m \eta \quad (\text{Eq.1})$$

Where the secondary ion current, I_m , is the product of the primary ion flux, I_p , the sputter yield, Y_m , the ionization probability to positive ions, α^+ , the molecules' fractional concentration, θ_m , and the transmission of the instrument, η . By measuring the secondary ion yields from pure films on the mass spectrometer to be used for imaging, an effective ionization efficiency can be calculated, which is the product of $Y_m \alpha^+ \eta$. Assuming that images are obtained by adhering to the static limit²⁴, 10^{13} impacts/cm² for the total primary ion flux can be used. Using the total dosage for I_m ,

results in the calculation of the total secondary ion yield. This leaves only the estimation of the molecules fractional concentration, which appears frequently in the literature.²⁵ The calculated secondary ion yield, from Eq. 1, can then be used in the Poisson equation for λ , to generate the probability mass function (relative number of events versus expected counts). If the expected number of ions counted is λ , then the probability of there being exactly k counts is defined by the Poisson distribution.

$$f(k; \lambda) = \frac{\lambda^k e^{-\lambda}}{k!} \quad (\text{Eq. 2})$$

When surface concentrations are considered as distributions, the potential overlap of these distributions must be estimated using a z-score to determine the accuracy of the experiment. The z-score is the difference in the means of two different populations given in the number of standard deviations. This is indicative of how accurately a pixel can be assigned to a given population.

$$z = \frac{\mu_2 - \mu_1}{\sigma_m} \quad (\text{Eq. 3})$$

where μ_2 is the mean intensity of the higher concentration, μ_1 is the mean intensity of the lower concentration and σ_m is the standard deviation calculated from the mean ion intensity. Because of the shape of the Poisson distribution, the standard deviation is equal to $\sqrt{\mu}$.

To assess the goodness-of-fit for imaging data, reduced χ^2 values were calculated. Briefly, the reduced χ^2 is the variance of the imaging data divided by the variance predicted by the Poisson distribution. Thus, reduced χ^2 values near 1 are indicative of a good fit.

4.3 Results and Discussion

4.3.1 SIMS imaging of homogenous surfaces

Because SIMS instruments collect data by counting occurrences, the counts in individual pixels follow a discrete probability distribution. The effect of this distribution is illustrated in Figure 4-1. A SIMS image of a single component Langmuir-Blodgett film made from palmitoyl-oleyl-phosphatidylcholine (POPC) is shown in Figure 4-1A. Figure 4-1B shows an intensity histogram plotted from the representative SIMS image that appears in 4-1A. On the x-axis, pixels are binned by the intensity or number of counts. The y-axis is the number of pixels at each intensity, normalized to the total number of pixels (N/N_{tot}). Displayed as an XY plot, the image (Figure 4-1A) appears to be a random array of intensities, and it is difficult to draw any conclusions about the nature of the analyzed surface. The black line represents the distribution predicted by the Poisson distribution using an average intensity calculated from the entire image. The theoretical curve fits the image distribution well, giving a reduced χ^2 value of 1.1. Thus, the intensity variations observed in Figure 4-1A are an artifact of counting statistics and the surface is homogenous, as would be expected given that the sample is a single component Langmuir-Blodgett film. These data also demonstrate that the Poisson distribution is an accurate model of the imaging data.

4.3.2 Probability mass functions and spatial resolution

The useful lateral resolution of a SIMS imaging experiment depends upon the focus of the primary ion beam as well as the useful ionization efficiency of the molecule of interest. However, because the image is compiled by counting rare events, one must consider that the pixel

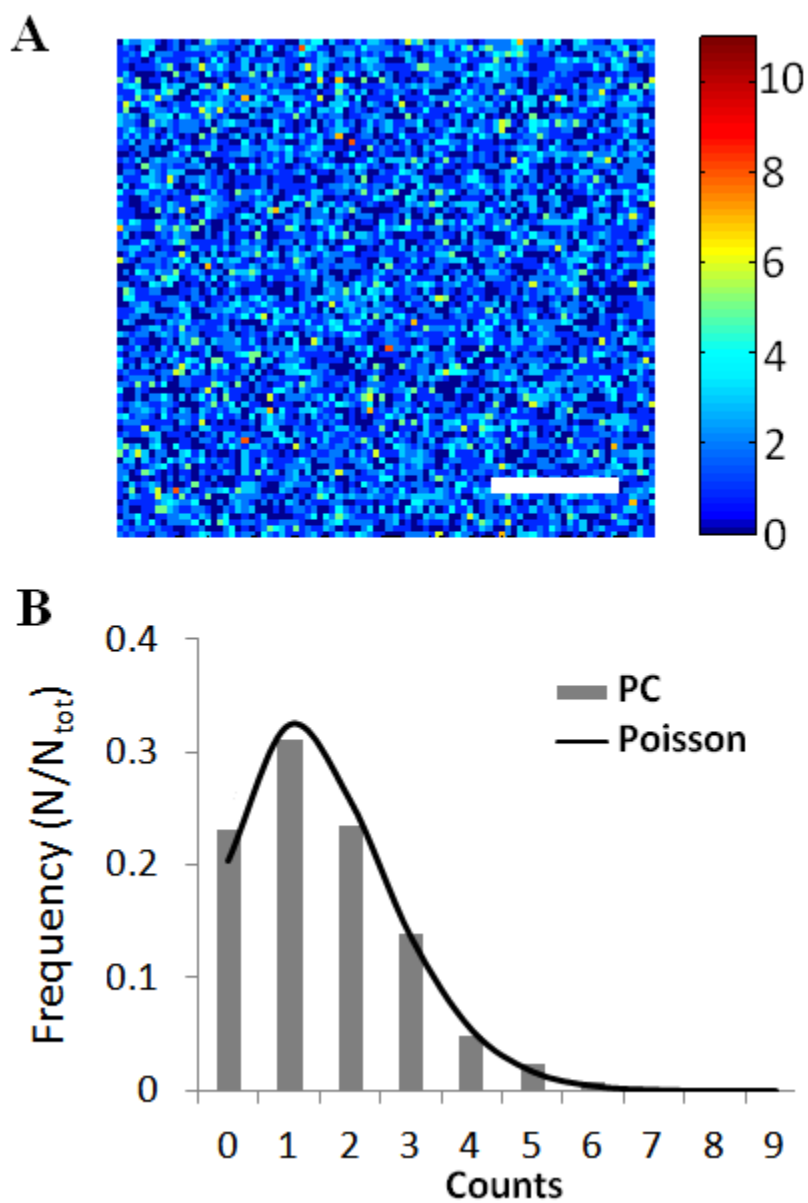


Figure 4-1. (A) Mass-specific image of PC from POPC LB film. (B) Histogram of signal intensity for $(m/z)^+ 184$ in a Langmuir Blodgett film composed of POPC. Scale bar represents 100 μm .

intensities will follow a probability distribution. The Poisson distribution is often used to characterize the statistics of rare events with a small average number of occurrences.²⁶ Adopting this as the model, the results of a proposed SIMS imaging measurement can be predicted, to better understand the effects of the intensity distribution, surface concentration, and ionization efficiency and how these parameters will affect the measurement.

In Figure 4-2, the model was applied to the theoretical imaging of cholesterol distribution in the plasma membrane of RBL-2H3 cells. The effective ionization efficiency was measured using a PVD cholesterol film imaged with an In^+ primary ion source. Although using In^+ primary ions results in lower ionization efficiencies when compared to cluster projectiles, the demonstrated compatibility with frozen sample preparations, ease of focus, and high ion currents that are routinely obtained make it useful for these experiments.

Previous work in the lab has demonstrated the m/z 147 can be used to identify cholesterol in the membrane of cryogenically preserved single cells, and offers a 3-fold increase in signal intensity, when compared to the molecular ion.²⁷ Due to the possibility of isobaric interference when using m/z 147, it is important ensure images are free of PDMS contamination. This was achieved by scanning the total image mass spectrum for the presence of other known PDMS contamination fragments.

For this calculation, two discrete surface concentrations of cholesterol were postulated. In concentration one, cholesterol comprises 25% of the membrane lipids, while in concentration two, cholesterol comprises 50% of membrane lipids, thus corresponding to a 100% concentration change. Using experimentally determined ionization efficiencies, and a pixel size of 310 nm, this would correspond to average pixel counts of approximately 0.6 and 1.2 for concentration one and concentration two, respectively. Figure 4-2A shows the expected intensity distributions calculated using these parameters. The resulting overlap of the distributions reveals that in an image containing these two populations, which differ in cholesterol concentration by a factor of

Probability Mass Functions

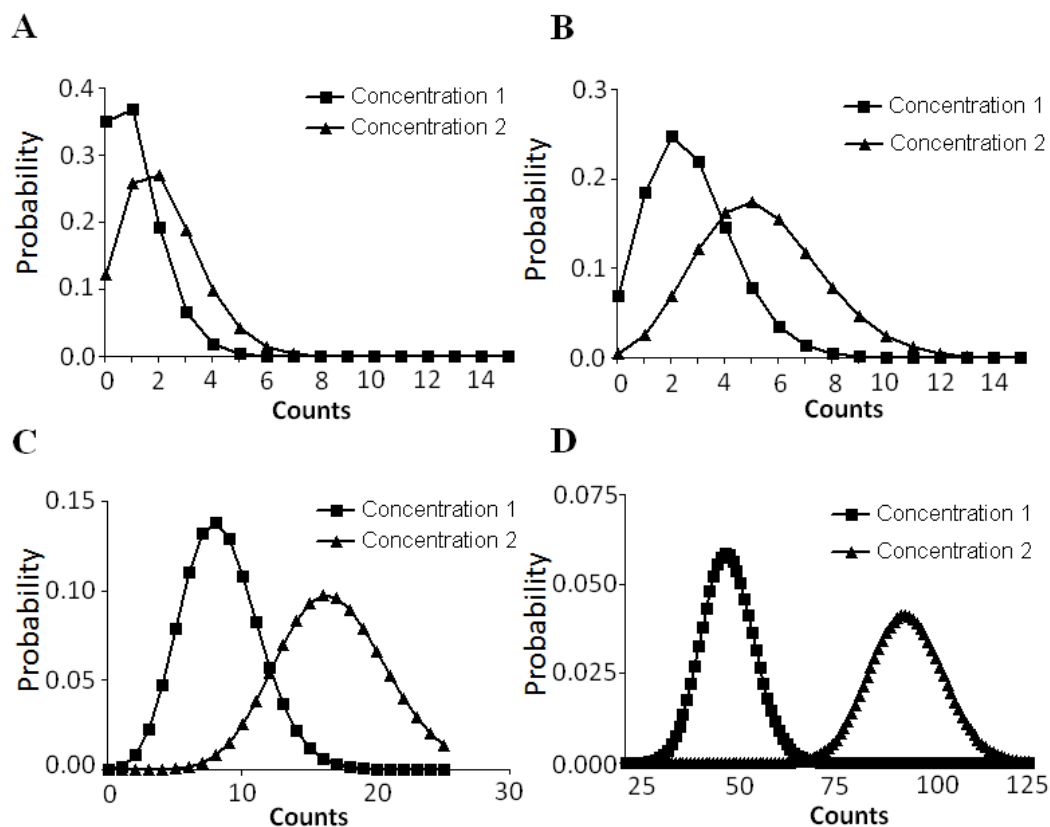


Figure 4-2. (A) Probability mass function for imaging cholesterol, assuming 100% concentration change between pixels, with 310 nm spatial resolution. (B) Probability mass function of two discrete populations where concentration 1 gives an average intensity of 2.67 counts and concentration 2 gives an average intensity of 5.33 counts. (C) Probability mass function for imaging cholesterol, assuming 100% concentration change between pixels, with 1.2 μm spatial resolution. (D) Probability mass function for imaging cholesterol, assuming 100% concentration change, down-binned to 2.79 μm spatial resolution.

two, the two concentrations will be virtually indistinguishable. This is expected because the average pixel intensity (N) is approximately 1, and N of 4, an average of 4 counts per pixel, is required for useful lateral resolution (*vide supra*). Increasing N to 4 for the calculations, and maintaining 100% concentration change, Figure 4-2B demonstrates that there is still considerable overlap. Extrapolation of this result to biological samples, which are infinitely more complex, suggests that spatial resolution estimates based on useful lateral resolution are misleading.

In Figure 4-2C, the spatial resolution of the data in Figure 4-2A has been down-binned from 310 nm to 1.2 μm by combining adjacent pixels, resulting in an N of 13.5. The plot shows that there is still an overlap in intensities. Counts in this overlap region can be differentiated with various levels of confidence; however, the majority of pixels can be identified with certainty. The degree of differentiation can be quantified using the z -score, as defined in Eq. 3 (Materials and Methods). For 1.2 μm spatial resolution, a z -score of 3 is calculated. From numerical integration, a z -score of 3 corresponds to 90% separation of the two distributions. A consequence of the standard deviation having a square root dependence on the mean intensity is that, regardless of how many counts are obtained, four times as many are needed to double the separation between populations. The by-product of this is illustrated in Figure 4-2D. To obtain complete separation of the two distributions, defined as being >99.5%, the image would have to be down-binned to 2.79 μm spatial resolution. This degree of separation gives a z -score of 5.6.

4.3.3 The effect of ionization efficiency and concentration change

The spatial resolution estimates reported in Figure 4-2 are instrument, mass, and matrix-dependent. Calculations were performed at a constant effective ionization efficiency and concentration change. Figure 4-3A shows the effect of the ionization efficiency of a species on spatial resolution. For this plot, the concentration change was again 100%, and the expected z -

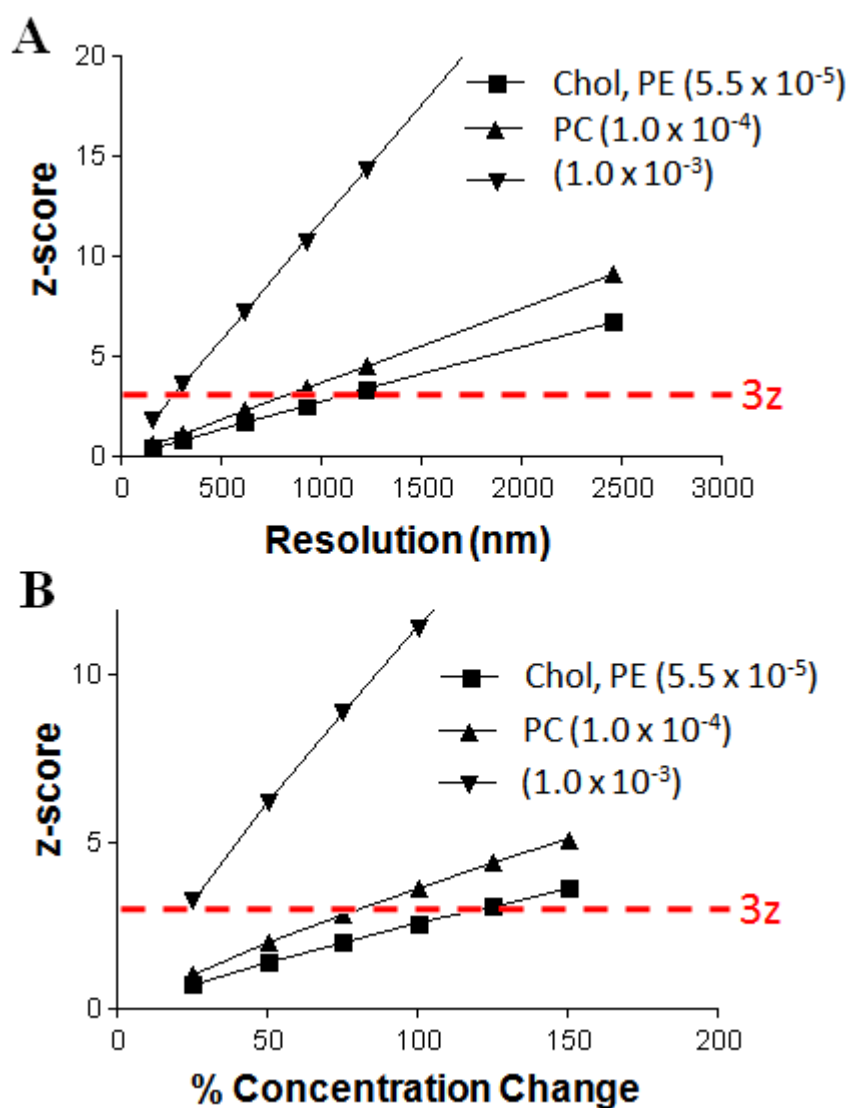


Figure 4-3. (A) z-score as a function of lateral resolution for various lipid ionization efficiencies. The change in concentration was held constant at 100%. (B) z-score as a function of change in lipid species concentration. For this plot, a spatial resolution of 1.2 μm was used, which corresponds to a z-score of 3, or 90% separation, for our cholesterol simulation. The numbers in the legends are ionization efficiencies.

score is plotted on the y-axis. The demonstrated dependence on ionization efficiency results in substantially different spatial resolutions attainable for different biomolecules. Thus, in a biological experiment where measurement of the native concentration change is desired, the best way to improve lateral resolution is through increased ionization efficiencies. Ionization efficiencies for cholesterol (5.5×10^{-5}), phosphoethanolamine (5.5×10^{-5}), and phosphocholine (1.0×10^{-4}) fragments were measured using In^+ as the primary ion source. Multiple reports in the literature i.e. utilizing cluster projectiles, MetA-SIMS, ME-SIMS, and combinations of these approaches have reported ionization efficiencies on the order of 1×10^{-3} , for a number of biomolecules.^{16, 17, 28-31} Figure 4-3A demonstrates that increasing ionization efficiency is promising for obtaining true submicron spatial resolution in biological experiments. Using a z-score of 3 to define a satisfactory confidence level and an ionization efficiency of 1×10^{-3} , we obtain a theoretical lateral resolution of 257 nm. In our experiment, the ionization efficiency limits the resolution to 1110 nm for cholesterol, and 811 nm for phosphocholine.

I then examined the z-score as a function of the change in concentration of the biomolecule, while keeping a constant spatial resolution of 1.2 μm . For this calculation, concentration one was held constant at 25% and concentration two was varied from 25 to 150%. It is important to note that a smaller value for concentration one results in lower spatial resolution, because it lowers the surface concentration of the molecule. This is important when considering biomolecules that are not major constituents of the sample. As one would expect, the z-score increases linearly with change in concentration. This plot further emphasizes the effect of ionization efficiency; a 20% concentration change can be accurately imaged with an ionization efficiency of 1×10^{-3} , compared with 120% and 83%, for 5.5×10^{-5} and 1.0×10^{-4} , respectively.

4.3.4 Using histograms to interpret imaging data

Although the distribution of counting data negatively impacts the spatial resolution attainable, the concept of plotting SIMS imaging data as a histogram can provide valuable information about a sample. The power of this analytical tool is demonstrated in Figure 4-4. Ternary Langmuir-Blodgett films have been used as model membranes for measuring lipid interactions.³² One such film made with 23% cholesterol, 47% sphingomyelin, and 30% POPC has been studied. The mass-specific image for cholesterol is shown in Figure 4-4A; Figure 4-4B contains a histogram of cholesterol intensities. Fitting the histogram with a Poisson distribution yields a reduced χ^2 value of 3.0, which suggests that multiple populations, or areas of different cholesterol concentration, are present on the surface. Indeed, the data can be fit to a model containing two distinct populations of cholesterol (Figure 4-4B, red trace, $R^2 = 0.96$). Mapping the pixels with intensities from 0-2, the image presented in Figure 4-4C is obtained. Figure 4-4D is the image from the map of pixel intensities 3-10. This demonstrates that analysis of the histogram allows us to better visualize and characterize domains that were previously identified via line scans,³³ giving us a complete image of the size and shape.

4.3.5 Single cell imaging of RBL-2H3 mast cells

One of the goals is to apply the unique capabilities of ToF-SIMS imaging to analyze the plasma membrane of single cells. These cells are 10–20 μm in diameter, and the membrane features under the experimental conditions used in the present work are submicron in size.³⁴ When imaging single cells, difficulties working with a small, finite sample volume are apparent. The analysis must be carried out in an ultra high vacuum environment, and thus great care must be exercised to preserve the arrangement of membrane components. This prerequisite precludes

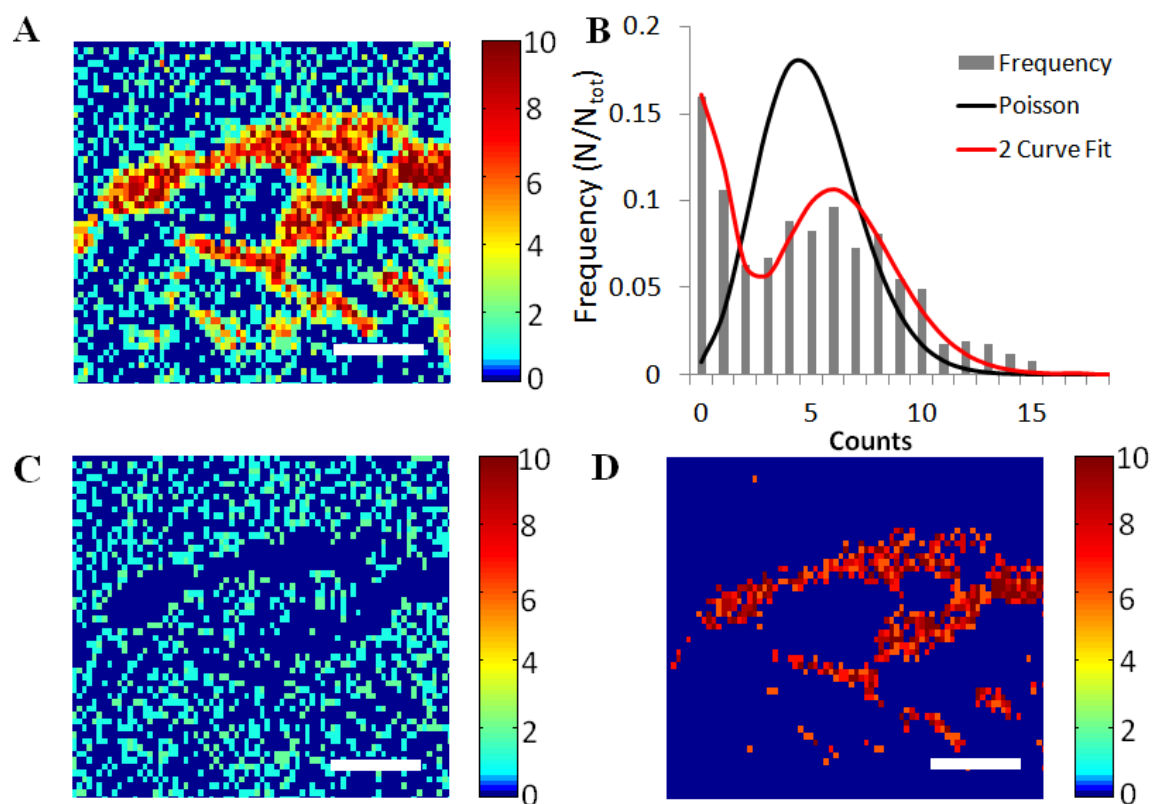


Figure 4-4. (A) Mass-specific image of cholesterol (m/z)⁺ 147 in the ternary mixture of PC, sphingomyelin, and cholesterol. (B) Histogram for signal intensity of cholesterol (m/z)⁺ 147 in a ternary mixture of PC, sphingomyelin, and cholesterol. The black line gives the predicted Poisson distribution using the average signal intensity. The red line gives the curve predicted by the Poisson distribution of the two populations shown in (C) and (D). (C) Map of pixels which have a cholesterol signal intensity of 0-2 counts, population 1. (D) Map of pixels which have a cholesterol signal intensity of 4-10 counts, population 2. Scale bars represent 100 μm .

the use of sample pretreatments (*vide supra*), to enhance ionization efficiency. To further complicate the analysis, the size of membrane features is on the scale of micrometers, and in many cases smaller. In addition, membrane components are commonly present in low concentrations on the surface. As a result, the data obtained from these experiments is often difficult to interpret. Thus, we applied our histogram analysis to identify possible populations, or domains, in the plasma membrane.

In Figure 4-5, four mass-specific ToF-SIMS images of a single RBL-2H3 cell are shown. The original images were collected using 310 nm pixels, as limited by the focus of the In⁺ primary ion source. The images have been down-binned to 1.2 μm pixels to increase the contrast obtained. For a 100% concentration change in cholesterol, this would correspond to a separation of 3 z. The masses mapped represent the phosphocholine headgroup (PC), cholesterol, the phosphoethanolamine headgroup (PE), and the phosphocholine headgroup plus part of the glycerol backbone (PPC). Phosphocholine containing lipids are the most abundant species in the mammalian cell membrane and they have the highest ionization efficiency, as evidenced in Figure 4-5A, by the far greater intensity and contrast seen in the PC image. Examination of this image gives information about the size and morphology of the cell. Given the inherent distribution of counting data, combined with varying ionization efficiencies and surface concentrations of the lipid, it is very difficult to draw any conclusions about the lipid species distribution from the images. The commonly used method for identifying heterogeneity, line scans, is problematic on this size scale because the effects of the intensity distribution dominate the generated line profile. To decrease the counting noise in a line scan, adjacent pixels are averaged resulting in a smooth profile. This approach is effective when analyzing domains much larger than a single pixel and having a characteristic location.^{2,3} However, this averaging obscures the information contained in single pixels and therefore decreases the spatial resolution. To identify smaller features, a new approach is needed.

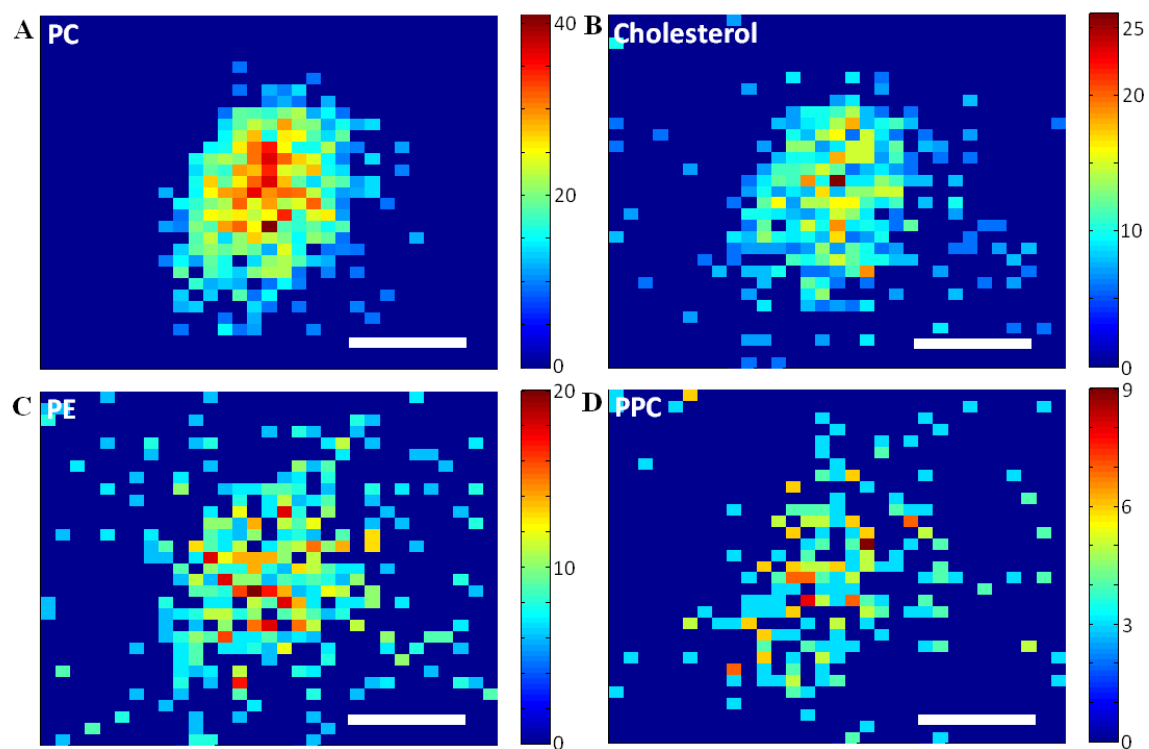


Figure 4-5. Mass-specific ToF-SIMS images of a RBL-2H3 mast cell. (A) PC (m/z)⁺ 184, (B) cholesterol (m/z)⁺ 147, (C) PE (m/z)⁺ 142, and (C) PPC (m/z)⁺ 224. Scale bars represent 10 μm .

4.3.6 Single cell histograms

To gain further insight into the lipid distribution intensity histograms for each of the species mapped were generated and these are shown in Figure 4-6. To do this, a region of interest was selected and the intensities for each pixel were then exported to statistical software. The boundary of the cell is derived from the boundary of the PC map for reasons specified above. Secondary ion micrographs (data not shown) confirm that RBL-2H3 cells present a flat surface to the analysis beam. To further minimize cell edge effects on the histogram, the outermost pixel around the cell perimeter was omitted. When analyzing cells that are not adherent and flat, further considerations will be required to account for the effect of cell morphology on secondary ion collection efficiency. The mean pixel intensity was again used to generate the theoretical curve predicted by the Poisson distribution to demonstrate the expected intensity distribution from a homogenous surface. Because each pixel is treated as an independent measurement, the histograms reported in Figure 4-6 have an n of 452.

It is apparent from the PC histogram that there is significant heterogeneity in the distribution of PC-containing lipid species across the surface of the cell. Reduced χ^2 analysis gives a value of 3.30, indicative of the poor fit. Due to the complexity of the PC histogram, interpreting the biological significance of this result is not possible at this time. Histograms of cholesterol and PE similarly suggest heterogeneous surface distributions of these species, with reduced χ^2 values of 1.95 and 1.81, respectively. The distribution of cholesterol intensities is discussed in further detail below. The fit for the PPC histogram, with a reduced χ^2 value of 1.39, suggests a more homogenous distribution. Because of the low average intensity of PPC, a z-score of <1 is expected for a 100% concentration change. Thus, large variations in concentrations could be concealed in this histogram and the result must be qualified in this manner. Table 4-1 displays the reduced χ^2 values for RBL-2H3 cell images shown in Figure 4-5, along with four

Table 4-1. Reduced χ^2 values for lipids imaged in RBL-2H3 Cells.

	Mast Cell 1	Mast Cell 2	Mast Cell 3	Mast Cell 4	Mast Cell 5	Average \pm SD
PC	3.30	2.18	2.19	2.35	2.30	2.46 \pm 0.47
Cholesterol	1.95	2.01	1.62	1.99	1.66	1.85 \pm 0.19
PE	1.81	1.94	1.73	1.63	1.71	1.76 \pm 0.12
PPC	1.39	1.71	1.35	1.30	1.49	1.45 \pm 0.16

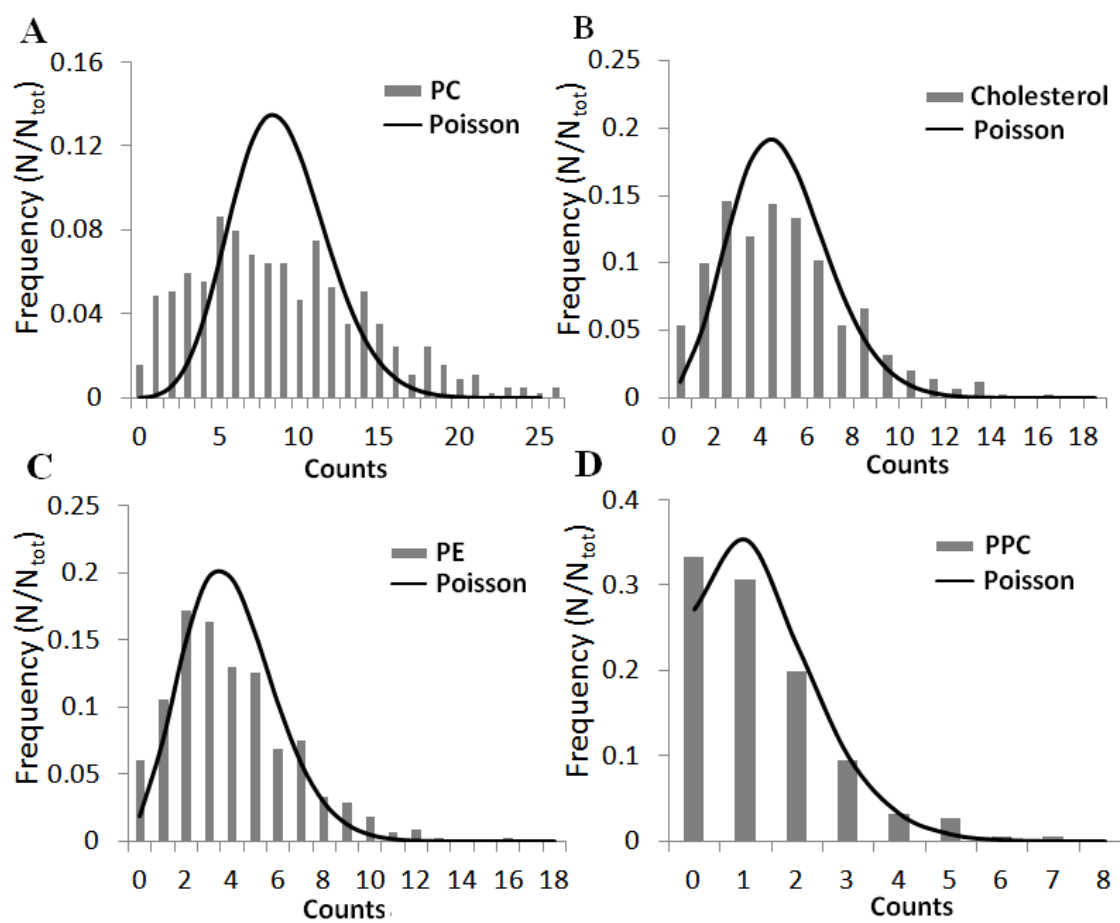


Figure 4-6. Histograms of the four lipid masses mapped in Figure 4-5. Histograms are the result of 452 pixels. The theoretical Poisson distribution, generated using the average pixel intensity, is overlaid in black. (A) $(m/z)^+$ 184, PC, (B) $(m/z)^+$ 147, CH, (C) $(m/z)^+$ 142, PE, and (D) $(m/z)^+$ 224, PPC.

other representative sets of RBL-2H3 cell images. The corresponding histograms for the cholesterol maps are presented in Figure 4-6.

4.3.7 Matrix effects in single cell plasma membrane imaging

When imaging with ToF-SIMS, it is necessary to consider the influence of matrix effects. It is imperative that the ionization efficiency of the analyte is constant across the surface of the cell to conclude that varying analyte concentration causes fluctuations in ion intensity. The cellular membrane is a tightly regulated, highly organized bilayer structure. The result is that lipids in a membrane consistently arrange themselves in the same orientation, perpendicular to the surface with hydrophilic moieties directed away from the interior. This leads to a repeating packing structure, which provides a consistent number of nearest neighbors with similar chemical properties.³⁵ Also the presence of membrane proteins on the cell surface, when averaged over the pixel area, must be assumed to be approximately constant. Given these two assumptions, lipids in the plasma membrane are found in similar chemical environments. Thus, if the membrane is well preserved with cryogenic sample preparation methods, it can be argued that matrix effects in all pixels across the surface, are equivalent.

To demonstrate this, the pixels that were in the top 10% of signal intensity for each of the four lipids mapped in Figure 4-5 were plotted in different colors, Figure 4-7A-D. The identity of each lipid mass is listed in the figure legend. This image demonstrates that these pixels are well distributed across the surface of the cell, regardless of the lipid moiety, thus validating the assumption that the ionization environment for lipids is relatively uniform across the cell. If the various lipid species ionization efficiencies were not constant across the cell surface, one would expect that high intensity pixels would appear as clusters on the surface. To further illustrate this lack of clustering, the four lipid masses are overlaid in Figure 4-7E. Pixels where overlap occurs

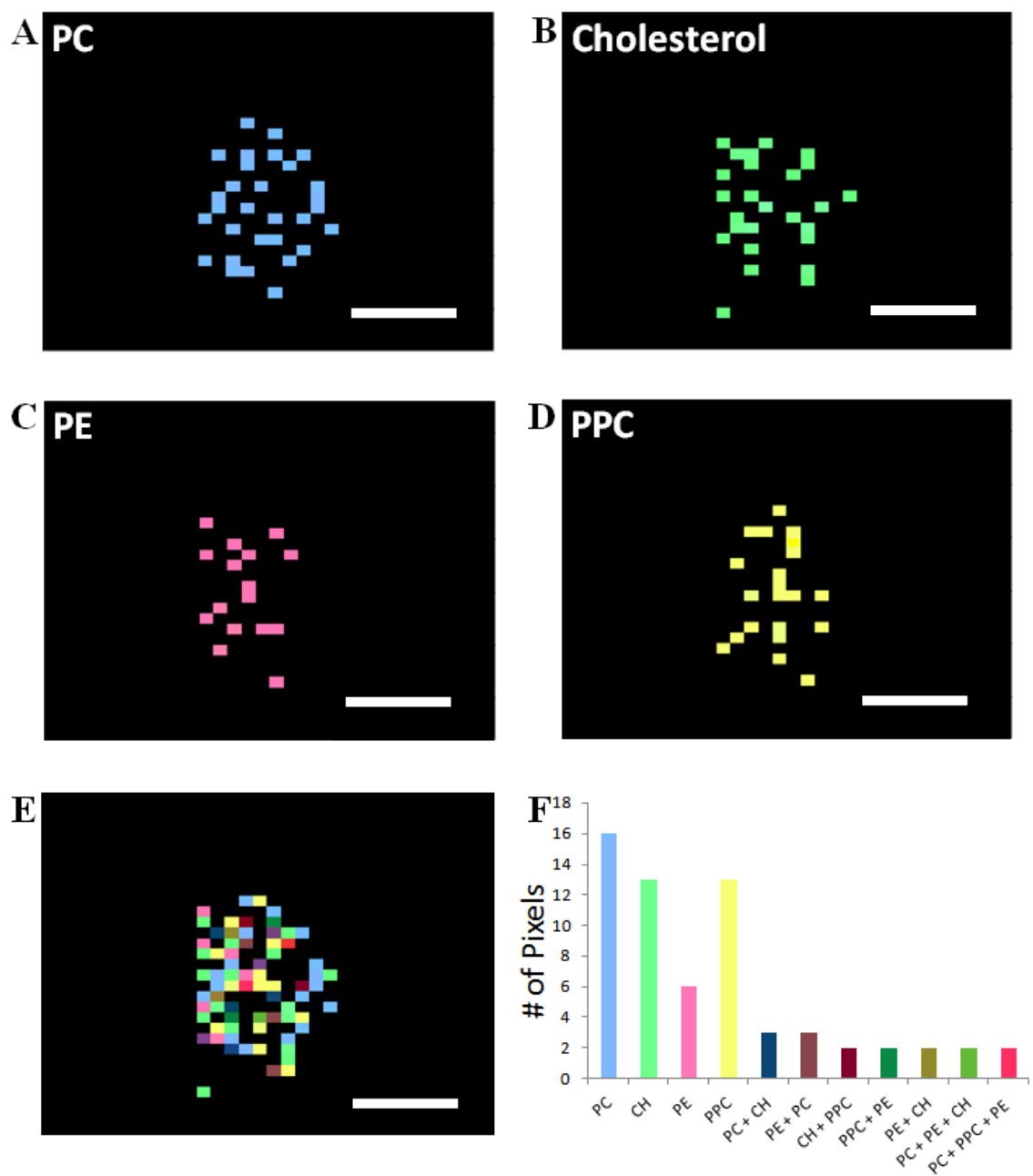


Figure 4-7. Pixels in the top 10% of signal intensity for (A) PC (m/z)⁺ 184, (B) Cholesterol (CH) (m/z)⁺ 147, (C) PE (m/z)⁺ 142, and (D) phospholipid only derived PC (m/z)⁺ 224. (E) Overlay of a-d. (F) Histogram of the coincidence of high intensity lipid signals. The extended color legend can be seen below the histogram. Scales bars represent 10 μ m.

are represented by new colors. The occurrence of overlap is then summarized with a histogram in Figure 4-7F. The identity of the colors is listed below the corresponding bar in the histogram. Figure 4-7F demonstrates that high intensity pixels most often occur exclusively, which also argues against the existence of ionization hotspots.

4.3.8 Distribution of cholesterol in RBL-2H3 mast cells

The histograms produced from cholesterol images suggest the presence of multiple populations or domains in the membrane. To extract more information from the histograms they were fit using multiple Poisson distributions. The mean and fractional surface contribution of the populations were allowed to vary to minimize error and produce the best fit. Figure 4-8A gives the resulting correlation coefficient as a function of molecular populations used. This plot demonstrates that the data are well described using three populations, and improvement in correlation coefficient is negligible when more curves are employed. This result is consistent for all five cholesterol images analyzed. Thus, the three-parameter model was adopted. An example of the three-curve fit is shown in Figure 4-8B. The three component curves are shown in Figure 4-8C, to give an idea of the relative contribution of each population. The results obtained for all the images, $n=5$, are summarized in Figure 4-8D. Examining the means from the fit curves reveals that population 1 has approximately half the cholesterol concentration of population one, and population three has twice the cholesterol concentration of population two (data not shown).

FRET and ESR studies indicate that as much as 65% of the cell surface may exist as cholesterol-rich domains in resting mast cells.³⁶ In addition, it is likely that nanoscopic segregation of these phases occurs in live cells.³⁷ Therefore it is important to describe the surface distribution of cholesterol in resting RBL-2H3 mast cells. The results shown in Figures 4-5, 4-6, and 4-8 as well as Table 4-1, demonstrate that heterogeneity in the lipid distribution of resting

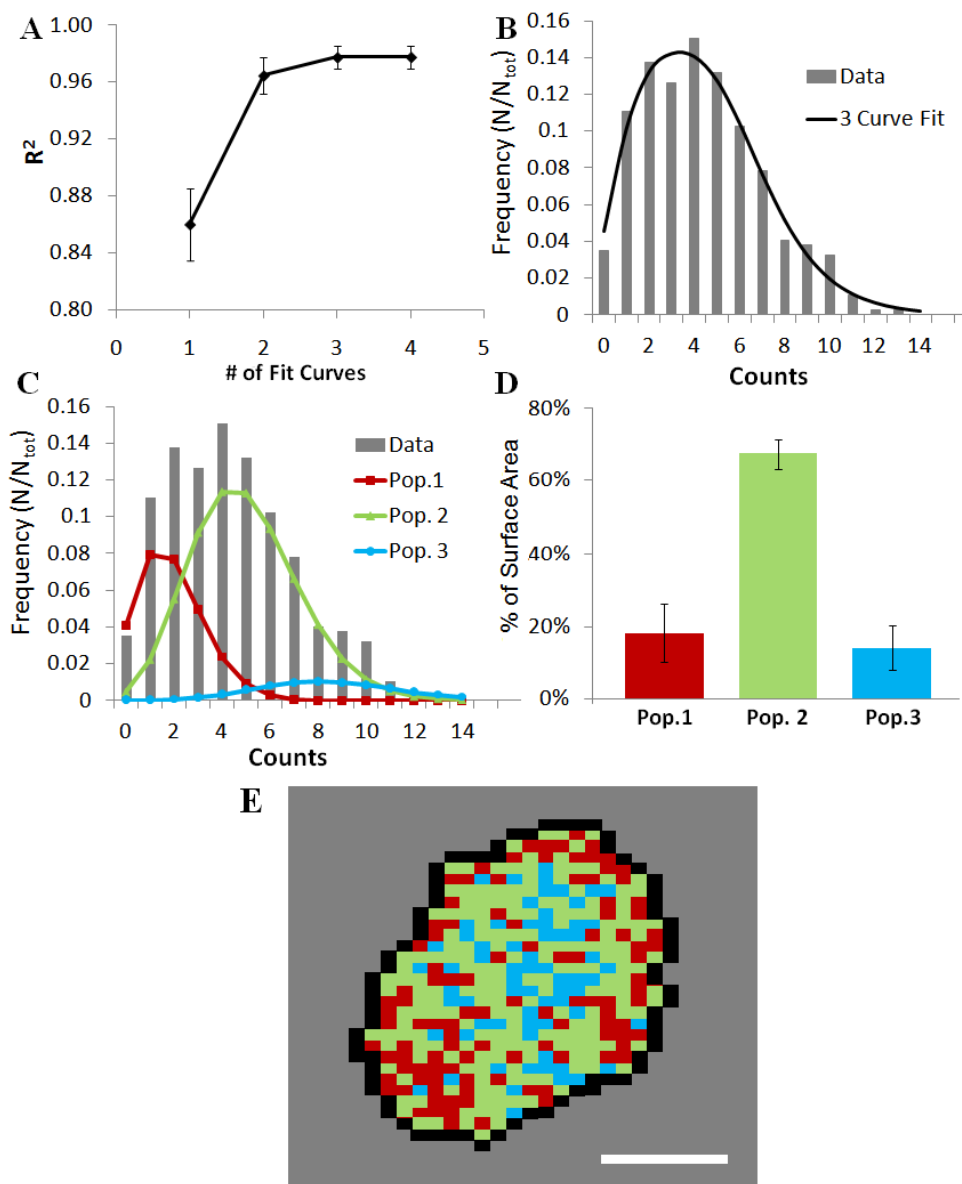


Figure 4-8. (A) A plot of correlation coefficient vs. number of weighted distributions used to fit cholesterol intensity distribution histograms. (B) Representative cholesterol histogram with 3 parameter fit shown in solid black, $R^2=0.98$. (C) The 3 curves that compose the 3 parameter fit shown in 6B. (D) Bar plot demonstrating the expected surface coverage for each cholesterol intensity population. (E) Reconstructed cell image displaying the locations of the three populations on the surface. Black outline corresponds to the boundary of the cell defined by the PC signal, which was used to generate the histogram. Color scheme for populations is conserved from (D). For this image, Population 1 is defined as pixels containing intensities 0-3, Population 2 is 4-7, Population 3 is 8-13. Scale bar is 10 μm . For (a) and (d), $n = 5$, and error bars denote standard deviations.

mast cells is observed by SIMS imaging. In the case of cholesterol, the evidence suggests that L_o domains exist on the cell surface, and even in the absence of cross-linking, heterogeneity in their surface distribution exists. A very important caveat related to the ToF-SIMS imaging results is that the RBL-2H3 cells were treated for 2 h at 4°C, which likely leads to quasi-phase separation that is cold-induced.^{38, 39} Indeed, plotting the pixels that correspond to each of the population intensities allows a map of these domains to be generated (Figure 4-8E). It is interesting to note that the higher intensities (population three) are central in the cell, the lowest (population one) seem to locate mostly around the outer parts of the cell, and the intermediate intensities (population two) are more spread out across the cell. This representation certainly appears to show heterogeneity based on the amount of cholesterol in specific domains of the membrane, a significant finding.

4.4 Conclusions

When interpreting SIMS images, it is essential to consider the intensity distribution of the molecular fragments. The distribution becomes increasingly important as the sample area becomes smaller and affects the attainable spatial resolution. The primary ion source spot size, the ionization efficiency of the analyte, the surface concentration, and the change in surface concentration to be measured are all important. Modeling can provide information about the feasibility of the experiment as well as the confidence level of the result. This approach uses a simple Poisson distribution to model the pixel intensity distributions obtained from SIMS imaging of homogenous surfaces. A more detailed representation of the surface is obtained by plotting the image intensity distributions as a histogram. Populations identified from histograms can be mapped to reveal unique distributions that are difficult to ascertain from the mass-specific images.

Plotting mass-specific images obtained from RBL-2H3 reveals that the lipid distribution on the plasma membrane is inhomogeneous. The evidence is especially strong in the case of PC-containing lipids. Although the nature and origin of these heterogeneities is presently unclear, SIMS imaging suggests the presence of substantial surface concentration differences in the plasma membrane. Histograms of cholesterol share the common characteristic of a small population of pixels exhibiting a two-fold increase in signal intensity. This provides direct evidence for the presence of cholesterol-rich domains on the cell surface.

4.5 References

- (1) Johansson, B. *Surf. Interface Anal.* **2006**, *38*, 1401-1412.
- (2) Ostrowski, S. G.; Bell, C. T. V.; Winograd, N.; Ewing, A. G. *Science* **2004**, *305*, 71-73.
- (3) Monroe, E. B.; Jurchen, J. C.; Lee, J.; Rubakhin, S. S.; Sweedler, J. V. *J. Am. Chem. Soc.* **2005**, *127*, 12152-12153.
- (4) Nygren, H.; Malmberg, P. *Trends Biotechnol.* **2007**, *25*, 499-504.
- (5) Altelaar, A. F. M.; van Minnen, J.; Jimenez, C. R.; Heeren, R. M. A.; Piersma, S. R. *Anal. Chem.* **2005**, *77*, 735-741.
- (6) Marxer, C. G.; Kraft, M. L.; Weber, P. K.; Hutcheon, I. D.; Boxer, S. G. *Biophys. J.* **2005**, *88*, 2965-2975.
- (7) Kraft, M. L.; Weber, P. K.; Longo, M. L.; Hutcheon, I. D.; Boxer, S. G. *Science* **2006**, *313*, 1948-1951.
- (8) Winograd, N. *Anal. Chem.* **2005**, 143A-149A.
- (9) Peteranderl, R.; Lechene, C. *J. Am. Soc. Mass Spectrom.* **2004**, *15*, 478-485.
- (10) Carado, A.; Passarelli, M. K.; Kozole, J.; Wingate, J. E.; Winograd, N.; Loboda, A. V. *Anal. Chem.* **2008**, *80*, 7921-7929.
- (11) Fletcher, J. S.; Rabbani, S.; Henderson, A.; Blenkinsopp, P.; Thompson, S. P.; Lockyer, N. P.; Vickerman, J. C. *Anal. Chem.* **2008**, *80*, 9058-9064.
- (12) Roddy, T. P.; Donald M. Cannon, J.; Meserole, C. A.; Winograd, N.; Ewing, A. G. *Anal. Chem.* **2002**, *74*, 4011-4019.
- (13) Roddy, T. P.; Donald M. Cannon, J.; Ostrowski, S. G.; Winograd, N.; Ewing, A. G. *Anal. Chem.* **2002**, *74*, 4020-4026.
- (14) Cannon, D. M. J.; Pacholski, M. L.; Winograd, N.; Ewing, A. G. *J. Am. Chem. Soc.* **2000**, *122*, 603-610.
- (15) Kotter, F.; Benninghoven, A. *App. Surf. Sci.* **1998**, *133*, 47-57.
- (16) Brunelle, A.; Touboul, D.; Laprevote, O. *J. Mass Spectrom.* **2005**, *40*, 985-999.
- (17) Prinz, C.; Hook, F.; Malm, J.; Sjoval, P. *Langmuir* **2007**, *23*, 8035-8041.
- (18) Keenan, M. R.; Kotula, P. G. *Surf. Interface Anal.* **2004**, *36*, 203-212.
- (19) Gidwani, A.; Holowka, D.; Baird, B. *Biochemistry* **2001**, *40*, 12422-12429.

- (20) Holowka, D.; Gosse, J. A.; Hammond, A. T.; Han, X. M.; Sengupta, P.; Smith, N. L.; Wagenknecht-Wiesner, A.; Wu, M.; Young, R. M.; Baird, B. *Biochim. Biophys. Acta, Mol. Cell Res.* **2005**, *1746*, 252-259.
- (21) Davey, A. M.; Heikal, A. A.; Sheets, E. D. 2007; Biophysical Society; 575A-575A.
- (22) Davey, A. M.; Walvick, R. P.; Liu, Y. X.; Heikal, A. A.; Sheets, E. D. *Biophys. J.* **2007**, *92*, 343-355.
- (23) Piehowski, P. D.; Kurczy, M. E.; Willingham, D.; Parry, S.; Heien, M. L.; Winograd, N.; Ewing, A. G. *Langmuir* **2008**, *24*, 7906-7911.
- (24) Vickerman, J. C.; Briggs, D., Eds. *ToF-SIMS: Surface Analysis by Mass Spectrometry*; IM Publications and Surface Spectra Limited: West Sussex, 2001.
- (25) Edidin, M. *Annu. Rev. Biophys. Biomol. Struct.* **2003**, *32*, 257-283.
- (26) Thompson, W. J. *Comput. Sci. Eng.* **2001**, *3*, 78-82.
- (27) Piehowski, P. D.; Carado, A. J.; Kurczy, M. E.; Ostrowski, S. G.; Heien, M. L.; Winograd, N.; Ewing, A. G. *Anal. Chem.* **2008**, *80*, 8662-8667.
- (28) Altelaar, A. F. M.; Klinkert, I.; Jalink, K.; deLange, R. P. J.; Adan, R. A. H.; Heeren, R. M. A.; Piersma, S. R. *Anal. Chem.* **2006**, 734-742.
- (29) McDonnell, L. A.; Heeren, R. M. A.; de Lange, R. P. J.; Fletcher, I. W. *J. Am. Soc. Mass Spectrom.* **2006**, *17*, 1195-1202.
- (30) Ostrowski, S. G.; Szakal, C.; Kozole, J.; Roddy, T. P.; Xu, J. Y.; Ewing, A. G.; Winograd, N. *Anal. Chem.* **2005**, *77*, 6190-6196.
- (31) Kozole, J.; Wucher, A.; Winograd, N. *Anal. Chem.* **2008**, *80*, 5293-5301.
- (32) McQuaw, C. M.; Zheng, L. L.; Ewing, A. G.; Winograd, N. *Langmuir* **2007**, *23*, 5645-5650.
- (33) Zheng, L.; McQuaw, C. M.; Ewing, A. G.; Winograd, N. *J. Am. Chem. Soc.* **2007**, *129*, 15730-+.
- (34) Davey, A. M.; Krise, K. M.; Sheets, E. D.; Heikal, A. A. *J. Biol. Chem.* **2008**, *283*, 7117-7127.
- (35) Gennis, R. B. *Biomembranes: Molecular Structure and Function*; Springer: New York, 1989.
- (36) Swamy, M. J.; Ciani, L.; Ge, M. T.; Smith, A. K.; Holowka, D.; Baird, B.; Freed, J. H. *Biophys. J.* **2006**, *90*, 4452-4465.
- (37) Sengupta, P.; Holowka, D.; Baird, B. *Biophys. J.* **2007**, *92*, 3564-3574.
- (38) Bali, R.; Savino, L.; Ramirez, D. A.; Tsvetkova, N. M.; Bagatolli, L.; Tablin, F.; Crowe, J. H.; Leiday, C. *Biochim. Biophys. Acta* **2009**.
- (39) Gousset, K.; Tsvetkova, N. M.; Crowe, J. H.; Tablin, F. *Biochim. Biophys. Acta* **2004**, *1660*, 7-15.

Chapter 5

Mass Spectrometry Imaging of Mating *Tetrahymena*: Changes in Cell Morphology Regulate Lipid Domain Formation

5.1 Introduction

During cellular function, the structure and the chemical composition of the cell membrane is continuously being modified via dynamic fusion and fission events with internal organelles.¹ The highly complex lipid composition of membranes plays a significant role in cell function by the construction of membrane features^{2,3} such as pores and lipid domains.⁴⁻⁷ It is not surprising that abnormalities in lipid composition and membrane function have been implicated in a myriad of disorders, ranging from neurological to cardiovascular.⁸⁻¹² Furthermore, an understanding of specialized membrane features and disease suggests a unique prospect for therapies that directly target lipid molecules and lipid domains.⁹

The *Tetrahymena* model of membrane fusion is ideal to study temporal changes in lipid dynamics related to lipid composition. Mating *Tetrahymena* fuse and then form hundreds of membrane pores between two mating cells. The pores expand, forming a membrane lattice with wide apertures, allowing cells to exchange micronuclei.¹³ The pores, 100-200 nm in diameter, require a curved localized membrane structure, which energetically favors certain lipids, excluding others.¹⁴ The mating process and pore formation can be synchronized such that the majority of the cells will be at the same mating step. Because the domain observed during mating forms without external manipulation, it is possible to determine whether changes in composition precede or follow changes in structure.

Mass spectrometry imaging has been used to observe lipid domains in conjugated single-cell organisms during mating.¹⁴ This discovery confirmed that the local composition of the

plasma membrane of living cells is intimately related to its localized structure but raised the important question: does the membrane lipid composition drive its structure or does the structure determine the membrane lipid composition? This is essentially a classic “chicken or the egg?” scenario. One possibility is that the membranes of these cells alter their lipid distribution and possibly their composition prior to fusion, thus anticipating the fusion event. The implication is that the lipid domains may help to drive fusion. Indeed, membrane fusion in *Tetrahymena thermophila* mating is dependent upon both lipid¹⁵ and protein¹⁶ synthesis. Conformational changes, which occur prior to fusion during a period called co-stimulation, have also been observed at the fusion site.¹⁶ The motivation to examine these cells at different stages of mating using mass spectrometry imaging was primed by these findings.

Two scenarios for the process by which lipid domains are formed are depicted in Figure 5-1. In this model, lysolipids of uncertain headgroup and hexagonal II (H II) lipids have been used to displace the cylindrical lipids, resulting in the observed lipid domain, which either precedes or follows pore formation. The bottom pathway represents domain formation preceding and preparing for membrane fusion. The upper pathway represents domains that are formed in response to the structural changes and fusion and pore formation.

Membrane pore formation involves significant bending of local membrane structure. The redistribution of lipid composition following membrane bending has been studied with model membranes. Homogenous, flat lipid monolayers were shown to form regions with heterogeneous lipid composition when bent, with the non-lamellar lipid concentrated in the areas of highest curvature.¹⁷ Additionally, phase separation of lipids can be induced by constructing a lipid bilayer on a curved surface.¹⁸ These phenomena are described by the theory of intrinsic curvature, which states lipid shape contributes to the spontaneous curvature of the membrane.¹⁹

In live cell experiments, degranulation of mast cells was inhibited when the contacting monolayers layers i.e. the outer leaflet of the vesicle and the inner leaflet of the plasma

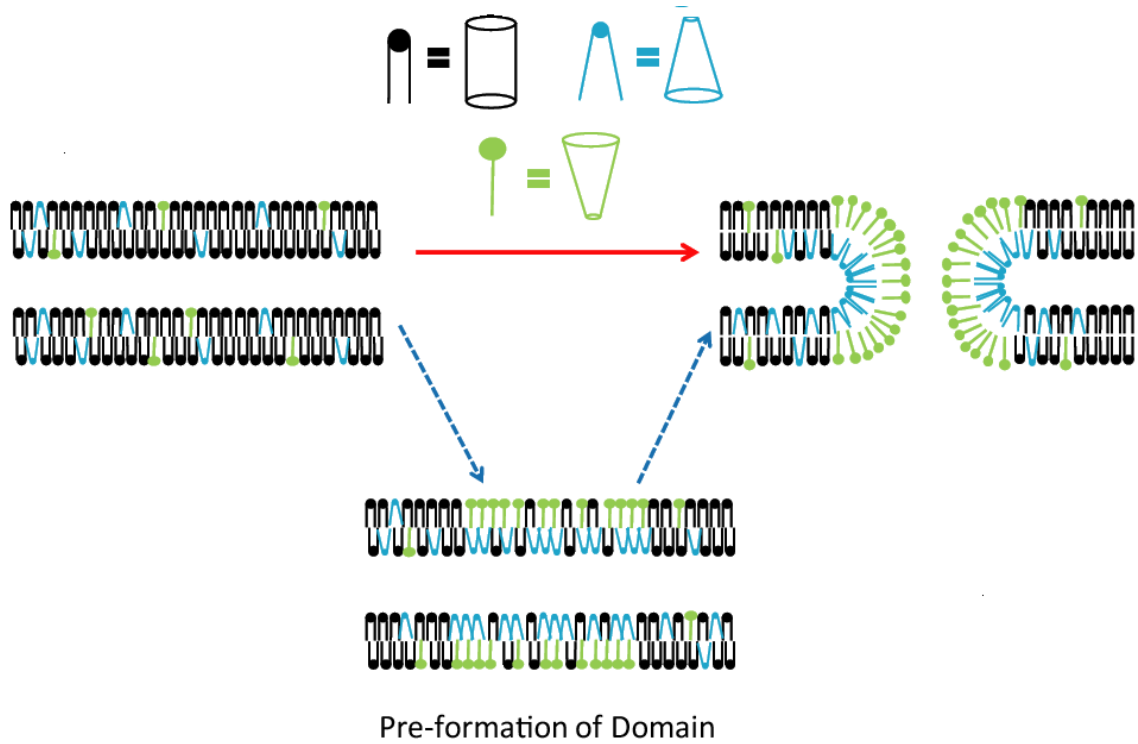


Figure 5-1. Schematic of two domain formation scenarios for mated *Tetrahymena thermophila*. Heterogeneously distributed lipids in the plasma membranes of *Tetrahymena thermophila* may form as a result of (red arrow) or in anticipation of pore formation (blue arrows). Black lipids are cylindrical, blue are H II and green are lysolipids.

membrane, were treated with lysophosphatidylcholine, a micelle-forming lipid (positive intrinsic curvature)²⁰, whereas incubation of isolated chromaffin granules with arachidonic acid (negative intrinsic curvature) promotes fusion.²¹ Amatore et al. recently showed that these lipids could each produce the opposite effect when added to the extracellular media (the non-contact side of the fusing membranes) of chromaffin cells.²² In a similar experiment PC12 cells were incubated with dipalmitoylphosphatidylcholine, a lamellar lipid (close to no intrinsic curvature), resulting in a decrease in the rate of exocytosis.²³ These studies unequivocally show the importance of non-lamellar lipids in the bending and fusion of lipid membranes. Experiments with model systems show that physical manipulation can be used to redistribute membrane composition and cell experiments show that altering composition can regulate the dynamics of the fusion event thus offering conflicting hypotheses; alteration of local lipid composition may be the cause or effect of altered membrane structure. Determining when the local composition changes relative to the fusion event could rectify this difference. In this chapter, mating *Tetrahymena* were examined with mass spectrometry imaging to determine if membrane fusion during the mating process creates lipid domains or if the cells have some mechanism, by anticipation of pore formation, to pre-form lipid domains.

This research effort was led by Michael Kurczyk. My role in the work was largely supportive: maintaining cell cultures, assistance with instrument maintenance and operation, discussions about data analysis, data interpretation, and manuscript preparation. My experience in this work formed the basis of my training in ToF-SIMS analysis of lipids in single cells, and insights from this work are underlying motivations for the rest of the work described in this thesis.

5.2 Material and Methods

5.2.1 Mating *Tetrahymena*

Tetrahymena thermophila strains B and CU428.1 were maintained at room temperature in 0.5% proteose peptone / 0.5% tryptone / 0.02% K_2HPO_4 / 0.01% crude soybean lecithin / 0.025% Fe-EDTA, and grown at 30 °C in 2% proteose peptone / 0.2% yeast extract / 0.5% dextrose / 0.01% crude soybean lecithin / 0.025% Fe-EDTA. Starvation was induced by centrifugation at 200 g for 4 min, washing with 10 mM HEPES adjusted to pH 7.3 with NaOH, and resuspension in HEPES at 30 °C with shaking. Cell densities were obtained by microscopic examination of samples fixed and diluted in phosphate-buffered formalin.

Cells starved for 16-20 hours were mixed to yield a 1:1 ratio of the two mating types at a density of approximately 10^6 cells/mL. Aliquots of 2 mL were distributed to wells of Falcon 353046 6-well plates maintained at 30 °C.

5.2.2 Trituration

One mL of cell suspension was removed from a 2 mL mating mix with a 1000 μ L Eppendorf micropipet and transferred to an empty well in a 6-well plate. The cells were drawn in and out of the pipet 5 times to disrupt loose pairs, then returned to the well. The result is 2 wells containing 1 mL of cell suspension; one that has been triturated and one that has not. One mL of 2.4% glutaraldehyde in 0.2M sodium phosphate buffer, pH 7.0 was then added to both the triturated and undisturbed mating mixes.

5.2.3 Cell Counting

Cells were counted at several time points over a 4-h period during mating: 0 min, 30 min, then every 15 min until 210 min, and 240 min. Aliquots were taken from the mating cell suspension and fixed in a formalin solution to terminate the mating process. This was done twice for each time step. One aliquot was triturated while the control cells were left undisturbed until fixation. Single and paired cells were counted and the percent of cells paired was determined. A minimum of 300 fixed cells was examined as described by Van Bell and Williams.²⁴ The percent of paired cells resistant to trituration was determined by dividing the percent of paired control cells by the percent of paired cells following trituration.

5.2.4 SIMS imaging

Cells were prepared for analysis in vacuum using a freeze fracture procedure for SIMS imaging described previously.²⁵ Cells were imaged at 3 times; 1, 2, and 3 h following mixing of the two mating types. SIMS imaging was carried out using Kratos Prism ToF-SIMS spectrometer (Manchester, U.K.) equipped with a 15-kV FEI (Beaverton, OR) indium liquid metal ion source (LMIS). The LMIS was focused to a beam size of approximately 500 nm and delivered 1 nA of current to the sample at 45°. The sample was mounted onto a LN₂-cooled analysis stage (Kore Tech. Ltd, Cambridge, U.K.).

SIMS imaging was performed by electrostatically raster-scanning the primary ion beam across the sample and collecting a mass spectrum at every pixel in the 128 x 128 pixel image. Molecular ion images were generated by selecting a mass of interest from the total ion mass spectrum and plotting the intensity at each pixel. Image processing, including a two-dimensional smooth and signal thresholding were done in MATLAB (MathWorks, Inc., Novi, MI).

5.2.5 Region of interest analysis

Mass Spectra from regions of interest (ROI) on the SIMS image were generated using a program written in house using Labview 7(National instruments, Austin, TX). The mass spectra for each individual pixel were down binned to one nominal mass, and the pixels were selected from each ROI and summed to produce a mass spectrum.

5.2.6 Line scans and intensity calculation

Using in-house software, line scans, which plot signal intensity variations for a particular mass across the SIMS image, were used to measure the percent decrease of PC in the junction region of a given cell pair. Line scans were acquired across the junction producing a graph of the intensity of m/z 184 with respect to lateral distance across the two cell bodies and the junction. A graph displaying local minima at the junction was determined to have a lipid domain.

PC intensities were calculated from line scans for each cell (Cell body I & II) and the junction, coupling them for each time point examined. Line scans were normalized to the maximum and the cell bodies were identified by local maxima. The signal intensity was determined by averaging the points at and above 90 % of the local maximum. The signal in the junction was determined by averaging data within 10 % of the local minimum as an analysis interval. When no local minima were found, analysis regions were chosen to correspond to cell bodies and junctions observed with microscopy. The average signal decrease between the two cell bodies and the junction was calculated as previously described.¹⁴

5.3 Results and Discussion

5.3.1 Lipid domain formation correlates to pore formation

To investigate when the lipid domain forms relative to fusion, time-of-flight secondary ion mass spectrometry (ToF-SIMS) imaging was used. Previously established ToF-SIMS imaging with freeze fracture sample preparation as a method to track lipid domain formation were employed.¹⁴ Furthermore, images of the phosphocholine (PC) ion (m/z 184), indicative of the lamellar lipids phosphatidylcholine and sphingomyelin, serve as a diagnostic tool to identify *Tetrahymena* mating domains; the PC signal decreases in the area where the two cells have fused.¹⁴ This is the only technique currently known to provide the chemical specificity and submicron lateral resolution required to directly visualize such domains.^{6, 26} In ToF-SIMS, the secondary ions are accelerated into a time-of-flight mass spectrometer, separating them by their mass-to-charge ratio and detecting them. An image is constructed by collecting mass spectra as a function of the position of the primary ion beam as it is raster-scanned across the surface. A mass spectrum is collected at each pixel, spatially revealing the chemical composition of the surface.

In order to establish the link between pore and lipid domain formation in mated *Tetrahymena thermophila*, it was important to identify the point at which stable pores had been formed between the two cells. Cell pairs can be described as being either strongly or weakly bound. The distinction is that strongly paired cells resist separation which can be brought about by physical perturbation or the addition of exogenous agents to the media.^{16, 24, 27} This resistance to separation is taken to be evidence for the formation of stable pores.²⁸ Here physical perturbation called trituration is used to discriminate strongly and weakly paired cells.²⁷

A differential interference contrast (DIC) image of paired cells is shown in Figure 5-2A and freeze fractured SIMS images of a trituated mated pair are shown in Figure 5-2B. The

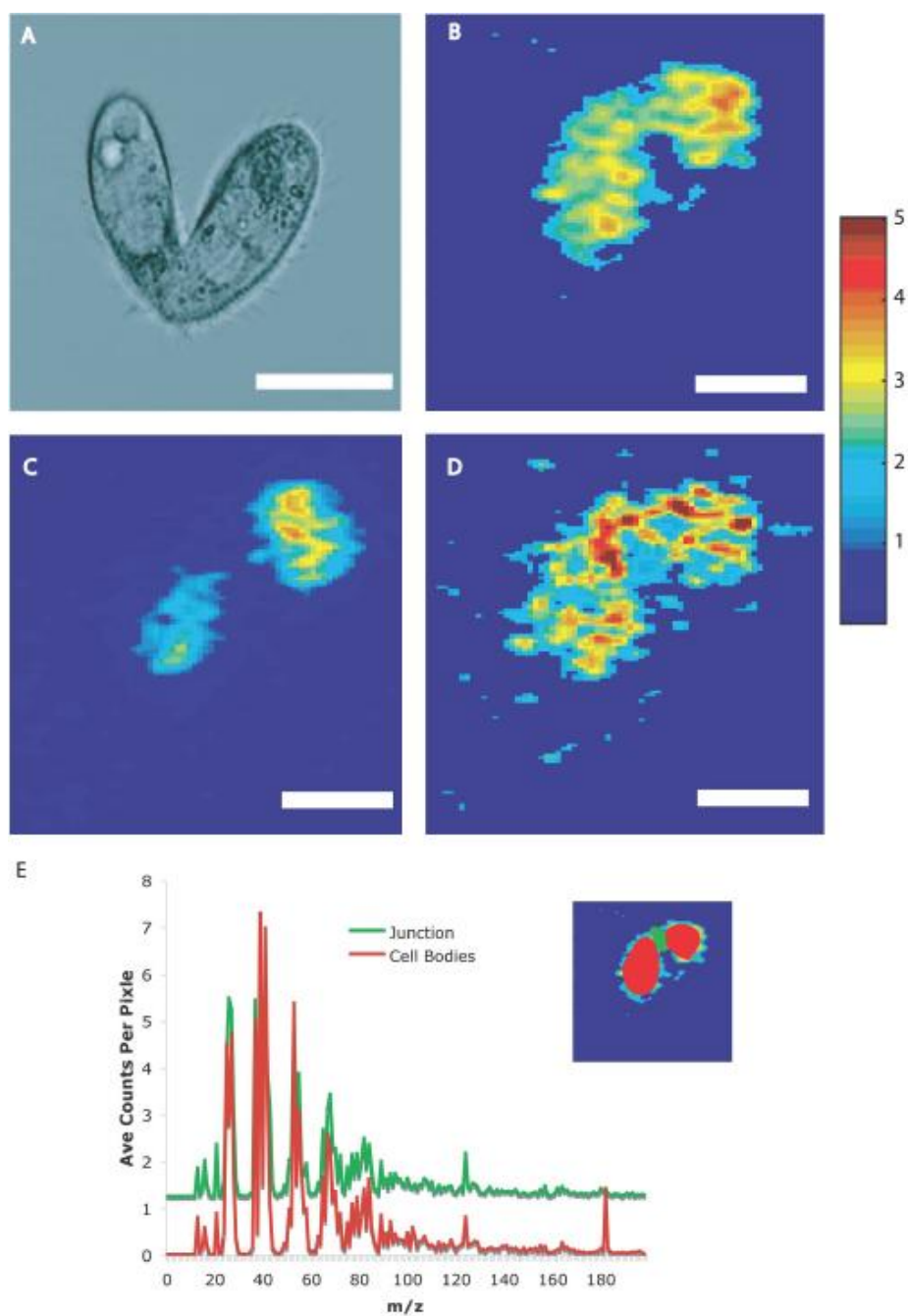


Figure 5-2. Sims analysis of a strongly paired mated *Tetrahymena thermophila*. (A) Differential interference contrast microscopy image of a mating cell pair (scale bar = 25 μ m). (B-D) SIMS images of a triturated pair of mating *Tetrahymena thermophilla*. C5H9 is mapped in B PC is mapped in C and 2-AEP is mapped in D the intensity in the 2-AEP image has been multiplied by 3. (E) Region of interest analysis of the same cells. The red mass spectrum is from the cell bodies and the green mass spectrum is from the junction. The inset highlights the regions on the SIMS image, red for the cell bodies and green for the junction. Data collected by Mike Kurczy.

image in panel B maps $C_5H_9^+$ (m/z 69), a hydrocarbon fragment ubiquitous to the acyl chains found in phospholipids.^{6, 29, 30} This chemical image shows that the membranes of the two cells are in contact because the signal is continuous through the junction. In fact, the membranes are fused, as evidenced by the cells' resistance to separation following trituration. The ion image also serves to as an internal standard, which is used to compare ion signals from other molecules from the membrane surface.^{6, 29, 30} The C_5H_9 signal is fairly consistent throughout the junction, thus fluctuations in lipid signal were taken to reflect changes in concentration across the membrane surface. The image in Figure 5-2C maps the surface concentration of PC. The most dramatic feature in this image is the lack of signal in the junction of the two cells. This is the previously reported lipid domain¹⁴, however, here using trituration it is confirmed that pores have formed between the two cells and that they correlate to the appearance of the lipid domain. The SIMS image in Figure 5-2D maps m/z 126 the headgroup and diagnostic ion used to identify 2-aminoethylphosphonolipid(2-AEP).¹⁴ This nonlamellar lipid does not decrease in the junction region like the PC ion. To the contrary the 2-AEP signal appears relatively intense in the region lacking the lamellar lipids. Mass spectra taken from two regions of interest, the cell-cell junction and the cell bodies, are shown in Figure 5-2E. The spectra confirm that the PC signal is decreased in the junction relative to the cell bodies, and that the concentration of 2-AEP remains consistent through the regions.

Trituration has been used here to isolate paired cells with pores, but it cannot be used to directly isolate weakly paired cells with no pores, because the procedure separates these cells. No lipid heterogeneity was observed in single cells when imaged with ToF-SIMS (data not shown), however to investigate weakly paired cells mating *Tetrahymena* cells had to be analyzed under quiescent conditions. The time scale for pair formation vs. pore formation was determined so that aliquots of weakly paired cells could be extracted, frozen, freeze fractured, and analyzed.

5.3.2 Trituration determines time scale for strong pair formation

Mating in *Tetrahymena* lasts several hours and can be synchronized such that the total population of cells will advance through the process at roughly the same rate. Cells will only initiate pairing in the presence of complementary mating types hence time zero is defined as the point when the two cell types are mixed. To determine the time scale of domain formation, rapid freezing was used to arrest the mating process, followed by ToF SIMS analysis. Cells were frozen for analysis at several time points, the lipids in the membrane measured and correlated to pair formation and ultimately membrane fusion. Cells were examined at 1 hour (loosely paired cells), 2 hours (loose/strong pair intermediates), and 3 hours (strongly paired cells). The time points for analysis were experimentally chosen by tracking the rate of pair formation and the rate of strong pair formation by comparing the number of cells that pair under quiescent conditions to the number of cells paired following trituration (Figure 5.3A). Most cell pairs were formed during the initial hour of mating. These pairs were determined to be weakly bound because at the same time point under trituration conditions no pairs were observed. The transition from loosely paired to mated cells occurred from 90 to 150 min with 50 % mated at 120 min following the initiation of the experiment. The plot obtained from the trituration experiment was used to determine the time points when aliquots of the mating cells suspension would be extracted and frozen. SIMS experiments were carried out on cells that had not been trituated.

5.3.3 Mass spectrometry imaging shows that weakly bound cells do not display lipid domains

Initial studies with ToF SIMS imaging of mating *Tetrahymena* were carried out on mated cells, demonstrating lipid domains. In that work, cells were analyzed later in the process (several hours) and exhibited distinct lipid domains.¹⁴ In the first step following formation of cell pairs,

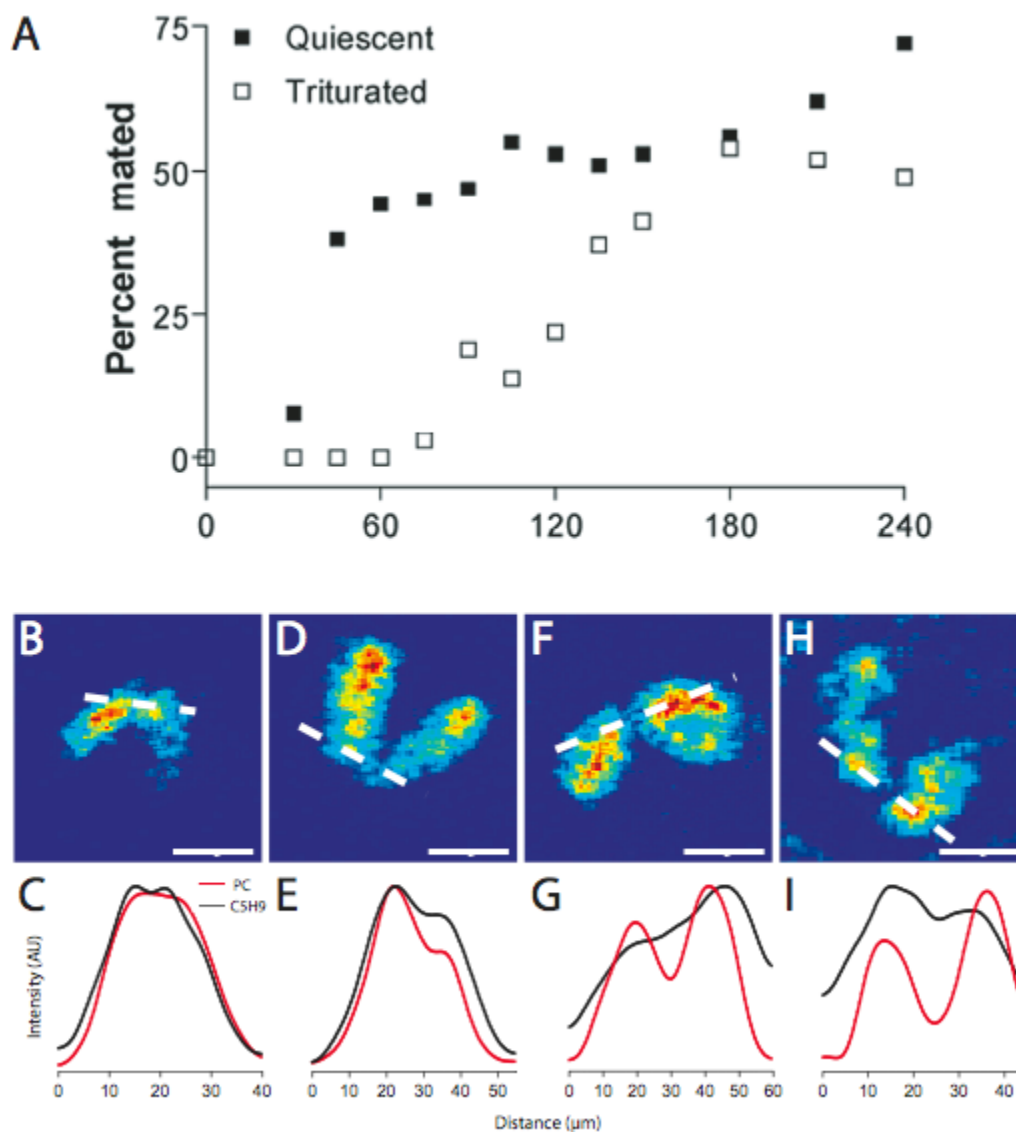


Figure 5-3. Temporal evolution of the observed lipid domain formed during cell conjugation. (A) The percent cells paired plotted over time under quiescent conditions and the percent of cells paired following trituration. (B-I) SIMS images and line scans of mated *Tetrahymena thermophilla* at three time points following the initiation of mating. The molecular fragment ion images of PC (m/z 184) for cell pairs imaged at (B) 1 hour, (D and F) 2 hours and (H) at 3 hours. (C, E, G, I) The corresponding line scans for PC and the m/z 69 intensity (ubiquitous hydrocarbon fragment C_5H_9) as control¹⁴. Each time point taken across the junction is shown below each image. Line scans were treated with 25 % Savitzky-Golay smoothing. Data collected by Mike Kurczy.

all the loosely bound pairs analyzed, with the exception of one, did not display a lipid domain in the ToF SIMS images (Figure 5-3B). Weakly adhered cell pairs are known to be disrupted following treatment with concanavalin A, a plant lectin with affinity for glycoproteins on the cell surface²⁷, suggesting that this initial pairing is dictated by a protein interaction before pores are formed. Image pixel intensity was averaged and plotted against distance across the cell-to-cell junction to provide line scans. A line scan for the image of loosely paired cells is shown in Figure 5-3C, and indicates the absence of a domain. A fraction of cell pairs imaged at two hours were observed to possess a lipid domain at the junction (Figure 5-3D and G). An example of a PC molecular fragment ion image for a cell pair that had no domain at two hours is shown in Figure 5-3D, while another example shown in Figure 5-3F had a clear lipid domain. This was confirmed by line scans across the images (Figure 5-3E and G). All cells imaged at the three-hour time point exhibited domains (Figure 5-3H and I).

5.3.4 Domains become more prominent over time

Average changes in PC in the cell-pair junctions are presented in Table 5-1. The amount of PC in the junction of mated *Tetrahymena* significantly decreases as cells are mated for longer times (one-way ANOVA, $p < 0.01$). It is hypothesized that the evolution of the observed lipid domain depends on changes in the superstructure of the membrane at the cell-cell junction i.e. pore formation, which requires non-lamellar lipids for stability. Additionally, it has been proposed that following initial formation, pores broaden and form a mesh of lipid microtubules.³¹ Assuming this mechanism for domain formation, the table also suggests that rate of these structural changes increases over time. The table shows that between one and two hours PC decreases by almost 20% and by 40% between two and three hours. The observed rate increase may be due to membrane reorganization caused by the initial events making the membranes more

Table 5-1. Summary of relative PC intensities across mating *Tetrahymena thermophila*

Time	Cell Body I	Junction	Cell Body II	Percent Decrease
One Hour (n= 6)	0.81 ± 0.15	0.74 ± 0.10	0.86 ± 0.11	9 % ± 9
Two Hours(n= 9)	0.80 ± 0.14	0.58 ± 0.12	0.86 ± 0.12	28 % ± 16
Three Hours (n= 4)	0.81 ± 0.15	0.23 ± 0.11	0.74 ± 0.22	68 % ± 17

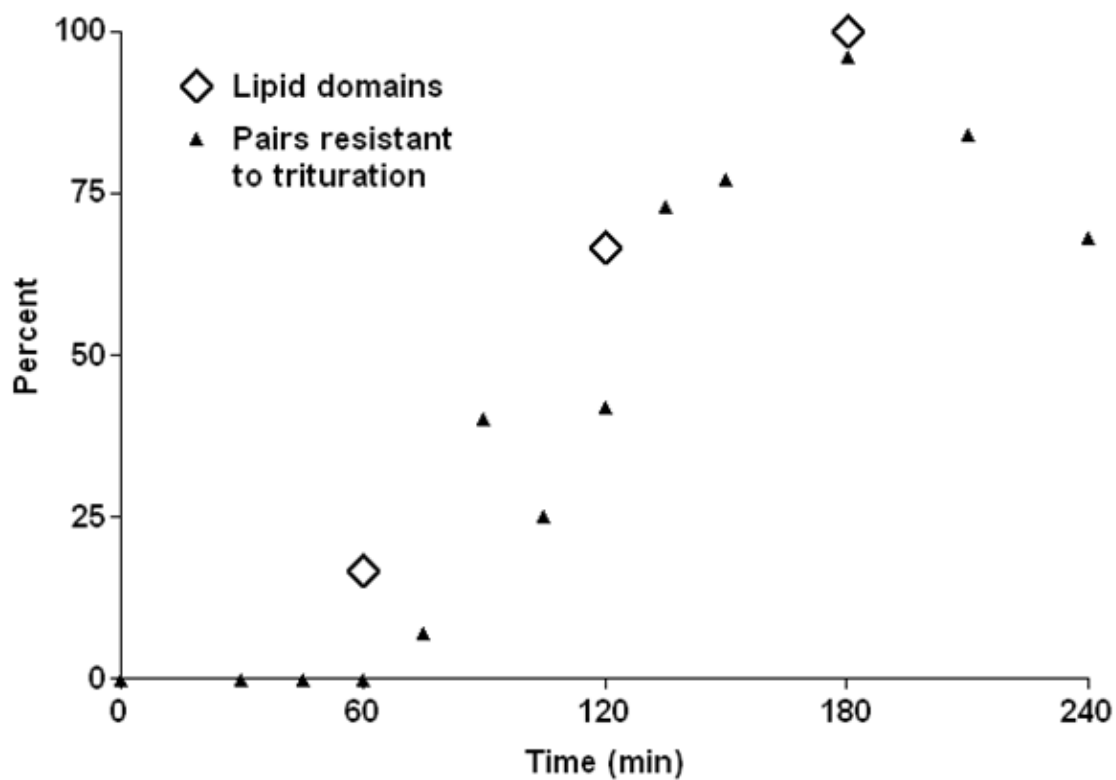


Figure 5-4. The percent of paired cells displaying lipid domains over time vs. the percent of paired cells that resisted separation following trituration. Three time points were investigated 60 min (n= 6), 120 min (n= 9), and 180 min (n= 4). Domains were defined as a decrease in phosphocholine at the junction between cells¹⁴. Line scans of PC intensity were used to measure this decrease. The appearance of a trough was used to determine that a pair had formed a lipid domain. Data collected by Mike Kurczy and Craig Van Bell.

amenable to fusion. This is consistent with the results from the living cell experiments discussed above.

5.3.5 Domain formation correlates to trituration resistance

The correlation between lipid domain formation and the strength of cell pairing (response to trituration) was analyzed. Cell pairs that did not display a significant trough in the line scan (less than 20 % signal decrease in the junction) were defined as not containing lipid domains. The percent of cells displaying domains at each time point is compared to the percent of cells resisting trituration in Figure 5-4. The pairs analyzed which did not show lipid domains were all from either the one or the two-hour time point. Indeed, one-third of the pairs analyzed at the intermediate time of two hours did not display lipid domains. The appearance of lipid domains correlated well to the resistance of pairs to separate following trituration. Apparently the formation of lipid domains in the cell pairs identifies the threshold from which cell mating cannot be easily disrupted.

5.4 Conclusion

Lipid domains observed in mated *Tetrahymena* are not observed in single cells prior to mating nor are they observed in significant numbers in loosely paired cells at early times. Hence, the hypothesis that lipid domain formation precedes strong pairing of cells is excluded. Moreover, domains do not form until the cells have become strongly paired and begin to form pores. Presumably the PC concentration decreases to make the spontaneous curvature of the contacting layers negative but this is not a precondition for fusion. It has been shown that the fusion protein synaptotagmin can induce membrane curvature³²; a similar mechanism could be at

work here. Protein-induced membrane deformation and pore formation may alter the local membrane composition. As the pores develop and increase in number, more high curvature lipid is recruited to the junction displacing PC. This produces the observed time-dependent decrease in PC at the junction. Therefore, the important conclusion from mass spectrometry images of mating *Tetrahymena* is that pore formation drives the formation of lipid domains. Thus, the physical structure needed to support a function dictates composition at this level.

Dynamic membrane processes are ubiquitous in cell biology. The mechanism by which the cellular machinery constructs highly curved membrane structures is therefore highly important. Two hypotheses can be envisioned (see Figure 5-1). First, the cell machinery might actively segregate non-lamellar lipids, which would reduce the energy barrier for membrane fusion, or second, mechanical bending of the membrane would favor lipid rearrangement to minimize energy of the pore structure. The composition of the cell membrane is continuously being modified via fusion and fission events. Whether structure dictates composition or the opposite is important in determining regulating factors. It has recently been observed that incubation with lipids can alter the rate of exocytosis.^{22, 23} If indeed structure dictates the chemical composition of membranes, then it is convenient to speculate that membrane fusion events result in a subsequent change in local membrane composition. This in turn would lead to plasticity in the process. This could serve numerous functions, and may be part of the basis of short-term memory.

5.5 References

- (1) Chernomordik, L. V.; Zimmerberg, J.; Kozlov, M. M. *J. Cell Biol.* **2006**, *175*, 201-207.
- (2) Blumenthal, R.; Clague, M. J.; Durell, S. R.; Epand, R. M. *Chem. Rev.* **2003**, *103*, 53-69.
- (3) Yang, L.; Huang, H. W. *Science* **2002**, *297*, 1877-1879.
- (4) Edidin, M. *Trends Cell Biol.* **2001**, *11*, 492-496.

- (5) Hao, M. M.; Mukherjee, S.; Maxfield, F. R. *Proc. Natl. Acad. Sci. U. S. A.* **2001**, *98*, 13072-13077.
- (6) Ostrowski, S. G.; Bell, C. T. V.; Winograd, N.; Ewing, A. G. *Science* **2004**, *305*, 71-73.
- (7) Simons, K.; Ikonen, E. *Nature* **1997**, *387*, 569-572.
- (8) Cutler, R. G.; Kelly, J.; Storie, K.; Pedersen, W. A.; Tammara, A.; Hatanpaa, K.; Troncoso, J. C.; Mattson, M. P. *Proc. Natl. Acad. Sci. U. S. A.* **2004**, *101*, 2070-2075.
- (9) Escriba, P. V. *Chem. Phys. Lipids* **2006**, *143*, 45-45.
- (10) Mattson, M. P.; Cutler, R. G.; Pedersen, W. A. *J. Neurochem.* **2002**, *81*, 60-60.
- (11) Maxfield, F. *Nature* **2005**, *438*, 612-621.
- (12) Scherzer, C. R.; Feany, M. B. *Trends Genet.* **2004**, *20*, 273-277.
- (13) Orias, J. D.; Hamilton, E. P.; Orias, E. *Science* **1983**, *222*, 181-184.
- (14) Ostrowski, S. G.; Van Bell, C. T.; Winograd, N.; Ewing, A. G. *Science* **2004**, *305*, 71-73.
- (15) Frisch, A.; Loyter, A.; Levy, R.; Goldberg, I. *Biochim. Biophys. Acta* **1978**, *506*, 18-29.
- (16) Wolfe, J. *Journal of Morphology* **1982**, *172*, 159-178.
- (17) Ding, L.; Weiss, T. M.; Fragneto, G.; Liu, W. H.; Yang, L.; Huang, H. W. *Langmuir* **2005**, *21*, 203-210.
- (18) Parthasarathy, R.; Yu, C. H.; Groves, J. T. *Langmuir* **2006**, *22*, 5095-5099.
- (19) Gruner, S. M. *Proc. Natl. Acad. Sci. U. S. A.* **1985**, *82*, 3665-3669.
- (20) Chernomordik, L. V.; Vogel, S. S.; Sokoloff, A.; Onaran, H. O.; Leikina, E. A.; Zimmerberg, J. *Febs Letters* **1993**, *318*, 71-76.
- (21) Creutz, C. E. *J Cell Biol* **1981**, *91*, 247-256.
- (22) Amatore, C.; Arbault, S.; Bouret, Y.; Guille, M.; Lemaitre, F.; Verchier, Y. *ChemBioChem* **2006**, *7*, 1998-2003.
- (23) Uchiyama, Y.; Maxson, M. M.; Sawada, T.; Nakano, A.; Ewing, A. G. *Brain Res.* **2007**, *1151*, 46-54.
- (24) Vanbell, C. T.; Williams, N. E. *J. Protozool.* **1984**, *31*, 112-116.
- (25) Cannon, D. M.; Pacholski, M. L.; Winograd, N.; Ewing, A. G. *J. Am. Chem. Soc.* **2000**, *122*, 603-610.
- (26) Kraft, M. L.; Weber, P. K.; Longo, M. L.; Hutcheon, I. D.; Boxer, S. G. *Science* **2006**, *313*, 1948-1951.
- (27) Ofer, L.; Levkovitz, H.; Loyter, A. *J Cell Biol* **1976**, *70*, 287-293.
- (28) Allewell, N. M.; Oles, J.; Wolfe, J. *Exp. Cell Res.* **1976**, *97*, 394-405.
- (29) Monroe, E. B.; Jurchen, J. C.; Lee, J.; Rubakhin, S. S.; Sweedler, J. V. *J. Am. Chem. Soc.* **2005**, *127*, 12152-12153.
- (30) Ostrowski, S. G.; Kurczy, M. E.; Roddy, T. P.; Winograd, N.; Ewing, A. G. *Anal. Chem.* **2007**, *79*, 3554-3560.
- (31) Frantisek Baluska; Dieter Volkmann; Barlow, P. W. *Cell-Cell Channels*; Landes Bioscience: Georgetown, TX, 2006.
- (32) Martens, S.; Kozlov, M. M.; McMahan, H. T. *Science* **2007**, *316*, 1205-1208.

Chapter 6

Cluster Bombardment to Recover Spatial Chemistry after Preparation of Biological Samples for SIMS Imaging

6.1 Introduction

Imaging time of flight secondary ion mass spectrometry (ToF-SIMS) is an emerging bioanalytical tool that allows molecular-specific images of biological samples to be acquired with their native chemistry intact, at submicron resolution, and without employing labels. However, the preparation of biological samples remains a limiting step in applying the technique to answering specific biological questions, since ToF-SIMS imaging is carried out under ultra high vacuum conditions.¹⁻¹⁰ Numerous methods have been developed to make biological samples more amiable to the vacuum environment, including freeze-drying with various rinses^{1, 11, 12}, metal imprinting¹⁰, metal deposition¹, freeze-etching⁷, freeze-fracture^{8, 13}, and vitrification.⁶ These methods have proven to be useful but all have shortcomings, the most limiting being reproducibility.

Ultimately, a SIMS experiment should yield an information-rich image, composed of intense signals corresponding to the ions of interest, with sub-micron spatial resolution. Sample preparation techniques are likely to damage the surface of the sample to some degree, resulting in the attenuation of relevant ion signals and degrading analyte localization. Under optimal experimental conditions these effects are minimal, and useful spatial and chemical information is extracted. Optimization of the sample preparation can be problematic for tissues and cells because of inherent sample-to-sample variation. Identical procedures can produce sample surfaces with varying degrees of damage and thus varied secondary ion yield and localization. However, if the damage is confined to the surface of the sample, this interfering layer can be

removed and the underlying, undamaged material analyzed. It will then be possible to acquire the chemical information from the undamaged layer, easing the restrictions on sample preparation.

Surface bombardment using cluster ion projectiles has the unique ability to remove molecular material with minimal damage accumulation to the underlying layers when compared to atomic projectiles.^{14,15} Also, these projectiles do not significantly redistribute material from one layer to the next. This approach has been successfully applied for several applications including molecular depth profiling^{16,17} and 3-D imaging¹¹, but has not yet been used as a supplemental sample preparation method.

In this chapter, the unique properties of cluster ion projectiles are utilized to increase the reproducibility of current sample preparation methods for biological SIMS imaging. The surface specificity of SIMS makes it possible for important information to be obscured by a matrix overlayer or by a layer of damaged material at the surface. The approach presented here demonstrates that it is possible to uncover spatio-chemical information from below the sample surface, thus overcoming some common artifacts caused by sample preparation.

The analysis of mouse embryos described in this chapter was done by Michael Kurczyk. It is included here to demonstrate an application derived and supported by the model system experiments described in the first half of the chapter.

6.2 Materials and Methods

6.2.1 C_{60}^+ SIMS

SIMS data was acquired using a BioToF ToF-SIMS spectrometer, described in detail elsewhere.¹⁸ The spectrometer was equipped with a 40 KeV C_{60}^+ primary ion source¹⁹⁻²¹

(Ionoptika Ltd., Southampton, U.K.). The source was operated with a 300 μm diameter beam defining aperture, yielding approximately 20 pA of DC current.

6.2.2 Preparation of cholesterol films

Physical vapor deposition (PVD) films were prepared by subliming cholesterol (Sigma-Aldrich, St. Louis, MO) contained in a crucible by resistive heating of a tungsten filament followed by deposition onto a LN_2 -cooled sample stage. The film thickness was monitored using a quartz crystal microbalance (QCM), and subsequently characterized using AFM. Films used for this study had a thickness of $100 \text{ nm} \pm 10 \text{ nm}$. To create patterns, a Cu Finder Grid (Ted Pella, CA) was affixed to the silicon substrate prior to cholesterol deposition. After the deposition, the grid was carefully removed to create a cholesterol relief on the silicon substrate.

6.2.3 Preparation of mouse embryo slices

Axial slices from 14 day old mouse embryos were excised as previously described.²² Tissue slices were either rinsed in 18 M Ω water or incubated in a 100 μM solution of cholesterol- β -cyclodextrin (CDT, Inc., High Springs, FL) for 30 min prior to rinsing. After rinsing, the tissue samples were applied to 5 mm x 5 mm Si Substrates (Ted Pella, CA) and plunge frozen in LN_2 . Samples were stored under LN_2 until being entered into the analysis chamber of the mass spectrometer at LN_2 temperature. The temperature of the sample was raised to $-80 \text{ }^\circ\text{C}$ to remove excess water on the surface.

6.3 Results and Discussion

6.3.1 Modeling water deposition in biological analysis

In the presence of atmospheric water, frozen hydrated samples accumulate an ice layer on the top of the surface to be analyzed. Likewise, freeze-fractured samples can be completely covered in ice due to the unpredictability of the position in the fracture plane.⁹ This ice may not damage the surface; however, it is a layer of material that masks the chemical information below the ice. Controlled removal of this layer will greatly increase the reproducibility of these two sample preparation methods.

To examine the usefulness of C_{60}^+ for removing a water layer from a sample without damaging the underlying chemical structure, a simulated biological sample was created by using physical vapor deposition (PVD). Briefly, a SEM finder grid was placed on a silicon substrate and cholesterol vapor was allowed to condense on the surface. After deposition the grid was removed, leaving behind a relief pattern of cholesterol with known spatial dimensions. A schematic of the patterned cholesterol films is shown in Figure 6-1. The sample was then transferred to the mass spectrometer for analysis. A 3D schematic of the patterned film surface is shown in Figure 6-2A. The sample was then cooled to LN₂ temperature for 1 h, which allowed water from the vacuum environment to condense on the surface forming an ice overlayer, Figure 6-2B. After collecting a SIMS image, the ice layer was removed using a C_{60}^+ impact with a sputter dose of $6 \times 10^{12} C_{60}^+/\text{cm}^2$, Figure 6-2C. From the measured sputter yield of amorphous ice for a 40 keV C_{60}^+ ($4000 \text{ H}_2\text{O}/C_{60}^+$) and the molecular density ($3.075 \times 10^{22} \text{ molecules}/\text{cm}^3$) it was calculated that $\leq 8 \text{ nm}$ of ice was removed from the surface. After removal an image larger than the sputter area was acquired, Figure 6-2D.

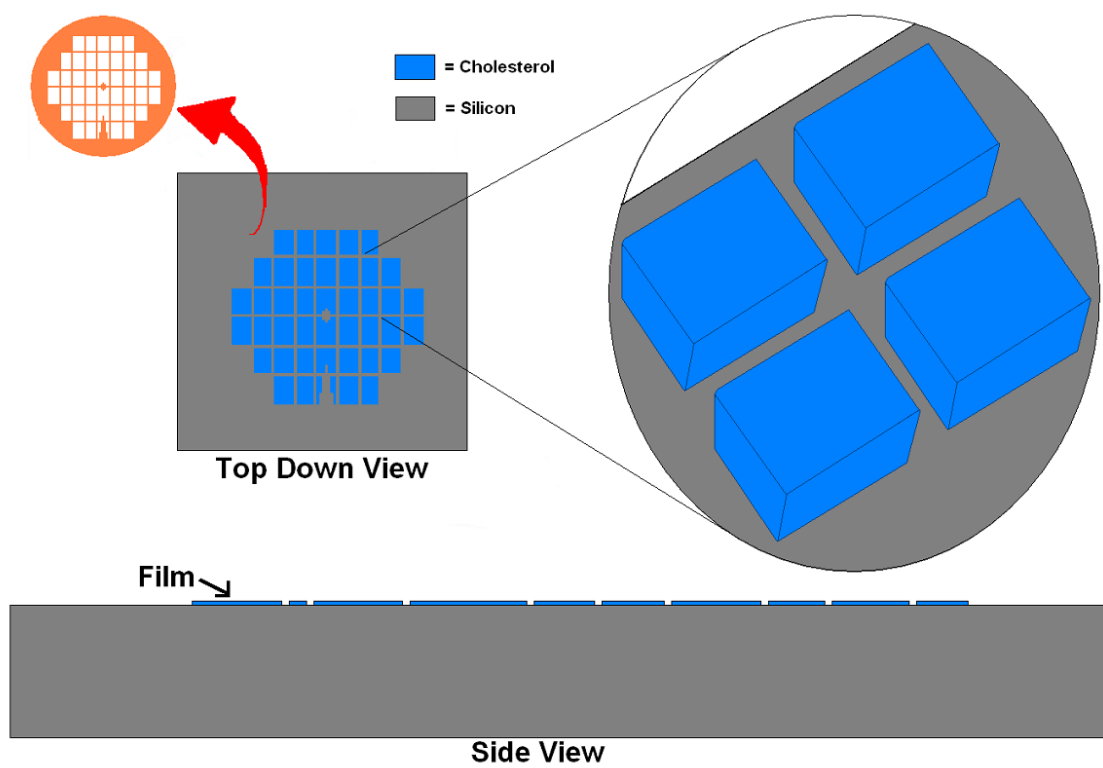


Figure 6-1. A cartoon diagram of physical vapor deposited patterned cholesterol film.

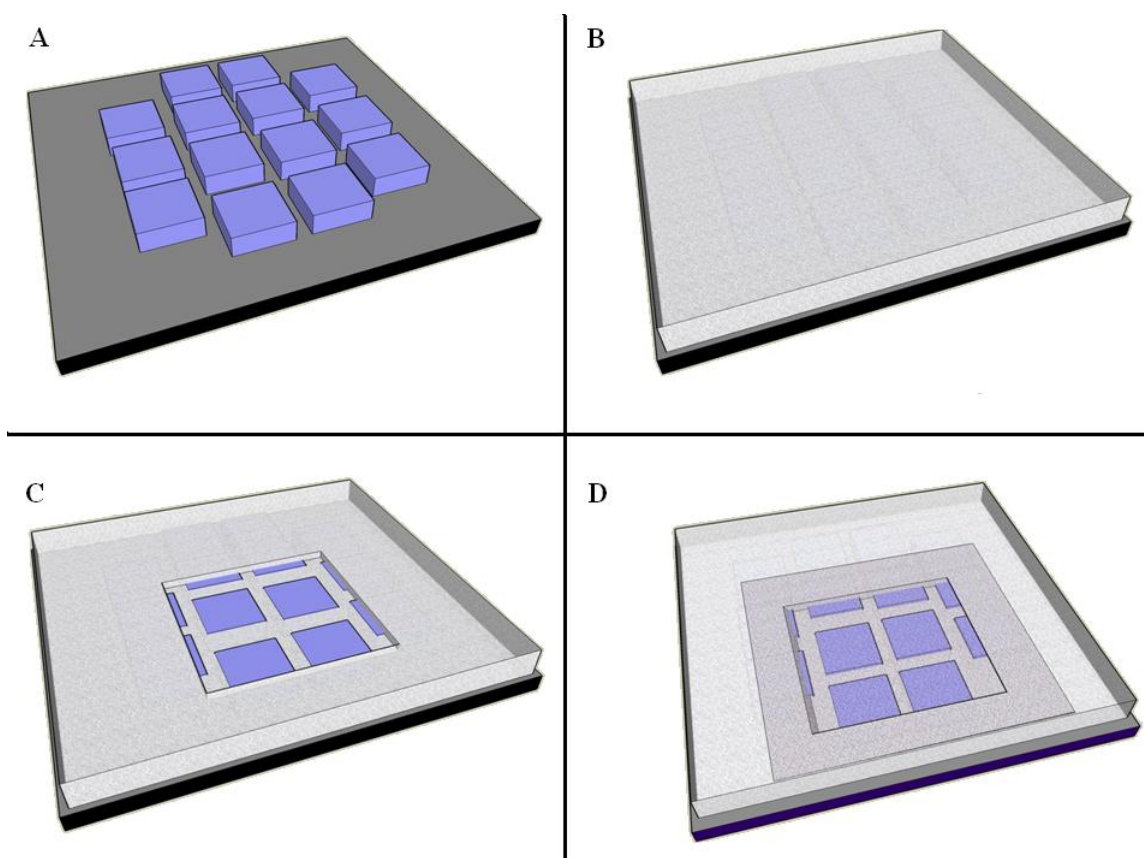


Figure 6-2. (A) 3D schematic of patterned cholesterol film. (B) 3D schematic of patterned cholesterol film that has been covered by deposited water. (C) 3D schematic of patterned cholesterol film after deposition and subsequent removal of water. (D) 3D schematic of patterned cholesterol film illustrating imaging area after deposition and removal of water.

A SIMS image overlay of a patterned cholesterol film on a Si substrate is shown in Figure 6-3A prior to ice deposition. Here the patterned cholesterol islands are visible; Si is mapped in red and cholesterol is mapped in green. The second panel (Figure 6-3B) contains an image overlay following ice deposition; water is mapped in blue and cholesterol in green. The grid pattern has been covered by the ice and cannot be resolved. The ejection of cholesterol ions has been prevented by the ice layer. Following sputter removal, the grid pattern can once again be resolved and it is possible to detect molecular ion signals (Figure 6-3C). The intensity of line scans for cholesterol taken across one of the grid lines in the patterned film before water deposition and after water deposition with subsequent removal is shown in Figure 6-3D. These data demonstrate that there is minimal loss of lateral resolution following the removal of the ice over layer. In fact, the interface between cholesterol pillars and the silicon substrate appears sharper after the water deposition and subsequent sputtering. This effect is likely due to removal of the cholesterol molecules that were redistributed across the Si surface as a result of the sample preparation and transfer.

6.3.2 Analysis of mouse embryos

To further investigate the value of employing C_{60}^+ in sample preparation, axial slices from a nine-day-old mouse embryo were studied. This model system was chosen because results from a previous study carried out by Ding et. al. revealed increased cholesterol concentration in specific regions of the embryo.²² The samples were freeze-dried for this imaging experiment without the use of any matrix or cyro-protectant; tissue

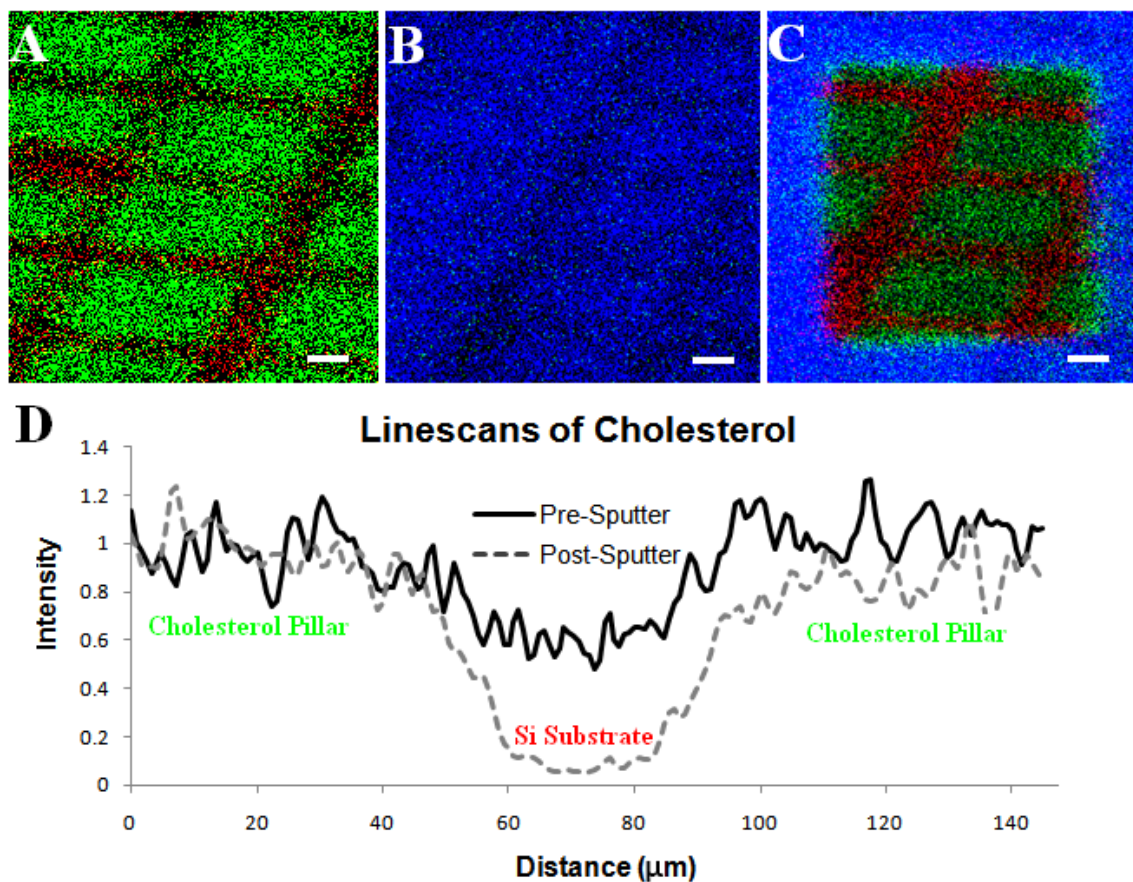


Figure 6-3. (A) Positive SIMS image of patterned cholesterol film on silicon created using physical vapor deposition, m/z 369 shown in green and m/z 28 in red. (B) The film was then cooled in vacuum (-196°C) and water was allowed to deposit, m/z 18 shown in blue and m/z 369 in green. The cholesterol layer is almost completely covered in water. (C) After etching with a dose of 10^{13} C_{60}^+ ions/ cm^2 the patterned film beneath is revealed with maintained spatial integrity. (D) Line scans across the film features reveal that the distribution of cholesterol on the surface is maintained when C_{60}^+ is used to remove the water overlayer versus when the surface is not cleaned with the C_{60}^+ nanotome. Scale bars are $25\ \mu\text{m}$.

slices were excised and either rinsed in 18 MΩ water or incubated in a 100 μM solution of soluble cholesterol for 30 min prior to rinsing. After rinsing, the tissue samples were plunge frozen in LN₂ and entered into the analysis chamber of the mass spectrometer at LN₂ temperature. The sample temperature was raised to -80° C allowing the ice to evaporate into the vacuum (1x10⁻⁸ torr) of the analysis chamber. Examination of the non-incubated tissue yielded insufficient cholesterol signal to establish differential distribution in the tissue slice (data not shown).

SIMS images of the cholesterol-incubated tissue were taken directly after freeze-drying. In these images the cholesterol signal was also weak and did not localize to any specific area of the tissue (Figure 6-4B). The C₆₀⁺ probe was used to sputter-clean the surface to expose the presumably undisturbed bulk of the tissue. The tissue was sputtered with a dose of 1x10¹³ C₆₀⁺/cm², which removed approximately 50 nm of tissue from the surface. The thickness of the amount removed was calculated using an estimated sputter yield of 500 molecules/ C₆₀⁺ and an estimated molecular density of 1x10²¹ molecules/cm³. These values were drawn from experiments performed using the disaccharide trehalose.¹⁶ The amount of material removed to uncover cholesterol localization is relatively small compared to the thickness of the tissue slice (~ 300 μm). The subsequent image (Figure 6-4C) shows increased cholesterol signal as well as localization to the genital ridge of the tissue.²² These results suggest that the damage created during freeze-drying the tissue samples without fixation, might be confined to the shallow depths (tens of nanometers) below the surface.

The changes in signal observed after removal of the surface of the tissue are shown in Table 6-1. After normalizing to total signal and image pixels, the cholesterol

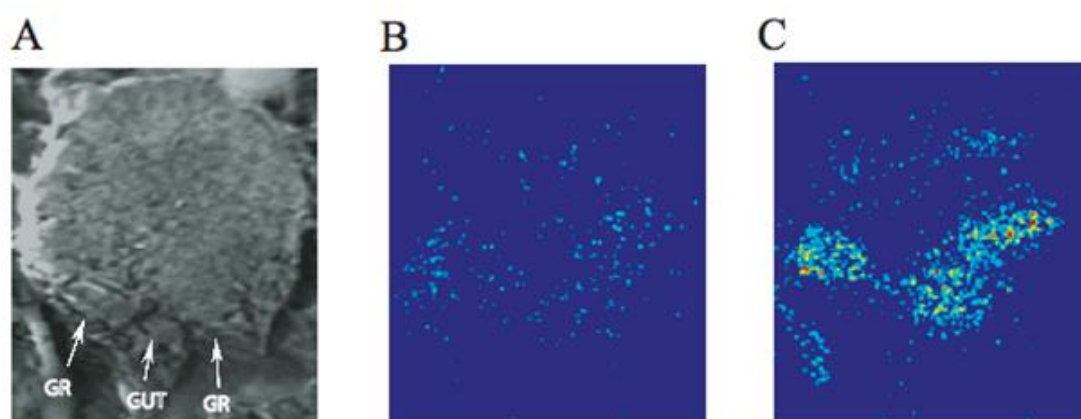


Figure 6-4. (A) Scanning ion image (SIM) of an axial slice from a 9-day-old mouse embryo. The gut and the genital ridge are identified by white arrows. The images in (B) and (C) are SIMS images of cholesterol (m/z 366-370) from the tissue in the SIM image. The image in (B) was taken prior to a sputter dose of $1 \times 10^{13} \text{ C}_{60}^+/\text{cm}^2$ and the image in (C) was taken after nanotome sputtering. Scale bars are 100 μm . Data collected by Michael Kurczy.

signal increased by 110 % and the PC signal decreased by 40 %. An increase in cholesterol signal following sputtering is an unexpected result, as it has been shown that depth profiling of deposited cholesterol films leads to an approximately 4.5 fold drop in signal before a steady state is reached.²³ This suggests the freeze-drying process affects the cholesterol molecules in the pre-sputtered sample to a significant degree. The decrease in PC is expected; however, the magnitude is less than expected based on depth profiling of a pure dipalmitoylphosphatidylcholine (DPPC) film in which signal decreases by approximately 3.5 times less than the initial value.²⁴ When the values are adjusted to account for the loss of signal observed in the sputtering of pure films (Table 6-1) the signal for PC is about twice the expected value, whereas the cholesterol is nearly an order of magnitude larger in intensity. These changes suggest that there are more intact cholesterol and DPPC molecules available for ionization after sputtering than before due to the removal of sample damage. These adjusted values, however, might not reflect actual concentrations because the ionization of these molecules might greatly differ in the complex environment of the tissue.

The work published by Ding et. al. was concerned with the role of cholesterol in the migration of primordial germ cells, the cells which mature to become gametes, to the genital regions of a vertebrate embryo. The germ cells migrate from the gut, which is adjacent to an area called the genital ridge. Using a novel cholesterol oxidase tipped electrode²⁵, an elevated amount of cholesterol was measured at the genital ridge.²² SIMS imaging was also employed to investigate cholesterol localization in these tissue samples as cholesterol has been observed in mouse tissue samples previously.¹² Initial

Table 6-1. Percent of ion signal following a sputter dose of $1 \times 10^{13} \text{ C}_{60}^+/\text{cm}^2$.

	PC (m/z 184)	Cholesterol (m/z 366-370)
Tissue Slice 1	70.4	202.6
Tissue Slice 2	52.1	207.8
Tissue Slice 3	58.4	221.4
Average	60 ± 9	211 ± 10
Adjusted Average	211 ± 33	948 ± 44

observations of the tissue samples with SIMS imaging revealed minimal cholesterol localization (*vide supra*). For this reason, the amount of cholesterol in the samples was augmented. The SIMS images show that the cholesterol concentration is preferentially increased in the genital ridge (Figure 6-4C). These results suggest that the increase in cholesterol measured with the electrode could be due to either synthesis or uptake of cholesterol by the embryo.

6.4 Conclusion

A C_{60} ion beam has been used as a nanotome to remove nanometers of interfering surface material from biologically relevant samples without significant damage to the underlying surface. The information uncovered would otherwise be unobservable with a surface technique such as ToF-SIMS imaging. Using known and estimated sputter yields and molecular densities, it is possible to remove material in a controlled and quantifiable manner. This method of controlled etching will greatly increase the number of analyzable biological samples for ToF-SIMS imaging. By removing the uppermost area of the surface, where much of the sample-preparation-induced damage occurs, reproducibility between samples can be significantly improved.

6.5 References

- (1) Altelaar, A. F.; Klinkert, I.; Jalink, K.; de Lange, R. P.; Heeren, R. M. A.; Piersma, S. R. *Anal. Chem.* **2006**, *78*, 734-742.
- (2) Brunelle, A.; Laprevote, O. *Curr. Pharm. Des.* **2007**, *13*, 3335-3343.
- (3) Cannon, D. M.; Pacholski, M. L.; Winograd, N.; Ewing, A. G. *J. Am. Chem. Soc.* **2000**, *122*, 603-610.

- (4) Chandra, S.; Morrison, G. H. *Biology of the Cell* **1992**, *74*, 31-42.
- (5) Kurczy, M. E.; Piehowski, P. D.; Parry, S.; Jiang, J.; Chen, G.; Winograd, N. *Appl. Surf. Sci.* **2008**, *255*, 1298-1304.
- (6) Parry, S.; Winograd, N. *Anal. Chem.* **2005**, *77*, 7950-7957.
- (7) Piehowski, P. D.; Kurczy, M. E.; Willingham, D.; Parry, S.; Heien, M. L.; Winograd, N.; Ewing, A. G. *Langmuir* **2008**, *24*, 7906-7911.
- (8) Quong, J. N.; Knize, M. G.; Kulp, K. S.; Wu, K. J. *Appl. Surf. Sci.* **2004**, *231-2*, 424-427.
- (9) Roddy, T. P.; Cannon, D. M.; Ostrowski, S. G.; Winograd, N.; Ewing, A. G. *Anal. Chem.* **2002**, *74*, 4020-4026.
- (10) Sjovall, P.; Lausmaa, J.; Nygren, H.; Carlsson, L.; Malmberg, P. *Anal. Chem.* **2003**, *75*, 3429-3434.
- (11) Fletcher, J. S.; Lockyer, N. P.; Vaidyanathan, S.; Vickerman, J. C. *Anal. Chem.* **2007**, *79*, 2199-2206.
- (12) Sjovall, P.; Lausmaa, J.; Johansson, B. *Anal. Chem.* **2004**, *76*, 4271-4278.
- (13) Ostrowski, S. G.; Van Bell, C. T.; Winograd, N.; Ewing, A. G. *Science* **2004**, *305*, 71-73.
- (14) Zheng, L. L.; Wucher, A.; Winograd, N. *J Am Soc Mass Spectr* **2008**, *19*, 96-102.
- (15) Cheng, J.; Wucher, A.; Winograd, N. *J Phys Chem B* **2006**, *110*, 8329-8336.
- (16) Cheng, J.; Winograd, N. *Anal. Chem.* **2005**, *77*, 3651-3659.
- (17) Wagner, M. S. *Anal. Chem.* **2005**, *77*, 911-922.
- (18) Braun, R. M.; Blenkinsopp, P.; Mullock, S. J.; Corlett, C.; Willey, K. F.; Vickerman, J. C.; Winograd, N. *Rapid Commun. Mass Spectrom.* **1998**, *12*, 1246-+.
- (19) Wong, S. C. C.; Hill, R.; Blenkinsopp, P.; Lockyer, N. P.; Weibel, D. E.; Vickerman, J. C. *Appl. Surf. Sci.* **2003**, *203*, 219-222.
- (20) Weibel, D.; Wong, S.; Lockyer, N.; Blenkinsopp, P.; Hill, R.; Vickerman, J. C. *Anal. Chem.* **2003**, *75*, 1754-1764.
- (21) Fletcher, J. S.; Conlan, X. A.; Jones, E. A.; Biddulph, G.; Lockyer, N. P.; Vickerman, J. C. *Anal. Chem.* **2006**, *78*, 1827-1831.
- (22) Ding, J. X.; Jiang, D.; Kurczy, M.; Nalepka, J.; Dudley, B.; Merkel, E. I.; Porter, F. D.; Ewing, A. G.; Winograd, N.; Burgess, J.; Molyneaux, K. *Bmc Developmental Biology* **2008**, *8*, 14.
- (23) Kozole, J.; Wucher, A.; Winograd, M. *Anal Chem* **2008**, *80*, 5293-5301.
- (24) Kozole, J.; Szakal, C.; Kurczy, M.; Winograd, N. *Appl. Surf. Sci.* **2006**, *252*, 6789-6792.
- (25) Devadoss, A.; Burgess, J. D. *J. Am. Chem. Soc.* **2004**, *126*, 10214-10215.

Chapter 7 Summary and Future Directions

7.1 Summary

The techniques described in this thesis are directed towards the goal of using ToF-SIMS imaging as analytical tool to study the spatial composition of lipid membranes in single cells. ToF-SIMS is a unique methodology that is well suited to this task for a multitude of reasons. The first is the inherent surface sensitivity of the technique. Molecular dynamics simulations show that 95% of sputtered materials derive from the top two atomic layers.¹ Thus spectral information obtained is primarily from the outer leaflet of the cell membrane. Secondly, the technique is chemically specific without the use of labels. Much of the study of membrane composition has been carried out using fluorescent techniques.² These methods require the use of bulky labels that can alter the biophysical properties of the molecule, or the incorporation of fluorescent probes that lack chemical specificity. Third, the primary ion sources employed to bombard the surface are highly focusable, and many sources are routinely operated at spot sizes smaller than 300 nm.³ This offers the possibility to image with higher spatial resolution than is available with most optical techniques. Finally, the analysis is compatible with cryogenic sample preservation methodology.^{4,5} This allows us to quench cell samples and capture dynamic processes in the act, without the rearrangement of lipids that can occur during other sample fixing methods.^{6,7}

As discussed in Chapters 1 and 2 of this thesis, sample preparation is crucial to obtaining useful spatial information from biological samples. A freeze-fracture protocol has been developed in the lab to achieve the preservation of single cells. This methodology has been successful for certain applications. However, it does suffer from drawbacks of expense, time investment, and variability. For these reasons, it was decided to investigate the application of

freeze-etching to produce cryogenically preserved single cells for ToF-SIMS analysis. This approach has proven to be successful in preserving cells as well as decreasing preparation time and increasing reproducibility. In addition, it was shown that re-deposition of water on the surface of the cell after freeze-etching increases the ionization efficiency of many interesting lipid species.⁵

Due to the high-energy nature of the sputtering process, extensive fragmentation of biomolecules can occur during SIMS analysis. Because of this, most lipids mapped in imaging studies are identified by characteristic fragment ions. These fragment ions are generally identified through the analysis of pure film standards by picking peaks. Accurate identification of fragment ions is generally complicated by the complex spectrum that is generated and a lack of mass resolution. Recently the Winograd lab has developed a hybrid-quadrupole orthogonal time-of-flight mass spectrometer. This instrument allows the utilization of collision-induced dissociation to discover fragments of cholesterol that have not previously been identified. These fragment ions offer great yield enhancements over the pseudomolecular ion used in prior experiments which greatly improved contrast for cholesterol mapping experiments.⁸

I was able to combine these advances to produce the highest spatial resolution, mass-specific images of cholesterol and phosphatidylcholine (PC) to date. To analyze these images, a new methodology that makes use of the Poisson nature of imaging data was developed. This new model gives a much more detailed description of the analyzed surface, and has been used to statistically validate features that are observed in high resolution images. In addition, this model emphasizes the importance of ionization efficiency on the obtainable spatial resolution in an experiment. By analyzing images as pixel intensity histograms, it was determined that cholesterol and PC are heterogeneously distributed on the surface of the RBL-2H3 mast cell surface. This represents a large step forward in single cell imaging, and should serve as a starting block for future studies of lipid membrane heterogeneity.

One area for which ToF-SIMS imaging has been used to make major contributions is the study of curvature-induced lipid heterogeneity.⁹ For these studies mating *Tetrahymena thermophila* have been used as a model system to study the aggregate effect of forming multiple fusion pores on the distribution of the cylindrical lipid PC. It has been demonstrated that the fusion region of the cells is in fact depleted in PC. The next question to address is when during fusion does this domain form; does the cell prepare for fusion by forcing lamellar lipid away from the site, or does the mechanical force supplied by fusion machinery cause the domain formation. Temporal experiments of the fusion process reveal that the domain forms in response to fusion and does not exist prior.

Another area of interest to those carrying out biological imaging experiments is the unique properties of the C_{60}^+ cluster projectile. The ability of this projectile to remove the chemical damage created by its impact creates a new dimension of analytical possibilities.^{3, 10, 11} In this thesis, the potential of this source as a supplemental sample preparation utility is demonstrated. It was postulated that much of the sample damage that is seen when preparing samples by freeze-drying is confined to the topmost molecular layers. The C_{60}^+ projectile can be used to clean away these layers exposing the lost spatio-chemical information. The ability to erode molecular layers with minimal damage accumulation also opens up the possibility of 3-dimensional analysis with ToF-SIMS.

Overall, ToF-SIMS imaging has been established as a powerful analytical tool in the investigation of cell membranes. However, there are limitations with the described methodology that will need to be addressed for this tool to be widely applied. Some of the limitations that are discussed in this thesis are mass resolution, tandem MS capabilities, and ionization efficiency. In a ToF-SIMS experiment, the flight tube is coaxial to the sputtering event, thus the mass resolution is limited by the width of the primary ion pulse, as well as energy and angle aberrations of desorbed ions. This results in significant time spread that is not accounted for by the

implementation of a dual stage reflectron. In complex samples such as cells and tissue, this causes isobaric interferences between different fragments. Additionally, it is inevitable that complex samples will produce fragments that have not been previously identified. In these cases it is imperative to accurately identify these ions, which can be achieved through MS/MS analyses. Another limitation is the ionization efficiency of the molecules of interest. Ultimately, the number of ions that can be generated from a small finite sample volume limit the data that can be obtained.

7.2 Future Directions

The field of biological ToF-SIMS analysis has expanded greatly in the past decade. This is largely due to the development of cluster ion sources which have been shown to improve secondary ion yields, extend mass range, reduce sample damage, and reduce sample charging, when compared with atomic projectiles.^{3, 12} The demands of biological sample analysis have greatly outrun the capabilities of traditional instrumentation.^{13, 14} As a result there is now considerable effort underway in the lab to address the shortcomings of traditional ToF-SIMS imaging. In the Winograd laboratory this had led to the development of the Qstar hybrid C_{60}^+ SIMS quadrupole orthogonal time-of-flight mass spectrometer. A schematic of this instrument can be found in Chapter 1. This new analytical platform offers many advantages over previous instruments: tandem MS capabilities, improved mass resolution and mass accuracy, increased imaging area and greatly increased duty cycle.¹⁴

7.2.1 Tandem MS experiments in SIMS

The utility of MS/MS in fragment identification has been discussed in Chapter 3. However, further discussion of the utility of this approach is warranted. As mentioned in chapter 3, isobaric interferences are unavoidable in the low mass range (<200 m/z) of a SIMS experiment. Obtaining a CID spectrum of these peaks allows us to probe the possibly multiple species that comprise it. The selectivity of the CID approach can even allow differentiation of structural isomers. An example of this, leucine (Leu) and isoleucine (Ile), is shown in Figure 7-1. Figure 7-1A gives the structures of these two isomers that vary in the location of a methyl group. This difference suggests that these two molecules may fragment differently. To study these molecules, pure films of each were prepared on silicon substrates. These two substrates were then mounted next to each other on the sample plate. Figure 7-1B shows a mass-specific image of (M+H)⁺ ion at 132.10, which is the same for both molecules. It can be seen that this ion is uniformly distributed and equally present on both shards. MS/MS analysis reveals that the (m/z)⁺ 69 is only present in significant intensity from the isoleucine. The MS/MS spectra of Leu and Ile can be seen in Figure 7-1D and 7-1E. Thus (m/z)⁺ can then be mapped to differentiate the Ile, Figure 7-1C.

Also worth mentioning is the incredible sensitivity that has been demonstrated when using CID with SIMS ions. Figure 7-2A shows a mass-specific image of an *Aplysia californica* neuron. Vitamin E, (m/z)⁺ 430.38, is shown in blue and demonstrates the ability of the Qstar instrument for single cell imaging. Of particular interest is Figure 7-2B, which shows a CID spectrum of vitamin E obtained from that single cell. A CID spectrum obtained from a neat film of vitamin E is shown in Figure 7-2C, which confirms the identification of vitamin E.

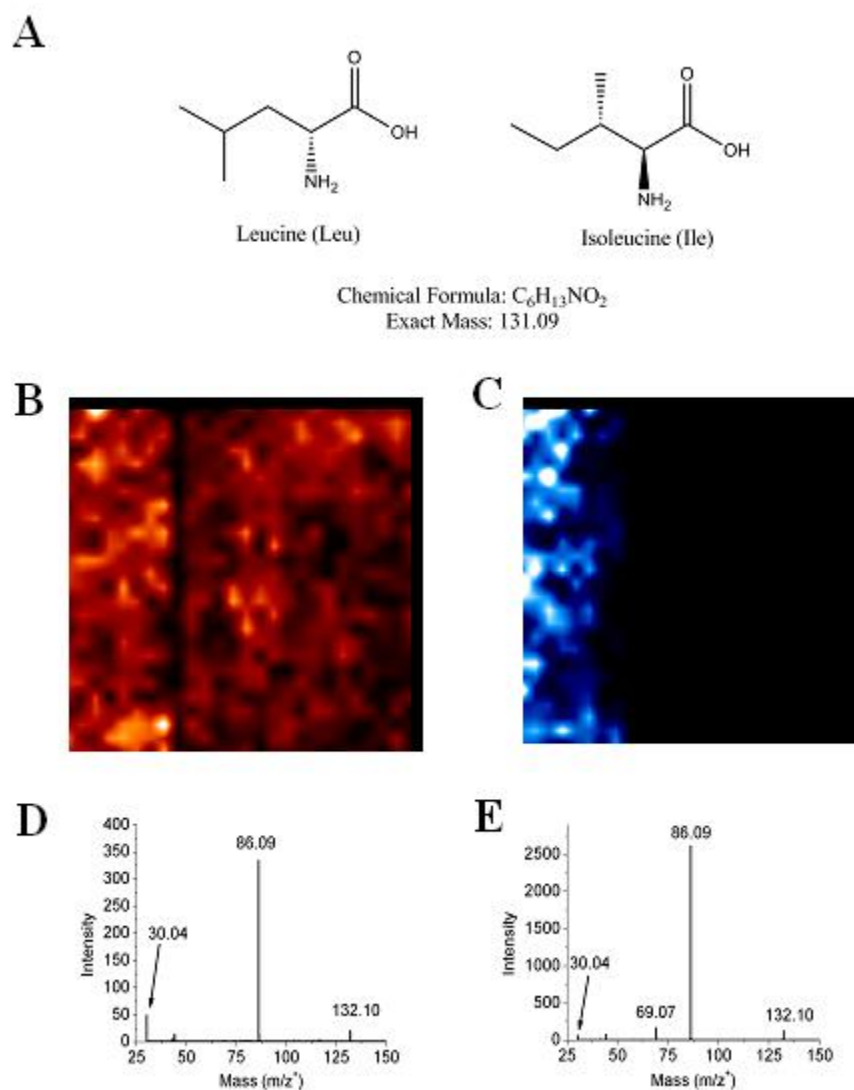


Figure 7-1. MS/MS SIMS analysis of the amino acids D-Leucine (Leu) and Isoleucine (Ile) (A) The two structural isomers (Leu) and (Ile). (B) MS/MS SIMS image of the junction of two different thin films on silicon shards. The chemical image of $M+H$ does not reveal the identities of the thin films as $m/z^+ 132.10$ maps to both shards. (C) MS/MS of $m/z^+ 132.10$ reveals the fragment ion $m/z^+ 69.07$ only comes from Ile, and so can be used to show that Ile is on the left, while Leu is on the right. (D,E) The MS/MS spectra of Leu and Ile are shown, respectively. Data collected by Anthony Carado.

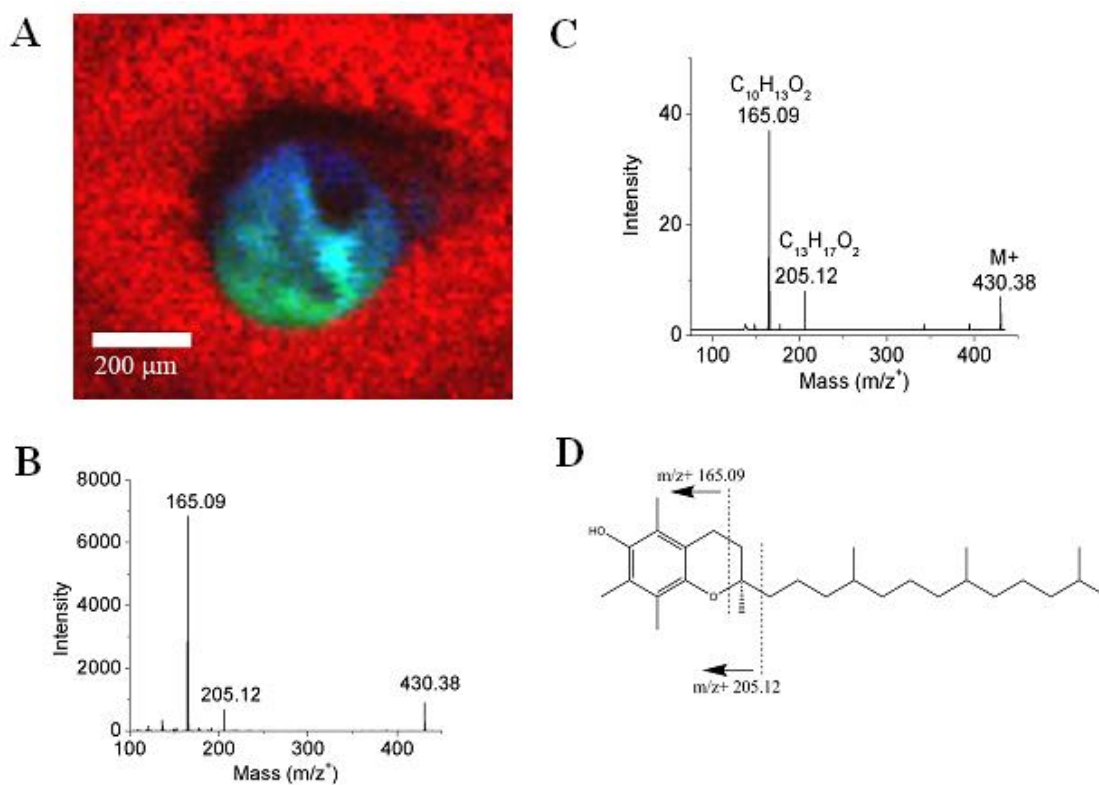


Figure 7-2. (A) Dynamic secondary ion image of a single aplysia cell with phosphate background in red, vitamin E in blue, and cholesterol in green. Cell diameter is approximately 350 μm . (B) CID spectrum of vitamin E from a single aplysia cell. (C) SIMS neat thin film reference MS/MS spectrum of vitamin E. (D) Fragmentation points of vitamin E. Data collected by Anthony Carado.

7.2.2 High mass resolution and mass accuracy

Another reoccurring theme in this thesis is the complexity of the spectra acquired due to the number of species present in biological samples as well as large amounts of fragmentation. This complexity is only increased when mass resolution is increased.¹⁴ An example of a typical spectrum is shown in Figure 7-3. This magnification clearly reveals that each nominal mass is composed of multiple species. In a traditional ToF-SIMS imaging experiment, this complexity would have led to inaccurate mapping. It is important for the success of future biological SIMS analyses that the species of interest is the only component of the peak that is mapped. The high mass resolution offered by this new platform will greatly reduce isobaric interference in imaging experiments as well as aid in the accurate identification of unknown ions.

7.2.3 Increased imaging area

Imaging of large tissue samples can be very difficult with traditional ToF-SIMS instruments. First, the coaxial position of the flight requires the use of pulsed beams, which results in prohibitively long image acquisition times. Secondly, the field-of-view is limited in traditional ToF-SIMS by the acceptance window of the collection optics. This necessitates the stitching together of many smaller images to generate a larger image. The hybrid instrument overcomes the first limitation with an orthogonally oriented flight tube, which permits a DC analysis beam. This greatly decreases the time it takes to obtain a large image. Due to the nature of the collection and scanning the stage instead of the analysis beam, the second limitation is removed. The value of this is demonstrated in Figure 7-4. The figure shows the PC head group (green) and cholesterol (blue) localizations in a rat cerebellum. The dashed white line indicates the region that has been magnified. The wide spatial resolution range obtainable by this

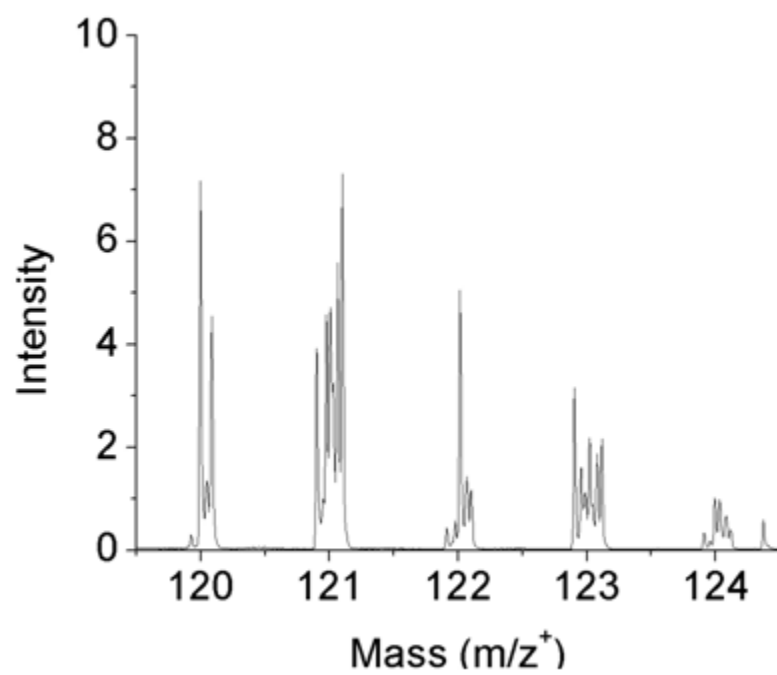


Figure 7-3. Mass range m/z^+ 119.5-124.5 for a mouse brain slice. Data Collected by Anthony Carado.

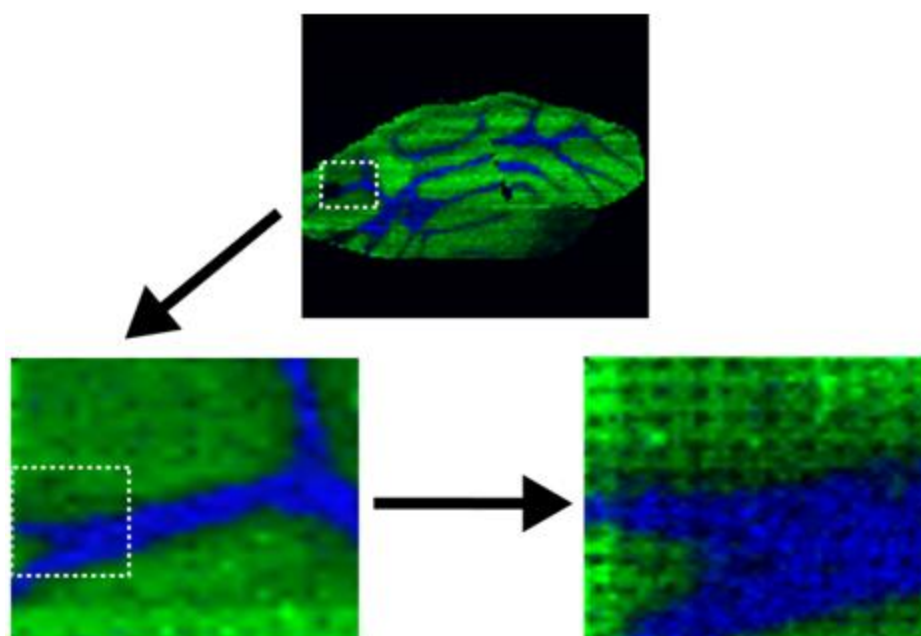


Figure 7-4. Secondary ion image of a rat brain slice using successively smaller step sizes to demonstrate the versatility of SIMS imaging with this platform. Phosphatidylcholine headgroup ion $m/z+ 184.07$ is shown in green while cholesterol pseudo-molecular ion $m/z+ 369.35$ is shown in blue. The white dashed line indicates the region of greater magnification in the following image. Data Collected by Melissa Passarelli.

instrument will greatly increase the diversity of samples that can be effectively analyzed by SIMS. In addition, large survey images of a sample can be taken quickly allowing the analyst to identify regions of interest. These regions can then be probed in much higher detail.

7.2.4 Increased duty cycle

As mentioned above the orthogonal geometry of the QStar XL allows for the utilization of DC analysis beams. Thus, the primary ion beam can deliver up to four orders of magnitude greater ion flux. This has important implications in imaging as this increase in dosage could be achieved for the highly focused beams utilized in single cell experiments, greatly reducing analysis time. Furthermore, it allows the mass resolution that is demonstrated in Figure 7-3 to be obtained with no attenuation of primary ion dose.

This increase in duty cycle also has major implications for an emerging field of research made possible by the utilization of cluster primary ion beams, three-dimensional ToF-SIMS imaging. To achieve three-dimensional imaging, multiple 2D images are taken with sputtering of material between images. The images obtained can be placed in a stack to give a 3D representation of the sample. In a traditional ToF-SIMS experiment, the material sputtered cannot be analyzed and thus valuable ions are lost. The orthogonal ToF permits continuous sampling, yielding 3D images with much greater information density. This is particularly important in the case of single cell experiments where the amount of material is limited. This could be utilized to monitor the sub-cellular location of various compounds, such as metabolite or drugs, in 3D.

7.3 Conclusions

The unique capabilities of ToF-SIMS as an analytical tool make it a powerful tool for the study of lipid distribution in cell membranes. Improvements in cryogenic sample preparation have been combined with the implementation of new MS analysis platforms to produce the most information rich images of cholesterol to date. A statistical model based on Poisson statistics has been developed to validate cholesterol distributions on the surface of RBL-2H3 cells. This analysis led to the conclusion that cholesterol is heterogeneously distributed in the resting RBL-2H3 membrane. In addition, this model puts forward a robust, new framework for ToF-SIMS single cell image analysis, which will greatly improve data interpretation. These experiments have been used to demonstrate the limitations of traditional ToF-SIMS instrumentation; however, recent work in the lab has been directed at addressing these limitations. Implementation of cluster ion sources as well as new MS platforms shows great promise to advance the application of ToF-SIMS as an important biological imaging technique.

7.4 References

- (1) Vickerman, J. C.; Briggs, D., Eds. *ToF-SIMS: Surface Analysis by Mass Spectrometry*; IM Publications and Surface Spectra Limited: West Sussex, 2001.
- (2) Mukherjee, S.; Maxfield, F. R. *Annu. Rev. Cell Dev. Biol.* **2004**, *20*, 839-866.
- (3) Winograd, N. *Anal. Chem.* **2005**, 143A-149A.
- (4) Cannon, D. M. J.; Pacholski, M. L.; Winograd, N.; Ewing, A. G. *J. Am. Chem. Soc.* **2000**, *122*, 603-610.
- (5) Piehowski, P. D.; Kurczy, M. E.; Willingham, D.; Parry, S.; Heien, M. L.; Winograd, N.; Ewing, A. G. *Langmuir* **2008**, *24*, 7906-7911.
- (6) Ausserer, W. A.; Chandra, S.; Morrison, G. H. *Journal of Microscopy* **1989**, *154*, 39-57.
- (7) Severs, N.; Shotton, D., Eds. *Rapid Freezing, Freeze-Fracture, and Deep Etching*; Wiley-Liss: New York, 1995.
- (8) Piehowski, P. D.; Carado, A. J.; Kurczy, M. E.; Ostrowski, S. G.; Heien, M. L.; Winograd, N.; Ewing, A. G. *Anal. Chem.* **2008**, *80*, 8662-8667.
- (9) Ostrowski, S. G.; Bell, C. T. V.; Winograd, N.; Ewing, A. G. *Science* **2004**, *305*, 71-73.
- (10) Cheng, J.; Winograd, N. *Anal. Chem.* **2005**, *77*, 3651-3659.

- (11) Wong, S. C. C.; Hill, R.; Blenkinsopp, P.; Lockyer, N. P.; Weibel, D. E.; Vickerman, J. *C. App. Surf. Sci.* **2003**, *203*, 219-222.
- (12) Toubol, D.; Kollmer, F.; Niehus, E.; Brunelle, A.; Laprevote, O. *J. Am. Soc. Mass Spectrom.* **2005**, *16*, 1608-1618.
- (13) Fletcher, J. S.; Rabbani, S.; Henderson, A.; Blenkinsopp, P.; Thompson, S. P.; Lockyer, N. P.; Vickerman, J. C. *Anal. Chem.* **2008**, *80*, 9058-9064.
- (14) Carado, A.; Passarelli, M. K.; Kozole, J.; Wingate, J. E.; Winograd, N.; Loboda, A. V. *Anal. Chem.* **2008**, *80*, 7921-7929.

Appendix A

Imaging Instrumentation and Procedure

In order to carry out the analysis of frozen-hydrated biological samples discussed above, new instrumental implements were needed to handle these samples. Thus a novel freeze-fracture sample preparation chamber was designed in-house to achieve these goals.⁹ The resulting chamber is diagrammed in Figure A-1. Copper implements are shown in yellow, to highlight these are cooled to LN₂ temperatures during entry of a frozen sample. Because frozen samples are prone to condensation accumulation during preparation, these experiments can introduce a lot of water into the vacuum chamber. To help maintain the vacuum, an IR lamp is employed between experiments to help remove the excess water. To promote a better understanding of the frozen sample handling process, a detailed procedure for entering the sample is listed below.

1. Before entering the sample into the instrument all components that contact the sample must be cooled. The instrument has five dewars connected to it. It is cooled by flowing N₂, at a pressure of ≈ 40 psi, through copper tubing that is immersed in the dewars. All five dewars are filled with LN₂ and the temperature is monitored using thermocouple feed-throughs attached to the cooled components. In addition, the instrument has a sorption pump that evacuates the fast entry port. This pump must be cooled to LN₂ temperature prior to introducing the sample.
2. The sample must be mounted onto the analysis block under LN₂. A London finder grid is first attached to the sample block using conductive silver paste. Then, a Styrofoam cooler is filled with LN₂ and the sample block, samples, and fast entry apparatus are placed in the cooler. When the LN₂ stops boiling, the sample can be mounted.

3. To mount the sample, a shard is fit in the recessed sample area with the top shard facing out. Two screws with washers are used to affix the sample to the block. The sample block is mounted on the entry port post and fit inside the metal sheath. The sheath is then screwed onto the fast entry port arm, while keeping the sample assembly under nitrogen.
4. Introducing the sample must be done as quickly as possible to minimize warming as well as condensation. The arm assembly is quickly inserted into the entry port, and the port is evacuated using the sorption pump for 30 s. After 30 s, the sample is injected into the instrument and quickly transferred to the pre-cooled sample transfer arm.
5. The sample is then transferred to the freeze-fracture stage. The temperature and pressure are crucial during the fracture process.⁹ It is usually necessary to wait several minutes for the vacuum to recover after introducing the sample.
6. To be able to fracture the sample, it is important that the block is mounted with the fracture shard extending above the substrate on the side of the fracture knife. The knife blade is positioned above the top shard. In the z-direction, the blade is positioned such that it will fall between the top shard and the sample block when brought down.
7. When the fracture stage reaches the desired temperature of $-106.5\text{ }^{\circ}\text{C}$, the sample is fractured by turning the blade counterclockwise with a quick flick of the wrist. This should result in the top shard snapping off. It is important to design a cold stage to catch the shard on to prevent water desorption changing the vacuum and depositing on the sample.
8. After the fracture, the blade is withdrawn from the sample approximately 5 mm and positioned directly in front of the sample. The knife blade acts as a cold trap, because it is colder than the sample, catching excess water vapor caused from the fracture.
9. When the preparation chamber pressure has recovered from the fracture, the sample can then be transferred to the sample analysis chamber.

Figure A-2 gives a schematic of the sample analysis chamber on the Kratos instrument from the top down. The cold clamp is also connected to cooling lines to maintain LN₂ temperatures. The ion source is currently an indium liquid metal ion gun (LMIG). To place the sample in front of the ion gun the swing arm rotates and locks into the cold clamp. Not shown in this schematic is the microscope used to view the sample. The microscope sits directly on top of the sample chamber and the optics inside the vacuum are mounted on a carousel with the extraction optics. A brief description of the image acquisition procedure is described below.

1. In the case of adherent cells it is useful to do a freeze-etch step prior to imaging.⁴¹ This is achieved by removing the dewar from the sample stage cooling line. This will result in the sample stage warming at a rate of approximately 5 °C/min. The stage is warmed to -80 °C to remove excess surface water and then quickly returned to LN₂ temperature.
2. The sample beam is focused. A standard sample, a London finder grid, attached to the sample block is used to obtain the desired focus. The primary ion beam is focused to a point by 2 electrostatic lenses in series. The focal point of these lenses can be manipulated by increasing and decreasing the potential that is applied to them. The London finder grids have distinct features of various sizes and are made to very high specifications. The focal point of the beam is manipulated until the user can visually distinguish features of the same size scale as they intend to measure. The interface width (the width measured for the signal to decrease from 85% to 15%) of a sharp interface is a good estimate of the primary ion beam spot diameter. For optimal imaging, this width should be less than or equal to the width of the pixels to be used for imaging.
3. Before cell imaging, the SIMS beam must be aligned with the microscope mounted on the instrument so that cells to be imaged can be identified and positioned in front of the primary ion beam. To do this, a digital micrograph of the grid is taken using the camera

on the microscope. Then a SIMS image of the grid is obtained. The two images are overlaid to determine the imaging area in the eyepiece.

4. Calibrating the spectrum is important to obtain the proper peak assignments. Calibration can be achieved by using the spectrum obtained from the SIMS image of the grid. A good three-point calibration can be obtained, from Na, Cu, and Ag. The Ag signal comes from the conductive silver paste that is used to mount the grid to sample block.
5. When collecting SIMS images the static limit should be used to insure a reliable representation of the surface. The static limit is defined as 1×10^{13} ions/cm². To calculate the limit you must know the pulse width, primary ion current, field of view, and the pixel size. A discussion of each of these is found below.
6. Primary ion current- to measure the primary ion current, a picoammeter is connected to the analysis stage through the stage voltage feed through while the beam is in the DC mode. Higher primary ion currents result in faster image collection times, as the static limit is reached faster. However, higher currents are obtained at the expense of spot size.
7. Spot size- this is the diameter of the primary ion beam at the focal point; it is the ultimate limit to spatial resolution. Smaller spot sizes can be obtained through rigorous beam alignment and generally result in lower primary ion currents.
8. Pixel size- the pixel size is the FOV divided by the amount of pixels chosen for the image. Choosing fewer pixels results in quicker acquisition times at the expense of spatial resolution.
9. Mass range- the mass range that is collected for an experiment depends on what the analyst is looking for. Traditionally the SIMS analyst collects from 10-1000 amu.

Appendix B

Matlab Scripts for Data Processing

Script 1, Thresholding

```
%Threshold sets any pixel less than or equal to the discriminator, to
zero
%Thresholding works on mass-specific images

function[threshold_data] = threshold(input_data, discriminator)

a= discriminator;

%Set x and y dimensions equal to input dimensions

[y_size, x_size] = size(input_data);

%Make an empty matrix for the output data

threshold_data = zeros(y_size, x_size);

%For loop compares each pixel intensity to the discriminator and sets
all
%less than or equal to zero

for i = 1: y_size
    for j = 1:x_size
        if input_data(i,j) <= a
            threshold_data(i,j) = 0;
        else
            threshold_data(i,j) = input_data(i,j);
        end
    end
end
end
```

Script 2, Nearest-neighbor smoothing

```
%Performs a nearest-neighbor smooth on the image data
%num_cycles is how many times you want to run the smoothing loop
```

```

%the second cycle will be run on the already smoothed once data
%width of smooth is how many neighbors will be averaged
%thus width_smooth = 1 will average 9 pixels and width_smooth =2
%willl average 25 pixels
%Smoothing is done on mass specific images

function [smoothed_data] = smooth(txt_data, num_cycles, width_smooth)

%Set y and x equal to the dimensions of the input matrix

[y_size, x_size] = size(txt_data);

%Make an empty matrix for the output data
smoothed_data = zeros(y_size, x_size);

%loop adds the pixels to be smoothed together, has be divided by number
%of pixels used to obtain average
num_pixels = (width_smooth*2+1)*(width_smooth*2+1);

%For loop adds the pixels together and divides by the number of pixels
%summed. Inserts this data into txt_data so that if multiple cycles
are
%run, the second cycle is run on the previously smoothed data.

for n = 1:num_cycles
    for i = width_smooth+1:y_size-width_smooth
        for j = width_smooth+1:x_size-width_smooth
            temp = sum(txt_data(i-width_smooth:i+width_smooth, j-
width_smooth:j+width_smooth));
            smoothed_data(i , j) = sum(temp)/num_pixels;
        end
    end
    txt_data = smoothed_data;
end
end

```

Script 3, Intensity binning

```

%mathematically adds intensity of neighboring
%pixels. Radius equals number of bins added in x and y direction
%Binning can only be run on mass specific images

function[bin_data] = bin(input, radius)

a = radius;

%Set x and y equal to the dimensions of the input matrix

[y_size, x_size] = size(input);

```

```

%Define the dimensions of the output matrix
%Divide by a+1 because the output matrix will be smaller
%Add 0.5 to make sure it rounds down to chop off incomplete
%pixels

y_out = round((y_size/(a+1))-0.5);

x_out = round((x_size/(a+1))-0.5);

%Make an empty matrix with the new matrix dimensions

bin_data = zeros(y_out, x_out);

%For loop adds i+a, j+a pixels together and puts the total
%in the new matrix
%loop skips to next y when a fully binned pixel cannot be created
%loop breaks when no more fully binned pixels can be created

for i = 1:(a+1):y_size
    for j = 1:(a+1):x_size
        if (j + a) > x_size
            continue
        end
        if (i + a) > y_size
            break
        end
        temp = sum(input(i:(i+a), j:(j+a)));
        bin_data(((i+a)/(a+1)),((j+a)/(a+1))) = sum(temp);
    end
end
end

```

Script 4, Population selection

```

%Population allows the user to display pixels that fall within a
specified
%data region, i.e. a population

function[population_data] = population(input_data, lower_bound,
upper_bound)

a = lower_bound;

b = upper_bound;

%Set x and y dimensions equal to input data dimensions

[y_size, x_size] = size(input_data);

```

```
%Make an empty matrix for the output data

population_data = zeros(y_size, x_size);

%For loop compares each pixel intensity to the boundaries and sets all
%less than lower_bound zero and greater than upper_bound to zero

for i = 1: y_size
    for j = 1:x_size
        if input_data(i,j) < a
            population_data(i,j) = 0;
        elseif input_data(i,j) > b
            population_data(i,j) = 0;
        else
            population_data(i,j) = input_data(i,j);
        end
    end
end
```

VITA

Paul D. Piehowski

Education

Ph.D. Analytical Chemistry, The Pennsylvania State University, 2009
B.A. Chemistry, St. John's University. 2003

Selected Publications

P.D. Piehowski, M.E. Kurczy, D.G. Willingham, S.A. Parry, M.L. Heien, N. Winograd, and A.G. Ewing. "Freeze-Etching and Vapor Matrix Deposition for ToF-SIMS Imaging of Single Cells", *Langmuir*, **2008**, 24, 7906-7911.

P. D. Piehowski, Anthony J. Carado, Michael E. Kurczy, Sara G. Ostrowski, Michael L. Heien, Nicholas Winograd, Andrew G. Ewing, "MS/MS Methodology to Improve Sub-Cellular Mapping of Cholesterol Using ToF-SIMS", *Anal. Chem.*, **2008**, 80, 8662-8667.

Michael L. Heien, **Paul D. Piehowski**, Nicholas Winograd, Andrew G. Ewing. "Lipid detection, identification, and imaging single cells with SIMS". *Mass Spectrometric Imaging. History, Fundamentals and Protocols*, Humana Press Methods in Molecular Biology Series. In Press.

Michael E. Kurczy, **P. D. Piehowski**, Michael L. Heien, Craig T. Van Bell, Nicholas Winograd and Andrew G. Ewing, "Lipid Domain Formation is Necessary for Irreversible Conjugation in *Tetrahymena thermophila*". Submitted, *PNAS*.

Michael E. Kurczy, **P.D. Piehowski**, Michael L. Heien, Kathleen Molyneaux, Nicholas Winograd, Andrew G. Ewing, "Utilizing the Unique Properties of Cluster Ion Projectiles to Increase the Reproducibility of Sample Preparation for Biological SIMS Imaging". Submitted, *JASMS*.

P.D. Piehowski, Angel M. Davey, Erin D. Sheets, Nicholas Winograd, Andrew G. Ewing, Michael L. Heien, "Mass Spectrometry Imaging of Sub-Cellular Features: Poisson Counting and Spatial Resolution". *Anal. Chem.* 2009, 81, 5593-5602. Selected Honors

Braucher Fellowship, The Pennsylvania State University
SIMS Workshop Student Award
Travel Award, The Pennsylvania State University